UNIVERSIDAD NACIONAL AUTÓNOMA DE MÉXICO
POSGRADO EN CIENCIAS FÍSICAS

Interacting Bose Gas in Multi-Rod Lattices: Ground State Properties and Quantum Phase Transitions

T E S I S
QUE PARA OPTAR POR EL GRADO DE:
DOCTOR EN CIENCIAS (FÍSICA)

PRESENTA
OMAR ABEL RODRÍGUEZ LÓPEZ

TUTOR
DR. MIGUEL ÁNGEL SOLÍS ATALA (IF)

MIEMBROS DEL COMITÉ TUTOR
DR. FRANCISCO JAVIER SEVILLA PÉREZ (IF)
DR. MANUEL DE LLANO DE LA GARZA (IIM)

CIUDAD UNIVERSITARIA, CIUDAD DE MÉXICO, ENERO DE 2020

To my family

Abstract

The physics of quantum many-body systems is a research field of the highest interest of the current scientific community. Remarkable phenomena arise in quantum many-body systems, including Bose-Einstein condensation, superfluidity, superconductivity, supersolidity, and topological phases. In the experimental ground, ultracold atoms in optical lattices have emerged as an ideal tool to simulate quantum many-body systems at low temperatures within periodic structures analog to those found in condensed matter. From the theoretical point of view, some tools to describe these systems are the Gross-Pitaevskii equation and Dynamical Mean-Field Theory, complemented by numerical approaches based on Density Functional Theory, Quantum Molecular Dynamics, and Quantum Monte Carlo methods, for instance.

Especially (but not limited to) in condensed matter physics, quantum many-body systems in periodic structures will always have a prominent place. This thesis presents the ground state properties of a one-dimensional, interacting Bose gas constrained within a periodic multi-rod lattice at zero temperature. We did our research using two complementary approaches. First, we used mean-field theory to analyze the weakly-interacting regime, i.e., we solved the Gross-Pitaevskii equation. Next, to go beyond the mean-field picture and investigate the effect of short-range repulsive interactions of arbitrary strength on the quantum behavior of the system, we used stochastic *ab-initio* Quantum Monte Carlo techniques.

Under the mean-field picture, we studied the effect of the multi-rod lattice, as well as the impact of the interactions on the condensate wave function, obtaining analytic solutions for the density in terms of Jacobi elliptic functions and incomplete elliptic integrals. Also, we characterized the energy spectrum of the system, the chemical potential, the compressibility of the system, and the sound velocity of the condensate. Finally, we used our model to predict the properties of Bose gases in optical lattices with a subwavelength structure, since we are confident that our model is an excellent candidate to study these novel structures.

To study our system beyond the mean-field theory regime, we mainly use the Variational Monte Carlo and Diffusion Monte Carlo methods. First, we propose a suitable trial wave function to represent the ground state, which we carry to its exact value within a controllable statistical error. Then, we calculate both

the ground state energy and the static structure factor as functions of the interaction and lattice parameters. Finally, we show that the Bose gas presents a superfluid to Mott-insulator phase transition at zero temperature. We give the phase diagram where we plot both the superfluid and Mott-insulator phases, as well as the boundary between them, as functions of the interaction strength and the lattice height.

Resumen

Los sistemas cuánticos de muchos cuerpos son una fuente fascinante de fenómenos físicos: condensación Bose-Einstein; superfluidez, superconductividad y supersolidez; transiciones de fase cuánticas topológicas; o la transición de fase superfluido a aislante de Mott en el gas de Bose, por nombrar algunos ejemplos. En el campo experimental, los átomos ultra fríos en redes ópticas han surgido como una plataforma ideal para simular sistemas cuánticos de muchos cuerpos en estructuras periódicas a muy bajas temperaturas. Desde el punto de vista teórico las herramientas para describir estos fenómenos incluyen, por ejemplo, la ecuación de Gross-Pitaevskii en la aproximación de campo medio, y la teoría de campo medio dinámica, las cuales pueden ser complementadas por métodos numéricos como la Teoría de Funcionales de la Densidad y métodos de Monte Carlo Cuántico, por ejemplo.

Especialmente en la física de la materia condensada (aunque no limitados a este campo), los sistemas cuánticos de muchos cuerpos en redes periódicas siempre tendrán un lugar importante. Esta tesis presenta un estudio de las propiedades del estado base de un gas unidimensional de bosones interactuantes, el cual se encuentra restringido espacialmente dentro de una red periódica compuesta por múltiples barras permeables, a temperatura cero. El análisis se hizo usando dos métodos complementarios. Primero, en el régimen débilmente interactuante usamos teoría de campo medio, es decir, resolvimos la ecuación de Gross-Pitaevskii. Después, para ir más allá del contexto de teoría de campo medio y analizar el efecto de interacciones repulsivas de magnitud arbitraria en el comportamiento cuántico del sistema, usamos técnicas *ab-initio* de Monte Carlo Cuántico.

En los Capítulos 1 y 2 damos una introducción a los conceptos físicos básicos sobre los gases de Bose. Introducimos el concepto de gas de Bose débilmente interactuante, y mostramos las condiciones bajo las cuales la teoría de campo medio inicialmente desarrollada para gases en tres dimensiones sigue siendo válida para gases en una dimensión. Siguiendo esta dirección deducimos la ecuación de Gross-Pitaevskii, que es una herramienta fundamental para el estudio de gases en el régimen débilmente interactuante. Enseguida damos una breve descripción del gas de Lieb-Liniger, modelo físico al cual se reduce nuestro sistema cuando suprimimos la red multibarras. Finalmente, damos una breve descripción de la teoría del líquido de Luttinger, la cual es fundamen-

tal para nuestro estudio de gases unidimensionales en regímenes fuertemente interactuantes donde la teoría de campo medio no es aplicable.

En el Capítulo 3, estudiamos el efecto de la red multibarras periódica, así como el impacto de las interacciones entre bosones, en la función de onda del condensado en el regimen débilmente interactuante. Para ello resolvemos la ecuación de Gross-Pitaevskii en 1D considerando que la función de onda del condensado se puede escribir como una onda de Bloch. De esta forma encontramos que la densidad del sistema puede expresarse analíticamente en términos de las funciones elípticas de Jacobi y las integrales elípticas incompletas de primero, segundo y tercer tipo. Además caracterizamos el espectro de energía del sistema, el potencial químico, la compresibilidad y la velocidad del sonido en el condensado. Finalmente, usamos nuestro modelo para predecir las propiedades de un gas de Bose atrapado en un nuevo tipo de redes ópticas que poseen una estructura espacial a una escala mucho menor que su propia longitud de onda, conocidas como "subwavelength optical lattices", las cuales han sido producidas experimentalmente en años recientes.

En el Capítulo 4 presentamos la teoría básica que fundamenta lo que se conoce como métodos de Monte Carlo Cuántico. Mostramos las características principales de los métodos Monte Carlo Variacional y Monte Carlo Difusivo, así como las principales diferencias entre ambos. Mostramos cómo mediante técnicas estocásticas ambos métodos son capaces de proveer información valiosa sobre las propiedades del estado base de un gas cuántico a temperatura cero para regímenes donde la teoría de campo medio es inaplicable. Especial atención merece el método Monte Carlo Difusivo pues es una técnica que nos permite calcular muchas propiedades físicas de manera exacta hasta un error estadístico que podemos calcular.

En el Capítulo 5 estudiamos las propiedades físicas de un gas de Bose con interacciones de corto alcance en una red multi-barras más allá del régimen de campo medio. Para ello empleamos los métodos Monte Carlo Variacional y Monte Carlo Difusivo para dicho análisis. Primero proponemos una función de onda de prueba adecuada para representar al estado base. Luego calculamos la energía del estado base como función de los parámetros de la red. Finalmente calculamos el factor de estructura estático del sistema y obtenemos el diagrama de fases a temperatura zero, donde delimitamos las fases superfluida y aislante de Mott como funciones de la magnitud de la interacción entre partículas y de la altura de las barreras de la red.

Finalmente en el Capítulo 6 damos una visión general de los principales resultados obtenidos, y discutimos algunos temas de investigación hacia el futuro relacionados con esta tesis.

Contents

1
Introduction

Ultracold bosonic and fermionic quantum gases have been a subject of intense research in the last few years after the experimental realization of Bose-Einstein condensation (BEC) in 1995 [1, 2]. These experiments were a milestone that transformed Bose and Einstein's mathematical predictions [3] in a physical reality. The technology to study cold matter has evolved enormously. Currently, physicists can realize Bose-Einstein condensates and other exotic quantum states with a significant degree of control on the system parameters using magneto-optical traps, optical lattices, and atom chips [4–8]. We have reached the point where experimental researchers can simulate [9–12] real quantum many-body systems in the laboratory by controlling most of its variables at will. In particular, these advances have opened the possibility to study the behavior of Fermi and Bose gases constrained in such ways that their movement is effectively quenched in two spatial directions, so they behave as one-dimensional [13–18] systems. Now it is possible to study the exotic behavior of one-dimensional quantum gases and verify theoretical predictions made long ago about them [19–22].

Describing the properties of quantum many-body systems is an extraordinarily hard task. Due to the combined effect of interactions between particles and the spatial constrictions, it is impossible to obtain, most of the time, the solution of the Schrödinger equation, i.e., the many-body wave function. It is possible, for example, in the one-dimensional world, for the ground state of the Tonks-Girardeau Bose gas [19, 23], the Lieb-Liniger model [24], and the Calogero model [25]. When solving the Schrödinger equation is not possible, we have to resort to approximations that are applicable only under reasonable assumptions.

The most common theoretical approach to study the properties of bosonic quantum many-body systems is the mean-field theory, i.e., solving the Gross-Pitaevskii equation [26, 27]. This approach assumes that the vast majority of the bosons occupy the same quantum state: the ground state, which is described by a wave function whose evolution is determined by a one-body, nonlinear partial differential equation: the Gross-Pitaevskii equation (GPE). In its basic form, the GPE is equivalent to the one-body Schrödinger equation plus an additional nonlinear term that accounts for the interactions between bosons. Despite its mathematical simplicity, the success of the GPE and the mean-field theory approach to model and predict the physical properties of weakly-interacting Bose gases [28] is inquestionable. However, for strongly correlated quantum systems like ^{4}He [29, 30], the mean-field approximation is inadequate, and complementary methods become necessary.

Quantum Monte Carlo (QMC) methods are an attractive alternative to calculate the ground-state properties of quantum many-body systems at zero or finite temperatures [31] with density and interactions of arbitrary magnitude. In particular, QMC methods are used to evaluate the expected values of quantum observables. In the coordinate representation, for instance, the expected value of the Hamiltonian on its ground state, i.e., the ground state energy of the system, is a multidimensional integral over a $3N$-dimensional space, being N the number of particles in the system. Numerical techniques commonly used to evaluate integrals in one dimension can be used in higher dimensions through cartesian products. However, this approach suffers from a severe problem: the time required to reach a given numerical accuracy increases exponentially with the dimension of the space. This problem is known as *the curse of dimensionality*. Monte Carlo methods, on the other hand, are stochastic algorithms whose rate of convergence is inversely proportional to the square root of the number of times an observable should be measured to obtain its expected value. Although it is a slow rate of convergence, it is independent of the space dimension. In a QMC calculation, one fixes the particle number to simulate a quantum system, and this number determines the size of the coordinate space. Even if the number of particle changes, the convergence rate of the algorithm remains the same.

Among the various QMC methods, the Variational Monte Carlo approach (VMC) is the most simple. It is based on the variational principle of quantum mechanics, so we can use it to obtain an approximate upper bound to the ground state energy of the system. The accuracy of this approximation depends on the quality of the trial wave function used to evaluate the expected value of the observable in question. A more sophisticated (and more complex) approach is the Diffusion Monte Carlo (DMC) method, a technique that solves the *imaginary-time Schrödinger equation* in small time intervals. By evolv-

ing an initial wave function repeatedly in small time steps, a DMC calculation yields estimates for the expected values of many observables that are exact up to a small, manageable stochastic error. Both VMC and DMC techniques have been used extensively to study strongly correlated quantum systems with great success [32–35].

In this thesis, we have used both mean-field and QMC approaches to study the properties of the ground state of a one-dimensional interacting Bose gas in a periodic, multi-rod lattice. The contents and results are organized in the following way:

In Chapter 2, we describe the fundamental theory of weakly-interacting, one dimensional Bose gases, also known as mean-field theory. In this chapter, we explain what defines a weakly-interacting Bose gas in 3D, and develop the mathematics that leads us to the famous Gross-Pitaevskii equation for a Bose gas within an inhomogeneous medium. Then, we establish the conditions under which the mean-field theory picture applies to one-dimensional systems, to finally obtain the one-dimensional version of the Gross-Pitaevskii equation. Afterward, we give a brief description of the Lieb-Liniger Bose gas (LL), a 1D system of major relevance in quantum many-body physics since it is an example of an exactly solvable model. Also, it is a system whose properties, especially the ground state energy, are relevant for the system we analyze in this thesis. Next, we give an overview of the Luttinger liquid theory: a formalism to describe the low-energy properties of one-dimensional bosonic and fermionic gases at very low temperatures. Finally, we give a summary of the experimental techniques used to manipulate cold atoms and Bose-Einstein condensates.

In Chapter 3, we show our research on the ground-state properties of the weakly-interacting 1D Bose gas within multi-rod lattices. A large part of this chapter is devoted to obtaining the solutions of the 1D GPE with an external Kronig-Penney (KP) potential. We establish the boundary conditions corresponding to periodic solutions in the form of Bloch waves. Remarkably, this type of solution can be determined analytically in terms of the Jacobi elliptic functions, as well as of the incomplete elliptic integrals of the first, second, and third kind. We show numerical results for the ground state density profile, energy spectrum, chemical potential, compressibility, and sound velocity. Finally, we use our model to predict some properties of ultracold BECs in optical lattices with a subwavelength structure [36, 37].

In Chapter 4, we show the statistical foundations of Monte Carlo integration techniques, how they are used to evaluate multidimensional integrals, and why their convergence rate is independent of the dimension of the space. Later, we depict the Metropolis-Hastings algorithm [38], a robust procedure to sample an arbitrary probability distribution function. Afterward, we describe the

Variational Monte Carlo method as an initial approach to analyze the ground-state properties of a quantum many-body system. Then, we show the basis of the Diffusion Monte Carlo method and depict the procedure to obtain the ground-state energy of a bosonic system. Also, we show some methods used to approximate the expected value of observables that do not commute with the Hamiltonian. Finally, we describe the so-called *Slater-Bijl-Jastrow* trial wave functions commonly used for QMC calculations.

In Chapter 5, we use QMC methods to analyze the ground-state properties of the 1D Bose gas with contact-like, repulsive interactions in multi-rods, beyond the weakly-interacting regime. First, we define the trial wave functions for the system. Then, we evaluate the ground state energy using both VMC and DMC when the KP potential vanishes since this case corresponds to the Lieb-Liniger gas, so that we can compare our results with the analytical predictions of the LL model [24]. Afterward, we introduce the KP potential and evaluate, in addition to the energy, the static structure factor using the method of *pure estimators* [33]. Knowledge of the static structure factor, together with results from the Luttinger liquid formalism, permits us to distinguish the quantum phases of the Bose gas in the case of unit-filling. Finally, we obtain the superfluid-Mott insulator phase diagram of the Bose gas as a function of the KP lattice height and the interaction magnitude between bosons.

In Chapter 6, we give an outlook about the results presented in this thesis, as well as some perspectives on future research topics.

Publications

During the course of this doctoral research, the following papers were published:

- O. A. Rodríguez, & M. A. Solís, "Universal Behavior of the BEC Critical Temperature for a Multi-slab Ideal Bose Gas", J. Low Temp. Phys. **183**, 144–151 (2016).

- Omar Abel Rodríguez-López, & M. A. Solís, "Periodic Ultranarrow Rods as 1D Subwavelength Optical Lattices", J. Low Temp. Phys. (2019), DOI: 10.1007/s10909-019-02276-6, arXiv:1907.12671v2

Earlier work

- Rodríguez, O. A. & Solís, M. A. "BEC and Dimensional Crossover in a Boson Gas Within Multi-slabs", J. Low Temp. Phys. **175**, 435–441 (2014).

2

One-Dimensional Bose Gases

In this chapter, we review several important concepts about one-dimensional degenerate Bose gases, as well as some theoretical approaches to study the properties of such systems.

2.1.   Systems of Identical Particles

The quantum mechanical behavior of a system of identical particles is very different than what classical physics predicts. Due to Heisenberg's uncertainty principle, there is no way any measurement can distinguish any pair of particles [39]. This *indistinguishability* has a major consequence: any measurable quantity must remain fixed when the positions of two particles are interchanged in the wave function, in particular, the probability density. If the wave function remains unchanged after exchanging any pair of identical particles, it is symmetric, and the system constituents are called *bosons*. On the other hand, if the wave function suffers a change of sign after exchanging of particles, it is antisymmetric, and the system constituents are called *fermions*.

Indistinguishability has an increasing role in quantum statistics when particles satisfy the *quantum degeneracy* condition

$$n\lambda_{\mathrm{dB}}^3 \sim 1. \tag{2.1}$$

Here, n is the average particle density and λ_{dB} is the *thermal de Broglie wavelength*,

$$\lambda_{\mathrm{dB}} = \sqrt{\frac{2\pi\hbar^2}{mk_{\mathrm{B}}T}}, \tag{2.2}$$

where m is the mass of the particles, T is the system temperature, k_B is the Boltzmann constant, and $\hbar = h/2\pi$. In the quantum degeneracy regime, the behavior of the system constituents depends on their type: bosons obey the Bose-Einstein statistics, while fermions follow the Fermi-Dirac statistics. Because of the Pauli exclusion principle, any two fermions can not occupy the same quantum state. On the other hand, bosons do not obey the Pauli exclusion principle, so many of them can occupy the same quantum state.

Back in 1924, A. Einstein [3], based on a previous work of S. N. Bose, predicted the appearance of a quantum phase transition nowadays known as *Bose-Einstein condensation* (BEC). This phenomenon occurs when the temperature of a Bose gas drops below a threshold known as Bose-Einstein condensation critical temperature. Under this condition, a significant fraction of particles occupies the lowest energy state, i.e., the ground-state. This state of matter is known as *Bose-Einstein condensate*, commonly referred through the BECacronym.

2.2. The Ideal Bose Gas

An ideal Bose gas obeys Bose-Einstein statistics. The mean occupation of a non-degenerate quantum state with energy E_k is

$$N(E_k) = \frac{1}{z^{-1}e^{\beta E_k} - 1}, \tag{2.3}$$

where $\beta = 1/k_B T$ and $z = \exp\left(\mu/k_B T\right)$ is the fugacity. The index k labels the quantum state. The total number of particles in the system is

$$N = \sum_k N(E_k) = \sum_k \frac{1}{z^{-1}e^{\beta E_k} - 1}. \tag{2.4}$$

In the thermodynamic limit, when $N \to \infty$ and the system volume $V \to \infty$, but the average density $n = N/V$ remains finite, the discrete energy spectrum E_k becomes a continuum spectrum, and the sums become integrals: $\sum_k \to V/(2\pi)^3 \int \mathrm{d}\boldsymbol{k}$. For a homogeneous ideal Bose gas, the particle energy is $E_k = \hbar^2 k^2/2m$, where $k = |\boldsymbol{k}|$. Then, the density equation Eq. (2.4) becomes

$$n = n_0 + \frac{1}{\lambda_{\mathrm{dB}}^3} g_{3/2}(z). \tag{2.5}$$

Here, $g_\nu(z)$ is the Bose-Einstein function

$$g_\nu(z) = \sum_{n=1}^{\infty} \frac{z^n}{n^\nu}, \tag{2.6}$$

also known as the Polylogarithm function. The term n_0 is the density of particles in the ground state with energy $E_0 = 0$,

$$n_0 = \frac{V^{-1}}{z^{-1} - 1} = \frac{N_0}{V} \implies N_0 = \frac{1}{z^{-1} - 1}, \tag{2.7}$$

while the second term of Eq. (2.5) is the density of particles distributed among the excited states: $n_{\text{exc}} = g_{3/2}(z)/\lambda_{\text{dB}}^3$.

Since the occupation number Eq. (2.3) must be positive, the chemical potential must be negative. Therefore, the fugacity must fulfill $0 < z < 1$. On the one hand, $z \to 0$ corresponds to the classical limit of very high temperatures. On the other hand, $z \to 1$ corresponds to the quantum degeneracy regime. This behavior has a significant consequence: the number of bosons distributed among the excited states $\boldsymbol{k} \neq \boldsymbol{0}$ is finite, and its value is such that

$$n_{\text{exc}} \leq \frac{1}{\lambda_{\text{dB}}^3} g_{3/2}(1), \tag{2.8}$$

with $g_{3/2}(1) = \zeta(3/2) \approx 2.612$, being $\zeta(\nu)$ the Riemann zeta function. For a fixed number of bosons N, there is a temperature T_{c} that saturates the excited states, exactly when n_{exc} equals the density of the whole gas,

$$n\lambda_{\text{dBc}}^3 = \zeta(3/2), \tag{2.9}$$

with $\lambda_{\text{dBc}} = \sqrt{2\pi\hbar/mk_{\text{B}}T_{\text{c}}}$. Since the particles are bosons, all of them that could not fit into the excited states will start to populate the ground state E_0, and they could represent a macroscopic fraction of the total; this event signals the occurrence of BEC phenomenon. Equation (2.9) fixes the critical temperature:

$$T_{\text{c}} = \frac{2\pi\hbar}{mk_{\text{B}}} \left(\frac{n}{\zeta(3/2)} \right)^{2/3}. \tag{2.10}$$

We recognize two possible scenarios [40]: for $T > T_{\text{c}}$, all the particles in the gas are distributed among the excited states. We refer to this situation as a *normal phase*. For $T < T_{\text{c}}$, a fraction of particles occupy excited states, and the rest occupy the ground state. This situation is known as the *condensed phase*.

2.2.1. The One-Dimensional Ideal Bose Gas

For an ideal homogeneous 1D Bose gas, one can find an expression for the density similar to the 3D one Eq. (2.5):

$$n_1 = \frac{1}{\lambda_{\text{dB}}} g_{1/2}(z). \tag{2.11}$$

Here, the number of particles distributed among excited states is proportional to $g_{1/2}(z)$. Since the term $g_{1/2}(z \to 1)$ diverges to infinite in the quantum degeneracy regime, there is not an upper bound for the number of particles distributed among excited states. Hence, the fraction of particles in the ground state never becomes significant, and Eq. (2.11) rules out Bose-Einstein condensation in a 1D homogeneous ideal Bose gas. We can still define a degeneracy temperature:

$$T_1^* = \frac{\hbar^2 n_1^2}{m k_{\mathrm{B}}}, \tag{2.12}$$

where $n_1 = N/L$ is the average one-dimensional density in a system with length L.

2.3. Long-Range Order

As we have seen, Bose-Einstein condensation occurs when a significant portion of particles populate the ground-state. A more formal criterion for the occurrence BEC, formulated by C. N. Yang [41], is directly related to the concept of *off-diagonal long-range order* (ODLRO). To illustrate the concept, we have to introduce the one-body density matrix (OBDM),

$$n^{(1)}(\boldsymbol{r}, \boldsymbol{r}') = \left\langle \hat{\boldsymbol{\Psi}}^\dagger(\boldsymbol{r}) \hat{\boldsymbol{\Psi}}(\boldsymbol{r}') \right\rangle, \tag{2.13}$$

where $\hat{\boldsymbol{\Psi}}^\dagger(\boldsymbol{r})$ is the quantum field operator that creates a particle at point $\boldsymbol{r}$. At the same time, $\hat{\boldsymbol{\Psi}}(\boldsymbol{r}')$ annihilates a particle at position $\boldsymbol{r}'$. These operators satisfy bosonic commutation relations,

$$\left[\hat{\boldsymbol{\Psi}}(\boldsymbol{r}), \hat{\boldsymbol{\Psi}}^\dagger(\boldsymbol{r}') \right] = \delta(\boldsymbol{r} - \boldsymbol{r}') \tag{2.14a}$$

$$\left[\hat{\boldsymbol{\Psi}}^\dagger(\boldsymbol{r}), \hat{\boldsymbol{\Psi}}^\dagger(\boldsymbol{r}') \right] = 0 \tag{2.14b}$$

$$\left[\hat{\boldsymbol{\Psi}}(\boldsymbol{r}), \hat{\boldsymbol{\Psi}}(\boldsymbol{r}') \right] = 0. \tag{2.14c}$$

Here, we implicitly assume that field operators, and consequently $n^{(1)}$, are time-dependent, i.e., $\hat{\boldsymbol{\Psi}}(\boldsymbol{r}) \equiv \hat{\boldsymbol{\Psi}}(\boldsymbol{r}, t)$. The one-body density matrix Eq. (2.13) contains relevant information about the system. In particular, its diagonal elements $\boldsymbol{r} = \boldsymbol{r}'$ give the density:

$$n(\boldsymbol{r}) = \left\langle \hat{\boldsymbol{\Psi}}^\dagger(\boldsymbol{r}) \hat{\boldsymbol{\Psi}}(\boldsymbol{r}) \right\rangle = n^{(1)}(\boldsymbol{r}, \boldsymbol{r}). \tag{2.15}$$

The total number of particles is

$$N = \int n(\boldsymbol{r}) \, d\boldsymbol{r}. \tag{2.16}$$

Yang relates the occurrence of BEC with the asymptotic behavior of the OBDM when $\|r - r'\| \to \infty$. If a BEC is present, then $n^{(1)}$ must have a large eigenvalue of order N, namely N_0, with a corresponding eigenfunction $\Psi_0(r, t)$, normalized to N_0, such that

$$n^{(1)}(r, r') \to \Psi_0^*(r, t)\Psi_0(r', t) \quad \text{if} \quad \|r - r'\| \to \infty. \tag{2.17}$$

This behavior can be taken as the definition of ODLRO, and the eigenfunction $\Psi_0(r, t)$ is taken as the *order parameter* of the condensate.

Yang's definition of long-range order does not seem suitable for finite systems. Instead, an alternative definition proposed by O. Penrose and L. Onsager [42] starts from the eigenvalues N_i of the OBDM, which are solutions of the equation

$$\int dr' \, n^{(1)}(r, r')\varphi_i(r') = N_i\varphi_i(r). \tag{2.18}$$

The single-particle functions $\varphi_i(r')$ are known as *natural orbitals*; they form a complete set of ortho-normalized functions such that

$$\sum_i \varphi_i^*(r)\varphi_i(r') = \delta(r - r'), \qquad \int dr \, \varphi_i^*(r)\varphi_j(r) = \delta_{ij}. \tag{2.19}$$

Hence, the normalization condition Eq. (2.16) is $N = \sum_i N_i$, and the diagonalized form of OBDM becomes

$$n^{(1)}(r, r') = \sum_i N_i \, \varphi_i^*(r)\varphi_i(r'). \tag{2.20}$$

Penrose and Onsager define BEC as the occurrence of one (and only one) single-particle state, referred to as the *condensed state*, whose eigenvalue is of the order of the total number of particles, let us say, $N_0 \sim N$.

The natural orbits determined by Eq. (2.18) provide an unambiguous basis to express the quantum field operator $\hat{\Psi}(r)$:

$$\hat{\Psi}(r) = \sum_i \varphi_i(r)\hat{a}_i, \tag{2.21}$$

where the operator $\hat{a}_i^\dagger$ ($\hat{a}_i$) creates (annihilates) a particle in the φ_i state. These operators satisfy bosonic commutation relations,

$$\left[\hat{a}_i, \hat{a}_j^\dagger\right] = \delta_{ij}, \quad [\hat{a}_i, \hat{a}_j] = \left[\hat{a}_i^\dagger, \hat{a}_j^\dagger\right] = 0. \tag{2.22}$$

Substituting Eq. (2.21) in Eq. (2.20), it follows that $\left\langle \hat{a}_j^\dagger \hat{a}_i \right\rangle = \delta_{ij} N_i$. It is convenient to split Eq. (2.21) as

$$\hat{\boldsymbol{\Psi}}(\boldsymbol{r}) = \varphi_0(\boldsymbol{r})\hat{\boldsymbol{a}}_0 + \sum_{i \neq 0} \varphi_i(\boldsymbol{r})\hat{\boldsymbol{a}}_i, \tag{2.23}$$

where the first term accounts for the particles in the condensed state, while the second represents condensed particles. If most of the particles occupy the ground-state and $N_0 = \left\langle \hat{a}_0^\dagger \hat{a}_0 \right\rangle \gg 1$, effectively forming a macroscopic BEC, then it becomes plausible to use the *Bogoliubov prescription*, which consists of replacing the operators $\hat{a}_0^\dagger$ and $\hat{a}_0$ by the c-number $\sqrt{N_0}$, neglecting their non-commutativity, as done originally by Bogoliubov [43]. Therefore, we can treat the condensed part $\varphi_0(\boldsymbol{r})\hat{\boldsymbol{a}}_0$ as a c-field, i.e., a classical field, so the field operator Eq. (2.23) becomes

$$\hat{\boldsymbol{\Psi}}(\boldsymbol{r}) = \Psi_0(\boldsymbol{r}) + \delta\hat{\boldsymbol{\Psi}}(\boldsymbol{r}), \tag{2.24}$$

where $\Psi_0(\boldsymbol{r}) = \sqrt{N_0}\varphi_0(\boldsymbol{r})$ and $\delta\hat{\boldsymbol{\Psi}}(\boldsymbol{r}) = \sum_{i \neq 0} \varphi_i(\boldsymbol{r})\hat{\boldsymbol{a}}_i$. The function $\Psi_0(\boldsymbol{r})$ in Eq. (2.24) can be identified as the order parameter of Yang's ODLRO criterion Eq. (2.17) since it is the eigenfunction of the OBDM with the largest eigenvalue of order N.

2.4. Weakly-Interacting Bose Gases

A weakly-interacting gas is a system such that the range of the inter-particle interactions is much smaller than the inter-particle distance. The previous assumption has important physical consequences; for example, collisions between two particles are described in terms of the asymptotic expression of the wave function at large inter-particle distances. When we consider gases close to zero temperature, or far below than its Bose-Einstein critical point, we can restrict to low values of the momenta. From scattering theory, it follows that the asymptotic wave function is entirely defined by lowest-order s-wave scattering length a_s. Hence, all the effects of the interaction on the physical properties of the bosons are defined by just one single parameter, a_s. For a system with N particles within a volume V, the average distance between them is roughly $d = n^{-1/3}$, where $n = N/V$ is the average density of the system. Then, the diluteness condition can be written as

$$|a_\mathrm{s}| \ll n^{-1/3}, \tag{2.25}$$

or equivalently, as $n|a_\mathrm{s}|^3 \ll 1$.

We start by writing the Hamiltonian of the homogeneous Bose gas in terms of creation and annihilation field operators $\hat{\boldsymbol{\Psi}}^{\dagger}(\boldsymbol{r})$ and $\hat{\boldsymbol{\Psi}}(\boldsymbol{r})$ [44, 45],

$$
\begin{aligned}
\hat{\boldsymbol{H}} = &-\frac{\hbar^2}{2m} \int \hat{\boldsymbol{\Psi}}^{\dagger}(\boldsymbol{r}) \nabla^2 \hat{\boldsymbol{\Psi}}(\boldsymbol{r}) \, d\boldsymbol{r} \\
&+ \frac{1}{2} \int \hat{\boldsymbol{\Psi}}^{\dagger}(\boldsymbol{r}) \hat{\boldsymbol{\Psi}}^{\dagger}(\boldsymbol{r}') V_{\text{int}}(\boldsymbol{r}' - \boldsymbol{r}) \hat{\boldsymbol{\Psi}}(\boldsymbol{r}') \hat{\boldsymbol{\Psi}}(\boldsymbol{r}) \, d\boldsymbol{r}' d\boldsymbol{r},
\end{aligned}
\tag{2.26}
$$

where $V_{\text{int}}(\boldsymbol{r}' - \boldsymbol{r})$ is the inter-particle interaction potential. These operators satisfy the canonical commutation relations Eq. (2.14). For a system with volume V, we can express the creation field operator as a linear combination of single-particle creation operators of bosons with momentum $\boldsymbol{p}$, times a plane wave,

$$
\hat{\boldsymbol{\Psi}}(\boldsymbol{r}) = \sum_{\boldsymbol{p}} \hat{\boldsymbol{a}}_{\boldsymbol{p}} \frac{1}{\sqrt{V}} e^{i\boldsymbol{p}\cdot\boldsymbol{r}/\hbar}.
\tag{2.27}
$$

Substituting this expression in Eq. (2.26), we arrive at the following result,

$$
\hat{\boldsymbol{H}} = \sum_{\boldsymbol{p}} \frac{p^2}{2m} \hat{\boldsymbol{a}}_{\boldsymbol{p}}^{\dagger} \hat{\boldsymbol{a}}_{\boldsymbol{p}} + \frac{1}{2V} \sum_{\boldsymbol{p}_1, \boldsymbol{p}_2} \sum_{\boldsymbol{p}'} U_{\boldsymbol{p}'} \hat{\boldsymbol{a}}_{\boldsymbol{p}_1 + \boldsymbol{p}'}^{\dagger} \hat{\boldsymbol{a}}_{\boldsymbol{p}_2 - \boldsymbol{p}'}^{\dagger} \hat{\boldsymbol{a}}_{\boldsymbol{p}_2} \hat{\boldsymbol{a}}_{\boldsymbol{p}_1},
\tag{2.28}
$$

where

$$
U_{\boldsymbol{p}'} = \int d\boldsymbol{r} \, V_{\text{int}}(\boldsymbol{r}) e^{-i\boldsymbol{p}'\cdot\boldsymbol{r}/\hbar}
\tag{2.29}
$$

and

$$
[\hat{\boldsymbol{a}}_{\boldsymbol{p}}, \hat{\boldsymbol{a}}_{\boldsymbol{p}'}^{\dagger}] = \delta_{\boldsymbol{p},\boldsymbol{p}'} \quad \text{and} \quad [\hat{\boldsymbol{a}}_{\boldsymbol{p}}, \hat{\boldsymbol{a}}_{\boldsymbol{p}'}] = [\hat{\boldsymbol{a}}_{\boldsymbol{p}}^{\dagger}, \hat{\boldsymbol{a}}_{\boldsymbol{p}'}^{\dagger}] = 0.
\tag{2.30}
$$

The r.h.s. in Eq. (2.29) is proportional to the scattering amplitude, or scattering length, in the first Born approximation [44],

$$
a_{\text{s}} = \frac{m^*}{2\pi\hbar^2} \int d\boldsymbol{r} \, V_{\text{int}}(\boldsymbol{r}) e^{-i\boldsymbol{p}'\cdot\boldsymbol{r}/\hbar},
\tag{2.31}
$$

where $m^* = m/2$ is the reduced mass of a pair of interacting bosons. For low momenta, we only have to consider the case $\boldsymbol{p}' = 0$; hence

$$
a_{\text{s}} = \frac{m}{4\pi\hbar^2} \int d\boldsymbol{r} \, V_{\text{int}}(\boldsymbol{r}).
\tag{2.32}
$$

Previously, we have emphasized that in virtue of the diluteness criterion, the physics of the system depends only on the scattering-length a_{s}, not in the shape of the two-body potential. Following Eq. (2.32) and Eq. (2.29), we get that

$$
U_{\boldsymbol{p}'=\boldsymbol{0}} = \frac{4\pi\hbar^2 a_{\text{s}}}{m},
\tag{2.33}
$$

so the Hamiltonian reduces to

$$\hat{H} = \sum_{\boldsymbol{p}} \frac{p^2}{2m}\hat{a}_{\boldsymbol{p}}^{\dagger}\hat{a}_{\boldsymbol{p}} + \frac{U_{\boldsymbol{p}'=\boldsymbol{0}}}{2V}\sum_{\boldsymbol{p}_1,\boldsymbol{p}_2} \hat{a}_{\boldsymbol{p}_1}^{\dagger}\hat{a}_{\boldsymbol{p}_2}^{\dagger}\hat{a}_{\boldsymbol{p}_2}\hat{a}_{\boldsymbol{p}_1}, \tag{2.34}$$

We see that the explicit dependence of the two-body potential is not present anymore, but is implicit in the value of $U_{\boldsymbol{p}'=\boldsymbol{0}}$.

The theory of dilute gases assumes the Bogoliubov prescription. Under this premise, we replace the creation and annihilation operators by c-numbers:

$$\hat{a}_{\boldsymbol{0}} = \sqrt{N_{\boldsymbol{0}}}, \tag{2.35}$$

where $N_{\boldsymbol{0}} \gg 1$ is the number of bosons in the ground state of the system. We consider that the system temperature is far below the BEC critical temperature. Hence, it is reasonable to assume that the occupation of states with momenta $\boldsymbol{p} \neq \boldsymbol{0}$, although nonzero, it is negligible compared to the occupation of the ground state. Consequently, practically all the N bosons in the system occupy the ground state. Then $N_{\boldsymbol{0}} \sim N$, $\hat{a}_{\boldsymbol{0}} \sim \sqrt{N}$, and only the ground state will contribute to the second term of Eq. (2.34). At the same time, the first term of Hamiltonian will be zero as it depends on p^2. The ground-state energy of the system is

$$E_{\boldsymbol{0}} = \frac{1}{2}\frac{N^2 U_{\boldsymbol{p}=\boldsymbol{0}}}{V}. \tag{2.36}$$

In terms of the density n, the energy of the ground state becomes

$$E_{\boldsymbol{0}} = \frac{1}{2}gnN, \tag{2.37}$$

where

$$g = \frac{4\pi\hbar^2 a_{\mathrm{s}}}{m} \tag{2.38}$$

is a parameter that measures the interaction strength. Therefore the chemical potential is

$$\mu = \left(\frac{\partial E_{\boldsymbol{0}}}{\partial N}\right)_{S,V} = gn. \tag{2.39}$$

Unlike a noninteracting Bose gas, the chemical potential is nonzero but is proportional g times the density. As expected, the chemical potential corresponds to the ideal Bose gas result when the interaction vanishes.

The pressure of the Bose gas is related to its internal energy as

$$p = -\left(\frac{\partial E_0}{\partial V}\right)_{S,N} = \frac{gn^2}{2}. \tag{2.40}$$

Unlike the IBG, in general, the weakly-interacting Bose gas pressure is nonzero. Its compressibility is

$$\kappa = -\frac{1}{V}\left(\frac{\partial V}{\partial p}\right)_S = \frac{1}{gn^2}, \tag{2.41}$$

which is finite except for $g \to 0$ since it diverges. Finally, the sound velocity in the gas is

$$c_{\mathrm{s}} \equiv \frac{1}{\sqrt{\kappa n m}} = \sqrt{\frac{gn}{m}}. \tag{2.42}$$

2.4.1. Inhomogeneous Bose Gases

Now we proceed to look into the properties of the weakly-interacting Bose gas subject to an external potential. Our starting is the many-body Hamiltonian in second quantized form,

$$\hat{\boldsymbol{H}} = \int \hat{\boldsymbol{\Psi}}^\dagger(\boldsymbol{r})\hat{\boldsymbol{h}}_0(\boldsymbol{r})\hat{\boldsymbol{\Psi}}(\boldsymbol{r}) \ d\boldsymbol{r}$$
$$+ \frac{1}{2}\int \hat{\boldsymbol{\Psi}}^\dagger(\boldsymbol{r})\hat{\boldsymbol{\Psi}}^\dagger(\boldsymbol{r}')V_{\mathrm{int}}(\boldsymbol{r}' - \boldsymbol{r})\hat{\boldsymbol{\Psi}}(\boldsymbol{r}')\hat{\boldsymbol{\Psi}}(\boldsymbol{r}) \ d\boldsymbol{r}'d\boldsymbol{r}. \tag{2.43}$$

The operator $\hat{\boldsymbol{h}}_0(\boldsymbol{r})$ is the Hamiltonian of the noninteracting Bose gas subject to an external potential $V_{\mathrm{ext}}(\boldsymbol{r})$:

$$\hat{\boldsymbol{h}}_0(\boldsymbol{r}) = -\frac{\hbar^2}{2m}\nabla^2 + V_{\mathrm{ext}}(\boldsymbol{r}). \tag{2.44}$$

Previously, in virtue of the diluteness criterion, we concluded that interactions between bosons are determined entirely by the s-wave scattering length a_{s}. The shape of the interaction potential does not matter, as long as it yields the correct value of the scattering length. So, we can replace the physical two-body interaction potential $V_{\mathrm{int}}(\boldsymbol{r})$ in Eq. (2.32) with an effective potential that gives the correct value of the scattering length. This effective interaction has the form of a contact pseudo-potential:

$$V_{\mathrm{int}}(\boldsymbol{r} - \boldsymbol{r}') = g\delta(\boldsymbol{r} - \boldsymbol{r}'), \tag{2.45}$$

where $g = 4\pi\hbar^2 a_{\mathrm{s}}/m$, as defined in Eq. (2.38), measures the strength of the contact interaction. Direct substitution of Eq. (2.45) in Eq. (2.32) shows the consistency of this definition. Then, the many-body Hamiltonian subject to the potential Eq. (2.45) becomes

$$\hat{\boldsymbol{H}} = \int \hat{\boldsymbol{\Psi}}^\dagger(\boldsymbol{r})\hat{\boldsymbol{h}}_0(\boldsymbol{r})\hat{\boldsymbol{\Psi}}(\boldsymbol{r})\,d\boldsymbol{r} + \frac{g}{2}\int \hat{\boldsymbol{\Psi}}^\dagger(\boldsymbol{r})\hat{\boldsymbol{\Psi}}^\dagger(\boldsymbol{r})\hat{\boldsymbol{\Psi}}(\boldsymbol{r})\hat{\boldsymbol{\Psi}}(\boldsymbol{r})d\boldsymbol{r}. \quad (2.46)$$

We can get the evolution of the creation field operator $\hat{\boldsymbol{\Psi}}(\boldsymbol{r}, t)$ as a function of time from Heisenberg's equation:

$$i\hbar\frac{\partial\hat{\boldsymbol{\Psi}}(\boldsymbol{r}, t)}{\partial t} = \left[\hat{\boldsymbol{\Psi}}(\boldsymbol{r}, t), \hat{\boldsymbol{H}}(t)\right]. \quad (2.47)$$

The Hamiltonian Eq. (2.46) is a function of time, i.e., $\hat{\boldsymbol{H}} \equiv \hat{\boldsymbol{H}}(t)$, though we have omitted it explicitly. Hence, the time evolution of the field operator is

$$i\hbar\frac{\partial\hat{\boldsymbol{\Psi}}(\boldsymbol{r}, t)}{\partial t} = \hat{\boldsymbol{h}}_0\hat{\boldsymbol{\Psi}}(\boldsymbol{r}, t) + g\,\hat{\boldsymbol{\Psi}}^\dagger(\boldsymbol{r}, t)\hat{\boldsymbol{\Psi}}(\boldsymbol{r}, t)\hat{\boldsymbol{\Psi}}(\boldsymbol{r}, t). \quad (2.48)$$

Analogously to the study of the interacting homogeneous Bose gas, we assume that a macroscopic number of bosons occupy the ground state of the system. Then we can use the Bogoliubov prescription for the field operator, $\hat{\boldsymbol{\Psi}}(\boldsymbol{r}, t) = \Psi(\boldsymbol{r}, t) + \delta\hat{\boldsymbol{\Psi}}(\boldsymbol{r}, t)$, according to Eq. (2.24). The classical field $\Psi(\boldsymbol{r}, t)$ represents the wave function of the condensed bosons as a whole, and it is also the order parameter of the BEC. If we neglect quantum fluctuations accounted by the term $\delta\hat{\boldsymbol{\Psi}}(\boldsymbol{r}, t)$, we arrive at the famous Gross-Pitaevskii equation (GPE) [26, 27]:

$$i\hbar\frac{\partial\Psi(\boldsymbol{r}, t)}{\partial t} = \left(-\frac{\hbar^2}{2m}\nabla^2 + V_{\mathrm{ext}}(\boldsymbol{r}) + g\left|\Psi(\boldsymbol{r}, t)\right|^2\right)\Psi(\boldsymbol{r}, t). \quad (2.49)$$

The GPE governs the dynamics of the condensate. It resembles the one-particle Schrödinger equation, with an additional nonlinear term proportional to the square of the condensate wave function, which accounts for the interactions between bosons. In this sense, Eq. (2.49) is a mean-field equation. Then, we define the Gross-Pitaevskii Hamiltonian as

$$\hat{\boldsymbol{H}}_{\mathrm{GP}} = -\frac{\hbar^2}{2m}\nabla^2 + V_{\mathrm{ext}}(\boldsymbol{r}) + g\left|\Psi(\boldsymbol{r}, t)\right|^2, \quad (2.50)$$

so Eq. (2.49) becomes

$$i\hbar\frac{\partial\Psi(\boldsymbol{r}, t)}{\partial t} = \hat{\boldsymbol{H}}_{\mathrm{GP}}\Psi(\boldsymbol{r}, t). \quad (2.51)$$

The assumption that most bosons occupy the ground state allows us to assert that the condensate density is the Bose gas density, i.e.,

$$n(\boldsymbol{r}) = |\Psi(\boldsymbol{r},t)|^2\,, \tag{2.52}$$

and the total number of bosons N is

$$N = \int n(\boldsymbol{r})\,d\boldsymbol{r}. \tag{2.53}$$

This equation is referred to as the normalization condition. Substituting the Bogoliubov prescription Eq. (2.24) in the Hamiltonian Eq. (2.46) and neglecting quantum fluctuations, we obtain the energy of the condensate:

$$E[\Psi] = \frac{\hbar^2}{2m} \int d\boldsymbol{r}\, |\nabla \Psi(\boldsymbol{r},t)|^2 \\ + \int d\boldsymbol{r}\, V_{\text{ext}}(\boldsymbol{r})|\Psi(\boldsymbol{r},t)|^2 + \frac{g}{2} \int d\boldsymbol{r}\, |\Psi(\boldsymbol{r},t)|^4. \tag{2.54}$$

Solutions of Eq. (2.51) subject to the normalization condition Eq. (2.53) describe the ground-state properties of the weakly-interacting Bose gas at zero temperature. The normalization condition fixes the chemical potential μ of the condensate, which is related to the energy by

$$\mu = \left(\frac{\partial E}{\partial N}\right)_{S,V}. \tag{2.55}$$

The Gross-Pitaevskii equation is considered the primary theoretical tool to describe phenomena that occurs for weakly-interacting Bose gases at extremely low temperatures, like in many of nowadays experiments realized in ultracold atomic gases (see Section 3.1). Among the kind of solutions of the GPE, one can find localized solutions like *solitons* in one, two, and three dimensions [46–48], and even Bloch waves [49–51]. Also, there is a whole industry dedicated to studying the dynamics and properties of Bose-Einstein condensates using numerical techniques to solve the time-dependent GPE [52–56].

Equation Eq. (2.49) has a particular set of states that evolve in time in the form

$$\Psi(\boldsymbol{r},t) = \Phi(\boldsymbol{r})e^{-i\mu t/\hbar}, \tag{2.56}$$

where the chemical potential fixes the time dependence of the wave function. States defined by Eq. (2.56) are called *stationary* since they decouple the time dependence from the spatial dependence. Then, Eq. (2.51) takes form of

$$\hat{\boldsymbol{H}}_{\text{GP}}\Phi(\boldsymbol{r}) = \mu\Phi(\boldsymbol{r}). \tag{2.57}$$

Equation (2.57) is the stationary Gross-Pitaevskii equation, and it looks very similar to the stationary one-particle Schrödinger equation. However, it is a nonlinear equation, due to the term proportional to the condensate density in Eq. (2.50). For this reason, the GPE is known as the Nonlinear Schrödinger equation (NLSE) in many contexts. Also, the chemical potential plays the role of eigenvalue of $\hat{\boldsymbol{H}}_{\mathrm{GP}}$ instead of the energy per particle. Only in the case when the interaction is zero, both chemical potential and ground-state energy (per particle) are equal.

2.5. Mean-Field Theory in One Dimension

The theory of dilute gases described in the previous section was developed for a three-dimensional system. However, with nowadays experimental techniques, it is possible to confine a Bose fluid within highly anisotropic potentials that effectively constrain the movement of the particles in two or even in one spatial dimension [13, 21, 57].

One criterion to discard or assert the applicability of mean-field theory for a homogeneous Bose gas is that the average distance between bosons should be smaller than the healing length ξ of the gas [45],

$$\xi = \frac{\hbar}{\sqrt{2}mc_{\mathrm{s}}} = \frac{\hbar}{\sqrt{2mgn}}. \tag{2.58}$$

Here, c_{s} is the sound velocity in the fluid (see Eq. (2.42)), and g is the interaction strength factor (see Eq. (2.38)). The average distance d between particles can be estimated in terms of the average density n roughly as $d \sim n^{-1/3}$. Then, following the definition of g, we obtain

$$\frac{\xi}{d} \sim \frac{1}{\sqrt{8\pi a_{\mathrm{s}}d^{-1}}} = \frac{1}{\sqrt{8\pi(a_{\mathrm{s}}n^{1/3})}}, \tag{2.59}$$

with a_{s} being the s-wave scattering length. We observe that the ratio ξ/d is proportional to $(na_{\mathrm{s}}^3)^{-1/6}$, so the condition $\xi > d$ is well satisfied for small densities. However, if we change the geometry of the system and reduce the dimension, the situation changes completely.

Let us consider a Bose gas of N bosons confined in a cylindrical geometry of length L produced by a harmonic trap with a frequency $\omega_{\perp}$ in the transverse (radial) direction and frequency ω_z in the axial direction. A very elongated trap, i.e., a cigar-shaped trap, is obtained with $\omega_{\perp} \gg \omega_z$. We define the linear density as $n_1 = N/L$. Therefore, the average linear density n_1 is related to the

three-dimensional density n through

$$n_1 = n\pi a_\perp^2, \tag{2.60}$$

where $a_\perp = \sqrt{\hbar/m\omega_\perp}$ is the oscillation length of the transverse harmonic trapping potential $V(r_\perp) = m\omega_\perp^2 r_\perp^2/2$. The average three-dimensional density n is measured at $r_\perp = 0$. In this one-dimensional geometry generated by the trapping potential, the distance between particles in terms of the linear density is $d = n_1^{-1}$, so the quotient ξ/d becomes

$$\frac{\xi}{d} = \sqrt{\frac{a_\perp^2}{8a_s}n_1}. \tag{2.61}$$

We see that this quotient becomes smaller as the linear density decreases; this means that the mean-field theory developed in the previous section becomes inadequate for diluted systems with a one-dimensional geometry. Nevertheless, there is the possibility that the healing length ξ becomes larger than the average interparticle distance d if

$$n_1 \frac{a_\perp^2}{a_s} \gg 1, \tag{2.62}$$

for instance, when the linear density is sufficiently large.

A system with cylindrical geometry, as described before, has two notable regimes [45]. If $n_1 a_s \gg 1$, the system enters in the radial Thomas-Fermi regime or *three-dimensional cigar*, where the system locally retains its three-dimensional nature, although geometrically looks one-dimensional. Our primary interest is the *one-dimensional mean-field regime*, $n_1 a_s \ll 1$, where only the ground state of the harmonic trapping potential in the radial direction contributes to the chemical potential:

$$\mu = \hbar\omega_\perp(1 + 2a_s n_1) = \mu_\perp + \mu_{1D}. \tag{2.63}$$

The constant term $\mu_\perp = \hbar\omega_\perp$ arises from the zero-point motion in the transverse direction, while the second term is the chemical potential of the weakly-interacting Bose gas in the one-dimensional mean-field regime:

$$\mu_{1D} = 2a_s n_1 \hbar\omega_\perp. \tag{2.64}$$

Looking back to Eq. (2.62), we can introduce a *one-dimensional scattering length*:

$$a_{1D} = -\frac{a_\perp^2}{a_s}. \tag{2.65}$$

Then, the relevant condition that must be fulfilled to apply mean-field theory in one-dimension is

$$n_1|a_{1D}| \gg 1. \tag{2.66}$$

Here, the factor $n_1|a_{1D}|$ is known as the *gas parameter*. We must note that condition Eq. (2.66) is only guaranteed if the ratio $a_\perp/a_s$ is sufficiently large. Only in this case the condition $n_1 a_s \ll 1$ required to reach the one-dimensional mean-field regime is consistent with Eq. (2.66). Considering the previous arguments, the limit of high densities always corresponds to the 1D mean-field regime.

Following the definitions of the one-dimensional scattering length a_{1D}, the linear density n_1, and the transverse radius $a_\perp$, we find

$$\mu_{1D} = \frac{2\hbar^2 a_s}{ma_\perp^2}n_1 = -\frac{2\hbar^2}{ma_{1D}}n_1. \tag{2.67}$$

From Eq. (2.55), we obtain the energy of the Bose gas:

$$E = -\frac{\hbar^2}{ma_{1D}}n_1 N. \tag{2.68}$$

Equations (2.67) and (2.68) have the same mathematical form as Eqs. (2.39) and (2.37) for the three-dimensional mean-field regime, provided that we define an equivalent interaction parameter g_{1D} for one-dimensional systems as

$$g_{1D} = -\frac{2\hbar^2}{ma_{1D}}. \tag{2.69}$$

Immediately, we obtain

$$E = \frac{1}{2}g_{1D}n_1 N \tag{2.70}$$

$$\mu_{1D} = g_{1D}n_1. \tag{2.71}$$

2.5.1. 1D Mean-Field Equation

As we saw in the previous section, 1D Bose gases are experimentally realized through a very elongated, cigar-like harmonic trap. Such a trap "froze" the dynamics of the particles in the radial direction, and only the lowest energy state in the radial direction contributes to the total chemical potential of the system, as shown in Eq. (2.63). Under this premise, the lowest transverse state is

the ground state of a 2D harmonic oscillator with frequency $\omega_\perp$ in both x and y directions,

$$\Psi_{\mathrm{T}}(x,y) = \sqrt{\frac{m\omega_\perp}{\pi\hbar}} e^{-m\omega_\perp(x^2+y^2)/2\hbar}. \tag{2.72}$$

Due to the intense trapping in the radial direction, the wave function of the system Eq. (2.51) factorizes as

$$\Psi(\boldsymbol{r},t) = e^{-i\omega_\perp t}\Psi_{\mathrm{T}}(x,y)\Psi_{\mathrm{1D}}(z,t). \tag{2.73}$$

The phase $e^{-i\omega_\perp t}$ corresponds to a time evolution with an energy $\mu_\perp = \hbar\omega_\perp$, i.e., the lowest contribution to the chemical potential of the transverse state Eq. (2.72). At the same time, the axial part of the wave function, i.e., $\Psi_{\mathrm{1D}}(z,t)$, models the dynamics of the 1D Bose gas. Substituting Eq. (2.73) in the 3D GPE (2.49), then multiplying by $\Psi_{\mathrm{T}}(x,y)$, and finally integrating over the x-y plane, we find that the function $\Psi_{\mathrm{1D}}(z,t)$ is governed by the differential equation

$$i\hbar\frac{\partial\Psi_{\mathrm{1D}}(z,t)}{\partial t} = \hat{\boldsymbol{H}}_{\mathrm{GP}_{\mathrm{1D}}}\Psi_{\mathrm{1D}}(z,t), \tag{2.74}$$

where $\hat{\boldsymbol{H}}_{\mathrm{GP}_{\mathrm{1D}}}(z,t)$ is the one-dimensional Gross-Pitaevskii Hamiltonian,

$$\hat{\boldsymbol{H}}_{\mathrm{GP}_{\mathrm{1D}}} = -\frac{\hbar^2}{2m}\frac{\partial^2}{\partial z^2} + V_{\mathrm{ext}}(z) + g_{\mathrm{1D}}\left|\Psi_{\mathrm{1D}}(z,t)\right|^2. \tag{2.75}$$

We note that the equation Eq. (2.74) has the same structure as Eq. (2.51) for a 3D system, but with a different interaction parameter g_{1D} (see Eq. (2.69)) due to the presence of the trap in the transverse direction. Not surprisingly, the 1D energy functional (relative to the zero-point energy) has the same structure as Eq. (2.54), i.e.,

$$
\begin{aligned}
E[\Psi_{\mathrm{1D}}] = {} & \frac{\hbar^2}{2m}\int\left|\frac{\partial\Psi_{\mathrm{1D}}(z,t)}{\partial z}\right|^2 dz \\
& + \int V_{\mathrm{ext}}(z)\left|\Psi_{\mathrm{1D}}(z,t)\right|^2 dz + \frac{g_{\mathrm{1D}}}{2}\int\left|\Psi_{\mathrm{1D}}(z,t)\right|^4 dz,
\end{aligned}
\tag{2.76}
$$

Also, the wave function is subject to the normalization condition

$$\int\left|\Psi_{\mathrm{1D}}(z,t)\right|^2 dz = N. \tag{2.77}$$

As in the 3D case, we can replace the interaction potential by an effective two-body pseudo-potential between any pair of bosons:

$$V(z - z') = g_{1D}\delta(z - z').$$ (2.78)

The stationary states of Eq. (2.74), which evolve in time according to

$$\Psi_{1D}(z, t) = \Phi_{1D}(z)e^{-i\mu_{1D}t/\hbar},$$ (2.79)

are governed by the stationary 1D Gross-Pitaevskii equation,

$$\hat{\boldsymbol{H}}_{GP_{1D}}(z)\Phi_{1D}(z) = \mu_{1D}\Phi_{1D}(z),$$ (2.80)

where $\Phi_{1D}(z)$ contains the spatial dependence of the ground-state wave function of the gas, μ_{1D} is the chemical potential, and

$$\hat{\boldsymbol{H}}_{GP_{1D}} = -\frac{\hbar^2}{2m}\frac{\partial^2}{\partial z^2} + V_{\text{ext}}(z) + g_{1D}\left|\Phi_{1D}(z)\right|^2,$$ (2.81)

since $|\Psi_{1D}(z, t)|^2 = |\Phi_{1D}(z)|^2$. Analogously to the 3D case (see Eq. (2.77)), the normalization condition becomes

$$\int |\Phi_{1D}(z)|^2\ dz = N.$$ (2.82)

The procedure described in this section corresponds to a dimensional reduction of the 3D GPE to one dimension considering harmonic trapping potentials. The method can also be used for two-dimensional Bose gases [58], and even for particles with long-range interactions, as the dipole-dipole case [59].

2.6. BEC and Long-Range Order in One Dimension

In Section 2.5, we analyzed the applicability of mean-field formalism in 1D systems, and finally, we arrived at the 1D Gross-Pitaevskii equation Eq. (2.74). Our starting point was the 3D mean-field formalism; hence, during this study, we assumed the existence of a BEC. However, the Mermin-Wagner-Hohenberg theorem [60, 61] rules out Bose-Einstein condensation in uniform, weakly-interacting 2D and 1D Bose gases at finite temperature; in 1D, there is no BEC even at zero temperature. Phase fluctuations accounted by $\delta\hat{\Psi}$ in Eq. (2.23) destroy long-range order, and they are the cause of BEC's absence. Trapped Bose gases in low-dimensional geometries with nowadays experimental techniques are not certainly uniform, so the Mermin-Wagner-Hohenberg theorem does not

necessarily hold. However, it is worthwhile to discuss some differences between BEC in lower dimensions compared to three dimensions, where ODLRO and BEC exist at sufficiently low temperatures for dilute Bose gases.

It is possible to analyze the properties of low-dimensional Bose gases, as well as the possibility of BEC, through the *density-phase* representation of the quantum field operator. In this framework, one expresses the field operator as

$$\hat{\boldsymbol{\Psi}}^{\dagger}(\boldsymbol{r}) = \sqrt{\hat{\boldsymbol{n}}(\boldsymbol{r})}\, e^{-i\hat{\boldsymbol{\theta}}(\boldsymbol{r})}, \quad \left[\hat{\boldsymbol{n}}(\boldsymbol{r}), \hat{\boldsymbol{\theta}}(\boldsymbol{r}')\right] = i\delta(\boldsymbol{r} - \boldsymbol{r}'), \tag{2.83}$$

where $\hat{\boldsymbol{n}}(\boldsymbol{r})$ and $\hat{\boldsymbol{\theta}}(\boldsymbol{r})$ are the density and phase operators, respectively. We can assume small density fluctuations, that is, representing the density operator as

$$\hat{\boldsymbol{n}}(\boldsymbol{r}) = n(\boldsymbol{r}) + \delta\hat{\boldsymbol{n}}(\boldsymbol{r}). \tag{2.84}$$

Here, $n(\boldsymbol{r})$ is the mean density profile, and $\delta\hat{\boldsymbol{n}}(\boldsymbol{r})$ accounts for density fluctuations. Substituting Eq. (2.83) into the into Eq. (2.48), it is shown [62–65] that at zero order in $\delta\hat{\boldsymbol{n}}$, the mean density $n(\boldsymbol{r})$ satisfies the Gross-Pitaevskii equation

$$-\frac{\hbar^2}{2m} \frac{\nabla^2 \sqrt{n(\boldsymbol{r})}}{\sqrt{n(\boldsymbol{r})}} + V_{\text{ext}}(\boldsymbol{r}) + gn(\boldsymbol{r}) = \mu, \tag{2.85}$$

where the chemical potential is fixed by the normalization condition

$$\int d\boldsymbol{r}\; n(\boldsymbol{r}) = N. \tag{2.86}$$

Results indicate that if we assume small density fluctuations, the particles form a BEC with a mean density profile $n(\boldsymbol{r})$ given by the GPE Eq. (2.85). For a weakly-interacting Bose gas trapped in 1D geometries, density fluctuations become negligible for $T \ll T_1^*$ [44, 62], where $T_1^* = \hbar^2 n_1^2 / mk_{\text{B}}$ is the quantum degeneracy temperature Eq. (2.12) we defined in Section 2.2.1, being n_1 the average linear density.

Even if density fluctuations are strongly suppressed at low temperatures, phase fluctuations can not always be neglected. Commonly, in this situation, it is said that the system is a *quasicondensate*, i.e., a condensate with a fluctuating phase [62, 63, 66–68]. To observe the effects of phase fluctuations on the asymptotic behavior of the OBDM, let us take a uniform 1D weakly-interacting Bose gas at $T = 0$. At low temperatures, neglecting density fluctuations, we have [62, 63]

$$n^{(1)}(r) = n^{(1)}(z, z') = n_1 \exp\left(-\frac{1}{2}\left\langle\left[\hat{\boldsymbol{\theta}}(z) - \hat{\boldsymbol{\theta}}(z')\right]^2\right\rangle\right), \tag{2.87}$$

21

where $r = |z - z'|$. The behavior of $n^{(1)}(r)$ when $r \to \infty$ gives the following expression for the phase correlator [45]:

$$\left\langle \left[\hat{\boldsymbol{\theta}}(z) - \hat{\boldsymbol{\theta}}(z') \right]^2 \right\rangle \sim \frac{mc_{\mathrm{s}}}{\pi\hbar n_1} \ln \left(\frac{r}{\xi} \right), \tag{2.88}$$

where $\xi = \hbar/\sqrt{2}mc_{\mathrm{s}}$ is the healing length (see Eq. (2.59)), and $c_{\mathrm{s}} = \sqrt{\mu_{1\mathrm{D}}/m}$ is the sound velocity. Expression Eq. (2.88) implies that, for distances much larger than the healing length, the zero-temperature OBDM decays as a power law, i.e.,

$$n^{(1)}(r) \propto \left(\frac{r}{\xi} \right)^{-\alpha}, \tag{2.89}$$

with exponent

$$\alpha = \frac{mc_{\mathrm{s}}}{2\pi\hbar n_1}. \tag{2.90}$$

Hence, Eq. (2.89) implies that there is no ODLRO, so the gas is not a true Bose-Einstein condensate. Nevertheless, the 1D Bose gas forms a quasicondensate.

For finite low-dimensional Bose gases, both analytical and experimental results show that BEC is possible. Remarkably, Ketterle and van Druten prove the occurrence of BEC in a finite, 1D noninteracting Bose gas within a harmonic trap [69]. Moreover, density and phase fluctuations do not necessarily destroy ODLRO in weakly-interacting trapped Bose gases; the trapping potential suppresses quantum fluctuations. Hence, a true BEC can form even lower dimensions [70, 71], even at finite temperature [72].

2.7. Confinement Induced Resonances

As we saw in see Section 2.5, experimentally, a quasi-one-dimensional Bose gas can be created by confining the particles in a highly elongated cigar-shaped harmonic trap ($\omega_\perp \gg \omega_z$). In this situation, the interaction between bosons can be modeled by the effective two-particle interaction potential [73]

$$V_{\mathrm{int}}(r) = g_{1\mathrm{D}}\delta(r), \tag{2.91}$$

where $g_{1\mathrm{D}} = -2\hbar^2/ma_{1\mathrm{D}}$ is the interaction strength between particles, r is the interparticle distance, and $a_{1\mathrm{D}}$ is the *one-dimensional scattering length*. Due to the effects of the transverse confinement, it is found [73, 74] that

$$a_{1\mathrm{D}} = -\frac{a_\perp^2}{a_{\mathrm{s}}} \left(1 - C\frac{a_{\mathrm{s}}}{a_\perp} \right), \tag{2.92}$$

where a_{s} is the three-dimensional scattering length, $a_\perp = \sqrt{\hbar/m\omega_\perp}$ is the transverse oscillator length, and $C = -\zeta(1/2) \approx 1.46035$. The effective one-dimensional Hamiltonian for N trapped atoms is [75]

$$\hat{\boldsymbol{H}}_{\mathrm{cigar}} = \hat{\boldsymbol{H}}_{\mathrm{LL}} + \sum_{i=1}^{N} \frac{m\omega_z^2 z_i^2}{2}, \tag{2.93}$$

where $\hat{\boldsymbol{H}}_{\mathrm{LL}}$ is the 1D Lieb-Liniger Bose gas Hamiltonian [24]:

$$\hat{\boldsymbol{H}}_{\mathrm{LL}} = -\frac{\hbar^2}{2m} \sum_{i=1}^{N} \partial_{z_i}^2 + g_{\mathrm{1D}} \sum_{i=1}^{N} \sum_{j=i+1}^{N} \delta(z_i - z_j), \tag{2.94}$$

The additional term in Eq. (2.93) r.h.s. arises from the harmonic trapping in the z direction. Hamiltonian Eq. (2.94) describes a one dimensional Bose gas of particles interacting via a repulsive contact potential (see Section 2.8).

Both Eq. (2.92) and Eq. (2.93) establish a connection between theoretical 1D models and experiments in tightly confining waveguides. A remarkable physical phenomenon appears due to the trapping: the so-called *confinement-induced resonance* (CIR) [73, 74]. To understand this resonance, let us rewrite the interaction strength in the following way:

$$g_{\mathrm{1D}} = \frac{2\hbar a_{\mathrm{s}}}{m a_\perp^2} \frac{1}{1 - C a_{\mathrm{s}}/a_\perp}. \tag{2.95}$$

As we can see, by varying the value of the 3D scattering length a_{s} via a Feshbach resonance (FR), the interaction strength can be adjusted. In the 1D mean-field regime, $a_\perp/a_{\mathrm{s}} \gg 1$ hence $g_{\mathrm{1D}} = 2\hbar a_{\mathrm{s}}/m a_\perp^2 = -2\hbar^2/m a_{\mathrm{1D}}$, as we found in Eq. (2.69). A CIR occurs when the scattering length a_{s} approaches the length of transverse confinement $a_\perp$; when $a_\perp = C a_{\mathrm{s}}$, g_{1D} diverges. By slightly adjusting a_{s} around this critical value (see Ref. [76]), the interactions can go from strongly repulsive ($g_{\mathrm{1D}} \to \infty$) to strongly attractive ($g_{\mathrm{1D}} \to -\infty$). The former case (see Section 2.8) corresponds to the Tonks-Girardeau (TG) regime [19, 23], while the latter represents a new regime: the *super Tonks-Girardeau* gas (STG) [35].

2.8. The Lieb-Liniger Bose Gas

The Lieb-Liniger (LL) model [24] describes a one dimensional Bose gas with N particles interacting via a repulsive contact potential. The Hamiltonian of this system is

$$\hat{\boldsymbol{H}}_{\mathrm{LL}} = -\frac{\hbar^2}{2m} \sum_{i=1}^{N} \partial_{z_i}^2 + g_{\mathrm{1D}} \sum_{i=1}^{N} \sum_{j=i+1}^{N} \delta(z_i - z_j), \tag{2.96}$$

where $g_{1D} = -2\hbar^2/ma_{1D}$ is the strength factor of the interaction in the 1D regime.

The Lieb-Liniger gas is a system that can be solved analytically via a Bethe ansatz [77],

$$\psi(z_1, \ldots, z_N) = \sum_P a(P) \, e^{i \sum_{j=1}^{N} k_j z_j}. \tag{2.97}$$

The wavenumbers $k_1, \ldots, k_N$ form an ordered set, and the summation extends over all the permutations $\{P\}$ of them, where the coefficient $a(P)$ depends on a particular permutation.

In the thermodynamical limit, the ground state of the Bose gas at zero temperature can be expressed as

$$E = \frac{\hbar^2}{2m} N n_1^2 e(\gamma(n_1)), \tag{2.98}$$

where n_1 is the average linear density and

$$\gamma = \frac{m g_{1D}}{\hbar^2 n_1} \tag{2.99}$$

is known as the Lieb-Liniger parameter. The function $e(\gamma(n_1))$ is determined by

$$e(\gamma) = -\frac{\gamma^3}{\lambda^3(\gamma)} \int_{-1}^{+1} g(x; \gamma) x^2 \, dx, \tag{2.100}$$

while the functions $g(x, \gamma)$ and $\lambda(\gamma)$ get determined from the equations

$$g(x; \gamma) - \frac{1}{2\pi} = \frac{\lambda(\gamma)}{\pi} \int_{-1}^{+1} \frac{g(x'; \gamma)}{\lambda^2(\gamma) + (x - x')^2} \, dx' \tag{2.101}$$

and

$$\lambda(\gamma) = \gamma \int_{-1}^{+1} g(x; \gamma) \, dx. \tag{2.102}$$

Equation Eq. (2.101) is a Fredholm integral equation of the second kind (see Appendix A.1).

The function $e(\gamma)$ is a monotonically increasing function of γ, as shown in Fig. 2.1. On the one hand, $e(0) = 0$, which corresponds to noninteracting bosons. On the other hand, $e(\gamma \to \infty) = \pi^2/3$ when the gas enters the Tonks-Girardeau (TG) regime [19, 23] of impenetrable bosons. In the TG regime,
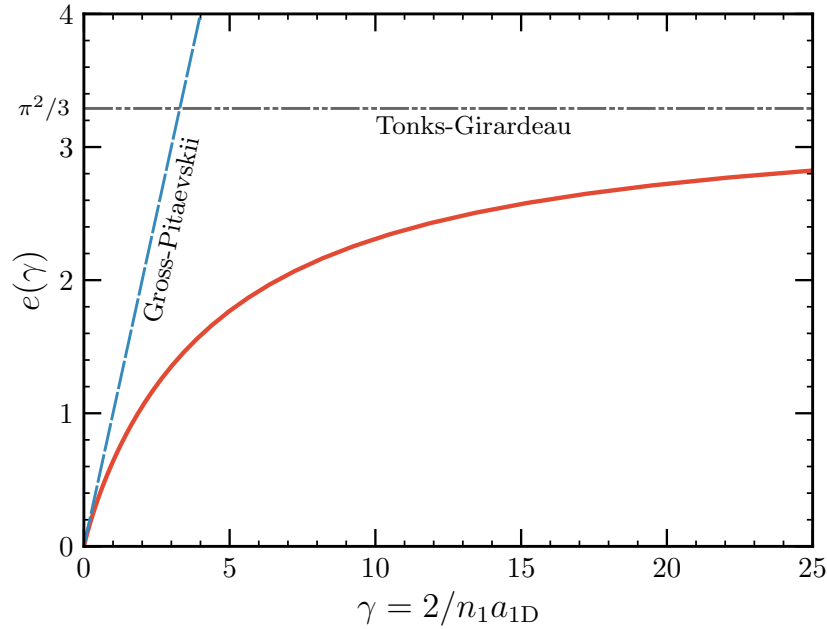
Figure 2.1: Dependence of $e(\gamma)$ as a function of $\gamma = 2/n_1 a_{1D}$ for the Lieb-Liniger theory Eq. (2.100) (solid line). The dashed line shows the small-γ behavior $e(\gamma) \sim \gamma$, which coincides with the 1D GPE prediction. As γ increases, the function tends to the Tonks-Girardeau limit $\pi^2/3$ (dash-dot-dot, horizontal line).

the system manifests the so-called *fermionization* phenomenon [23]. Accordingly, there is a one-to-one correspondence between the wave function of an impenetrable-bosons gas, and the wave function of a noninteracting, spinless-fermions gas. The energy of both systems is

$$E = \frac{\hbar^2 \pi^2 n_1^2}{6m} N. \tag{2.103}$$

For $\gamma \ll 1$, we have $e(\gamma) \sim \gamma$, so the total energy is $E \sim (g_{1D} n_1/2)N$. This result is the same as the one obtained using mean-field theory in 1D, i.e., the Gross-Pitaevskii equation applied to a one-dimensional system in Section 2.5. Hence, $\gamma \ll 1$ corresponds to the mean-field regime.

The LL parameter Eq. (2.99) is related to the one-dimensional scattering length Eq. (2.92) in a cigar-shape trap through

$$\gamma = -\frac{2}{n_1 a_{1D}}. \tag{2.104}$$

25

We saw in Section 2.5 that the 1D mean-field regime coincides with the high-density limit $n_1|a_{1D}| \gg 1$; this agrees which the mean-field condition $\gamma \ll 1$ for the LL model. The opposite limit $\gamma \to \infty$, according to Eq. (2.104), is equivalent to $n_1|a_{1D}| \ll 1$. Consequently, the Tonks-Girardeau regime coincides with the low-density limit.

2.9. Low-Energy Universal Description

The Lieb-Liniger gas is a remarkable system because one can solve the many-body problem for the ground state in an exact way; hence, it is an *exactly solvable model* or *integrable model*. The Tonks-Girardeau Bose gas of hard-core bosons [23] is another example of such models; it corresponds to the limit $g_{1D} \to \infty$ in Eq. (2.96) for the LL model, i.e., bosons with infinitely strong repulsive interactions. Additional examples of exactly solvable models include the Calogero model [25], and the t-V model: a particular case of the Bose-Hubbard model with an on-site interaction $U \to \infty$ [78].

Finding the exact solution of many-body, interacting systems is a tough task. At low temperatures, an alternative way to investigate such systems, even those nonintegrable, is using effective models that describe physical properties starting from the system's low-energy excitations. This approach is the spirit of Landau's Fermi liquid theory [79] for a degenerate, translationally-invariant, interacting, 3D isotropic fermionic gas. It is a phenomenological theory that predicts the behavior of the physical properties from some parameters that can be determined experimentally. The most remarkable result of Fermi liquid theory is that the properties of the interacting system remain mostly the same as the ideal system, even when the interactions between the particles are not small. However, the elementary constituents of the system are not individual electrons anymore, but *quasiparticles* formed by electrons *dressed* by density fluctuations around them, which behave like almost as free fermionic particles with a different effective mass. The microscopic derivation of the theory was obtained by J. M. Luttinger and P. Nozières in 1962 [80, 81].

How do one-dimensional systems compare to the 3D ones? In 3D systems, nearly free quasiparticles can exist. In 1D, particles can only move along one direction. If one of them tries to move, it has to push its neighbors. Therefore, individual motion is not possible, and excitations become necessarily collective. This collectivization invalidates the Landau Fermi liquid theory applicability for 1D systems. A useful low-energy description for 1D gases, whether bosonic or fermionic, must take into account the collective nature of the excitations. Such a formalism, applicable to a broad class of 1D systems with conducting or fluid

properties, is known as *Luttinger liquid theory* [20, 82, 83]. Frederick D. M. Haldane noticed two especially relevant characteristic properties of *Luttinger liquids*. First, their density-wave, collective elementary excitations spectrum has a linear dispersion at long wavelengths that defines a sound velocity. Second, at zero temperature, the correlation functions show a power-law decay. Haldane also derived [84] the low-energy properties of one-dimensional quantum fluids from an *Effective Harmonic-Fluid Approach* independent of statistics, and showed that the collective excitations of such fluids are noninteracting bosonic particles, i.e., phonons.

Let us consider a system of N bosons with length L, average density $n_1 = N/L$, and periodic boundary conditions. We assume bosons interact via a two-body potential. The Hamiltonian of the system is

$$
\hat{\boldsymbol{H}} = \frac{\hbar^2}{2m} \int dz \left(\partial_z \hat{\boldsymbol{\Psi}}^\dagger(z) \right) \left(\partial_z \hat{\boldsymbol{\Psi}}(z) \right)
$$
$$
+ \frac{1}{2} \int dz\, dz'\, \hat{\boldsymbol{\Psi}}^\dagger(z) \hat{\boldsymbol{\Psi}}^\dagger(z') V_{\text{int}}(z' - z) \hat{\boldsymbol{\Psi}}(z') \hat{\boldsymbol{\Psi}}(z), \quad (2.105)
$$

where the quantum field operator $\hat{\boldsymbol{\Psi}}(z)$ fulfills commutation relations

$$
\left[\hat{\boldsymbol{\Psi}}(z), \hat{\boldsymbol{\Psi}}^\dagger(z') \right] = \delta(z - z'), \tag{2.106a}
$$

$$
\left[\hat{\boldsymbol{\Psi}}^\dagger(z), \hat{\boldsymbol{\Psi}}^\dagger(z') \right] = 0, \tag{2.106b}
$$

$$
\left[\hat{\boldsymbol{\Psi}}(z), \hat{\boldsymbol{\Psi}}(z') \right] = 0, \tag{2.106c}
$$

and $\hat{\boldsymbol{\Psi}}^\dagger(z + L) = \hat{\boldsymbol{\Psi}}^\dagger(z)$.

In the Luttinger liquid theory [84], the collective character of the excitations motivates a field-theoretic approach in terms of collective fields. For bosons, these are the density operator $\hat{\boldsymbol{n}}(z)$ and the phase operator $\hat{\boldsymbol{\theta}}(z)$. The bosonic field operator $\hat{\boldsymbol{\Psi}}^\dagger(z)$ is written in polar form:

$$
\hat{\boldsymbol{\Psi}}^\dagger(z) = [\hat{\boldsymbol{n}}(z)]^{1/2} e^{-i\hat{\boldsymbol{\theta}}(z)}. \tag{2.107}
$$

Since this field operator and its adjoint fulfill bosonic commutation relations Eq. (2.14), there are similar relations for density and phase operators [85], in particular:

$$
\left[\hat{\boldsymbol{n}}(z), e^{-i\hat{\boldsymbol{\theta}}(z')} \right] = \delta(z - z') e^{-i\hat{\boldsymbol{\theta}}(z')}, \tag{2.108}
$$

which is consistent with the relation [78]

$$
\left[\hat{\boldsymbol{n}}(z), \hat{\boldsymbol{\theta}}(z') \right] = i\delta(z - z'). \tag{2.109}
$$

27

This relation expresses the well-known fact that in a superfluid or a BEC, the density and the phase are canonically conjugate fields.

To proceed further, let us consider the expression for the density field operator of a many-body system with N particles,

$$\hat{\boldsymbol{n}}(z) = \sum_{j=1}^{N} \delta(z - z_j), \tag{2.110}$$

where z_j is the position of the j-th particle. The density operator can be written more conveniently if we introduce a labeling field $\hat{\phi}_l(z)$. This field is a smooth, monotonically increasing continuous function of the position such that $\hat{\phi}_l(z_j) = 2\pi j$, i.e., it increases by 2π each time z passes the location of a particle. Its boundary conditions are $\hat{\phi}_l(z + L) = \hat{\phi}_l(z) + 2\pi N$. Now, let us consider that the particles are uniformly distributed on a straight line. Since the system has an average density n_1, the interparticle distance is n_1^{-1}, and the position of the j-th particle is $z_j = j n_1^{-1}$. Then, the *perfect* labeling field of the uniform system is $\hat{\phi}_l(z) = 2\pi n_1 z$. One can define a field $\hat{\phi}(z)$ relative to the perfect one as $\hat{\phi}_l(z) = 2\pi n_1 z - 2\hat{\phi}(z)$, by which the density operator can be written as

$$\hat{\boldsymbol{n}}(z) = \left(n_1 - \frac{1}{\pi}\partial_z\hat{\phi}(z)\right) \sum_{p=-\infty}^{\infty} e^{i2p(\pi n_1 z - \hat{\phi}(z))}. \tag{2.111}$$

This expression is known as the harmonic representation of the density operator. Equation (2.111) leads to the corresponding low-energy, harmonic representation of the bosonic quantum field operator Eq. (2.107) [84, 85]:

$$\hat{\boldsymbol{\Psi}}^{\dagger}(z) \simeq \left(n_1 - \frac{1}{\pi}\partial_z\hat{\phi}(z)\right)^{1/2} \left[\sum_{p=-\infty}^{\infty} e^{i2p(\pi n_1 z - \hat{\phi}(z))}\right] e^{-i\hat{\theta}(z)}. \tag{2.112}$$

Physically, for low-energy states, it is expected that $\hat{\theta}(z)$ and $\hat{\phi}(z)$ should vary slowly over a distance of order n_1^{-1}. From Eq. (2.109) and Eq. (2.111), it follows that

$$\left[\hat{\boldsymbol{\theta}}(z), \frac{1}{\pi}\partial_{z'}\hat{\phi}(z')\right] = i\delta(z - z'). \tag{2.113}$$

This result proves that $\hat{\theta}(z)$ and $\partial_z\hat{\phi}(z)/\pi$ are canonically conjugate fields.

The harmonic form of the field operator Eq. (2.111) results in a low-energy representation (keeping only the leading terms) of the Hamiltonian:

$$\hat{\boldsymbol{H}} = \frac{\hbar}{2\pi} \int dz \left[c_s K \left(\partial_z\hat{\boldsymbol{\theta}}(z)\right)^2 + \frac{c_s}{K} \left(\partial_z\hat{\phi}(z)\right)\right]. \tag{2.114}$$

Remarkably, the unknown parameters $v_J = c_{\mathrm{s}} K$ and $v_N = c_{\mathrm{s}}/K$ characterize all the low-energy properties of the system. They fulfill $v_J v_N = c_{\mathrm{s}}^2$, where c_{s} is the velocity of the density fluctuations, i.e., the sound velocity in the fluid. The parameter K, commonly referred to as the *Luttinger parameter*, controls the decay rate of the correlation functions at long distances [78, 84, 85]. Parameters v_J and v_N are nonuniversal since they depend on the microscopic characteristics of the system. They must be calculated, whether analytically or numerically, for the particular microscopic model under study. Among the available methods for such purpose are the Bethe ansatz, exact diagonalization, Quantum Monte Carlo (QMC) methods, and Density Matrix Renormalization Group (DMRG), to name a few. Once obtained, all the properties of the system are determined. Fortunately, there are well-established relations for both parameters with thermodynamic properties, which we describe in the following lines.

The *density stiffness* $v_N = c_{\mathrm{s}}/K$ is related to the zero-temperature macroscopic adiabatic compressibility κ by [84, 85]

$$\kappa^{-1} = \hbar \pi v_N n_1^2 = \hbar \pi n_1^2 \frac{c_{\mathrm{s}}}{K}, \tag{2.115}$$

where

$$\kappa^{-1} = n_1^2 L \left(\frac{\partial^2 E_0(N)}{\partial N^2} \right). \tag{2.116}$$

Here, $E_0(N)$ is the ground-state energy of the system with N particles. Next, we obtain

$$v_N = \frac{L}{\pi \hbar} \left(\frac{\partial^2 E_0(N)}{\partial N^2} \right). \tag{2.117}$$

The *phase stiffness* $v_J = c_{\mathrm{s}} K$ is related to the response of the system (at zero temperature) to a *twist* in the boundary conditions of the field operator:

$$\hat{\boldsymbol{\Psi}}^\dagger(z + L) = e^{-i\alpha} \hat{\boldsymbol{\Psi}}^\dagger(z). \tag{2.118}$$

We say that the field operator fulfills *twisted boundary conditions*, being α the twist angle. The introduction of this twist shifts both ground state energy and momentum regarding their values for $\alpha = 0$. In particular, the ground-state energy shift and the phase stiffness v_J become related by [85, 86]

$$v_J = \frac{\pi L}{\hbar} \left(\frac{\partial^2 E_0(\alpha)}{\partial \alpha^2} \right)_{\alpha=0}. \tag{2.119}$$

Looking at Eq. (2.117) and Eq. (2.119), we see that v_N and v_J relate the response of the system to a change in the particle number and a phase twist, respectively. Physically, in the presence of a twist in the boundary conditions, the system responds by drifting as a whole with a constant velocity, and the kinetic energy of the superfluid fraction $n_{1(\text{sf})}$ should be equal to the change of the ground-state energy. Then, one can relate the phase stiffness v_J with the superfluid fraction by [86]

$$v_J = \frac{\hbar \pi n_{1(\text{sf})}}{m}. \tag{2.120}$$

Although it is useful to calculate both c_{s} and K together with Eq. (2.117), relation Eq. (2.120) should be interpreted with care [78, 87].

For Galilean invariant systems, such as the Lieb-Liniger model Eq. (2.96), v_J is independent of interactions. Furthermore,

$$v_J = v_{\text{F}} = \frac{\hbar k_{\text{F}}}{m}, \tag{2.121}$$

where v_{F} and k_{F} are the Fermi velocity and Fermi momentum, respectively. For instance, for a spinless Bose gas $k_{\text{F}} = \pi n_1$, then Eq. (2.117) yields

$$\kappa = \frac{K^2}{v_{\text{F}} \hbar \pi n_1^2} = \frac{m K^2}{\hbar^2 \pi^2 n_1^3}. \tag{2.122}$$

This relation shows that the system becomes more compressible if K increases. For a noninteracting Bose gas, it is a well-known result that $\kappa \to \infty$, then $K \to \infty$. Repulsive interactions reduce compressibility, as showed in Section 2.4 for the weakly-interacting Bose gas. As an example, let us consider the Lieb-Liniger Bose gas (see Section 2.8). For infinitely strong interactions $g_{1D} \to \infty$, it becomes the Tonks-Girardeau gas whose energy is given by Eq. (2.103). Using Eq. (2.122), it follows immediately that $K = 1$. For finite interactions, the LL Bose gas energy is a monotonically increasing function of g_{1D}. Also, it approaches asymptotically to Eq. (2.103) as $g_{1D} \to \infty$. According to Eq. (2.116), the LL Bose gas compressibility is a monotonically decreasing function of g_{1D}. Therefore, $K \geq 1$. When $g_{1D} \sim 0$, the LL energy is well approximated by the 1D, weakly-Interacting Bose gas energy Eq. (2.70), and the compressibility, as the Luttinger parameter, diverge as $g_{1D} \to 0$.

3

Weakly-Interacting Bose Gas in Multi-Rods

In this chapter, we report the analysis of the physical properties of a 1D, weakly-interacting Bose gas constrained in a multi-rod, periodic structure. The results include an analytical treatment of the GPE, as well as numerical results obtained for the ground state properties. Also, we give a brief review of experimental methods used to manipulate quantum gases.

3.1. Manipulation of Quantum Gases

3.1.1. Magnetic Traps

Typically, atomic quantum gases are confined by inhomogeneous magnetic fields. By exploiting the Zeeman effect to subject the atoms to the action of a spatially varying potential, experimental setups can trap atoms around a finite region where the field has a minimum. A simple configuration is the 3D quadrupole field since the field vanishes at its center; this point acts as the center of the trap for the atoms. Despite its simplicity, pure quadrupole fields are not efficient to trap BECs due to *Majorana losses* [44, 45] that occur around the minimum of the field. With the aid of extra fields, the field at the center of the quadrupole trap is non-zero anymore, avoiding Majorana losses. For instance, in a time-averaged orbiting potential trap (TOP), this is achieved with a rotating uniform field superimposed to the quadrupole one; this was the type of trap used by Anderson et al. [1] to produce a BEC in 1995. A different approach is followed by the Ioffe-Pritchard trap, which uses two sets of coils to create the fields that confine the atoms harmonically in the three spatial directions. An extra pair of coils produces a static *bias* field that shifts the minimum of the

potential without disturbing the harmonic fields. The intensity of the fields can be controlled to produce, for instance, a "cigar-shaped" trap, as well as almost spherical traps. Magnetic traps can be combined with laser beams in an experimental setup to form a magneto-optical trap (MOT) that, besides trapping atoms, cools them (Doppler cooling).

3.1.2. Optical Lattices

The interaction between an atom and an oscillating electric field $\boldsymbol{\mathcal{E}}(\boldsymbol{r}, t)$ induces a dipole moment $\boldsymbol{d}$ in the atom. This interaction creates an energy shift on the ground state of the atom which behaves as an effective trapping potential [44] $V_{\text{dip}}(\boldsymbol{r}) = -\frac{1}{2}\alpha(\omega)|\boldsymbol{\mathcal{E}}(\boldsymbol{r})|^2$, where $\alpha(\omega)$ is the real part of the atomic polarizability, ω is the angular frequency of the electric field, and $|\boldsymbol{\mathcal{E}}(\boldsymbol{r})|^2$ is the intensity of the laser light proportional to the squared magnitude of the electric field.

The overlapping of two counter-propagating laser beams with the same wavelength λ_{OL} in opposite directions generates a standing wave with a period $\lambda_{\text{OL}}/2$ where the atoms can be trapped. The potential of this *optical lattice* has a magnitude

$$V_{\text{OL}}(z) = sE_{\text{R}}\sin^2(k_{\text{OL}}z), \tag{3.1}$$

where $k_{\text{OL}} = 2\pi/\lambda_{\text{OL}}$ is the wavenumber of the laser beams. The constant E_{R} is known as the *recoil energy* of the system,

$$E_{\text{R}} \equiv \frac{\hbar^2 k_{\text{OL}}^2}{2m}, \tag{3.2}$$

and is the natural energy scale in optical traps experiments. The parameter s measures the lattice depth. Geometrically, this 1D lattice creates a periodic array of 2D regions where the atoms get confined. Two potentials like Eq. (3.1) in orthogonal directions create an array of potential 1D tubes, while three orthogonal standing waves create a 3D cubic lattice [10]. Harmonic traps can be superimposed to the optical potentials to create more complex structures.

Optical lattices are versatile tools because of the high degree of tunability of their features, as well as the capability to adjust the magnitude of the interactions between particles via Feshbach resonances [88]. For example, the angle of interference between beams can be adjusted to create complex optical structures, like Kagomé lattices [89, 90]. Also, they have been used to observe the superfluid to Mott insulator transition in three and one-dimensional Bose gases [91, 92], as well as the experimental realization of the Tonks-Girardeau

Bose gas [21, 22]. On the other hand, the connection between high-T_C super-conductivity [93–95] and the Fermi-Hubbard model opens an opportunity to study the former using ultracold fermionic gases. Previous examples (among many others) show why optical lattices are considered an ideal platform for simulations of quantum many-body problems [10–12].

3.1.3. Magnetic Micro-Traps

The magnetic traps described in the previous section use macroscopic coils to generate magnetic fields. An alternative approach is building *magnetic micro-traps*, i.e., a set of microscopic conducting structures where electric currents flow, creating magnetic fields used to confine cold atoms very close to the surfaces of the conductors. The micro-trap concept can be enhanced by using the mature technology of semiconductors and the advances in cold atoms research. The result is a solid-state device where a BEC can be stored and manipulated. Also, micro-traps can have almost-arbitrary shapes limited only by the structure of the conductors. The final result is a compact, portable, and flexible setup commonly known as *atom chip*. First atom chips were realized in 1999 [5–7], and the first Bose-Einstein condensates on this kind of devices were realized only a couple of years later [8, 96]. Initially, only neutral bosonic atoms where used; later, the universe of neutral particles expanded to include fermionic particles, molecules, and Rydberg atoms. Atom chips have also been used in the study of degenerate 1D Bose gases [14–18]. For a more in-depth review of this subject, see Refs. [97, 98].

3.2. Ideal Bose Gas in Multi-Rods

Let us consider a 1D ideal Bose gas constrained within a periodic lattice composed by multiple rods. These rods can be seen as permeable barriers of width b separated by a distance a one from each other, distributed along the z direction. In order to model the rods, we use a Kronig-Penny potential [99] in the z direction composed of potential barriers of width b and separation a. The period of the potential is $l \equiv a + b$. The height of the potential barriers V_0, whose magnitude is inversely proportional to the barrier permeability, is a measure of how probable the tunneling of the bosons through the rods is.

Since we are considering noninteracting particles, the problem reduces to solve the one-particle Schrödinger equation

$$\hat{\boldsymbol{H}}_0 \Psi(z) = \varepsilon \Psi(z), \tag{3.3}$$
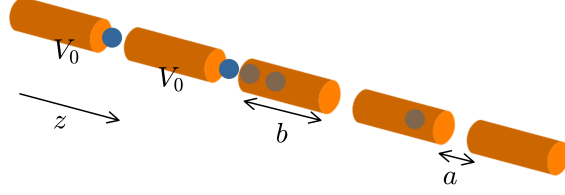
33

Figure 3.1: Schema of a 1D Bose gas in multi-rods.

where the one-particle Hamiltonian for the z coordinate $\hat{\boldsymbol{H}}_0$ is defined as

$$\hat{\boldsymbol{H}}_0 = -\frac{\hbar^2}{2m}\frac{\partial^2}{\partial z^2} + V_{\mathrm{KP}}(z). \tag{3.4}$$

with m the particle mass and $V_{\mathrm{KP}}(z)$ the Krong-Penney potential,

$$V_{\mathrm{KP}}(z) = V_0 \sum_{j=-\infty}^{\infty} \Big(\Theta(z - jl + a) - \Theta(z - (j+1)l) \Big), \tag{3.5}$$

where $\Theta(z)$ is the Heaviside step function (see Fig. 3.2). Since the KP potential is periodic, the solutions of the differential equation (3.3) are Bloch states,

$$\Psi(z) \equiv e^{ikz}\phi_k(z), \tag{3.6}$$

with $\hbar k$ being the quasi-momentum of the particles and $\phi_k(z)$ a periodic function with the same period of the potential, i.e.,

$$\phi_k(z + l) = \phi_k(z). \tag{3.7}$$

If we substitute Eq. (3.7) in (3.3), we arrive at a similar equation for $\phi_k(z)$,

$$\hat{\boldsymbol{H}}_0^{(k)}\phi_k(z) = \varepsilon_k\phi_k(z), \tag{3.8}$$

where the energy ε_k, which depends on k, is the eigenvalue of the one-particle "shifted" Hamiltonian

$$\hat{\boldsymbol{H}}_0^{(k)} = \frac{\hbar^2}{2m}(-i\partial_z + k)^2 + V_{\mathrm{KP}}(z), \tag{3.9}$$

where we use the notation $\partial_z \equiv \partial/\partial_z$.

In order to solve Eq. (3.8), we impose suitable boundary conditions: continuity of the wave function and its derivative at the edges of the barriers, as
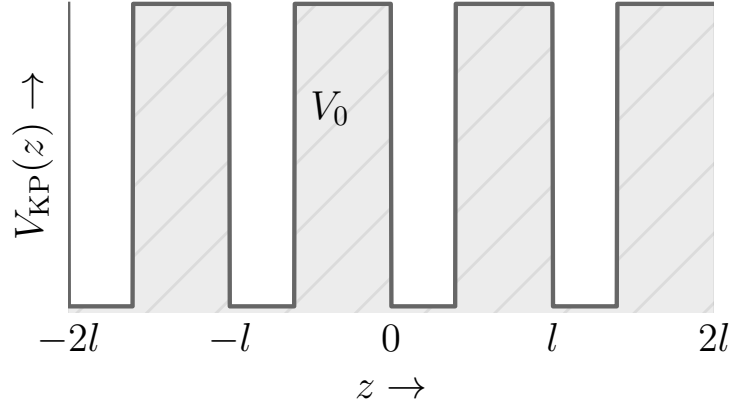
Figure 3.2: Kronig-Penney potential schematic.

well as the periodicity condition. Then, the energy ε_k is given by the implicit relation [99],

$$\frac{\kappa^2 - \alpha^2}{2\alpha\kappa} \sinh(\kappa b) \sin(\alpha a) + \cosh(\kappa b) \cos(\alpha a) = \cos[k(a+b)], \quad (3.10)$$

where $\hbar\kappa = \sqrt{2m(V_0 - \varepsilon_k)}$ y $\hbar\alpha = \sqrt{2m\varepsilon_k}$. Equation (3.10) is the well-known Krong-Penney dispersion relation for the energy. In general, it can not be solved analytically, so we have to resort to numerical techniques to estimate the values of the energy for a given quasi-momentum k. The energy spectrum of a particle subject to a nonzero KP potential is not continuous. We can understand this directly from Eq. (3.10): only the right-hand side depends on the quasimomentum k, while the left-hand side depends only on the energy ε_k. For a given value of k, the right-hand side of (3.10) is a number in the interval $[-1, 1]$; therefore, only the values of ε_k that make the left-hand side to fulfill this constraint are accessible. There are values of the energy that never satisfy Eq. (3.10). The final result is that for each value of k, Eq. (3.10) defines a complete family of eigenstates $\phi_{k,j}(z)$ with their corresponding energies $\varepsilon_{k,j}$, $j = 1, 2, 3, \ldots$. Then, the energy spectrum of the particles is formed by intervals of allowed energies, which we recognize as the energy bands of the system (labeled by the index j), separated by regions of inaccessible energies, known as forbidden bands. The shape of the energy bands is fixed by the potential parameters: magnitude V_0, a, and b.

The energy as a function of the potential magnitude for $b = a$ is shown in Fig. 3.3a. The colored regions represent the allowed energies. We can see how the energy spectrum starts as a continuum, i.e., there are no forbidden bands
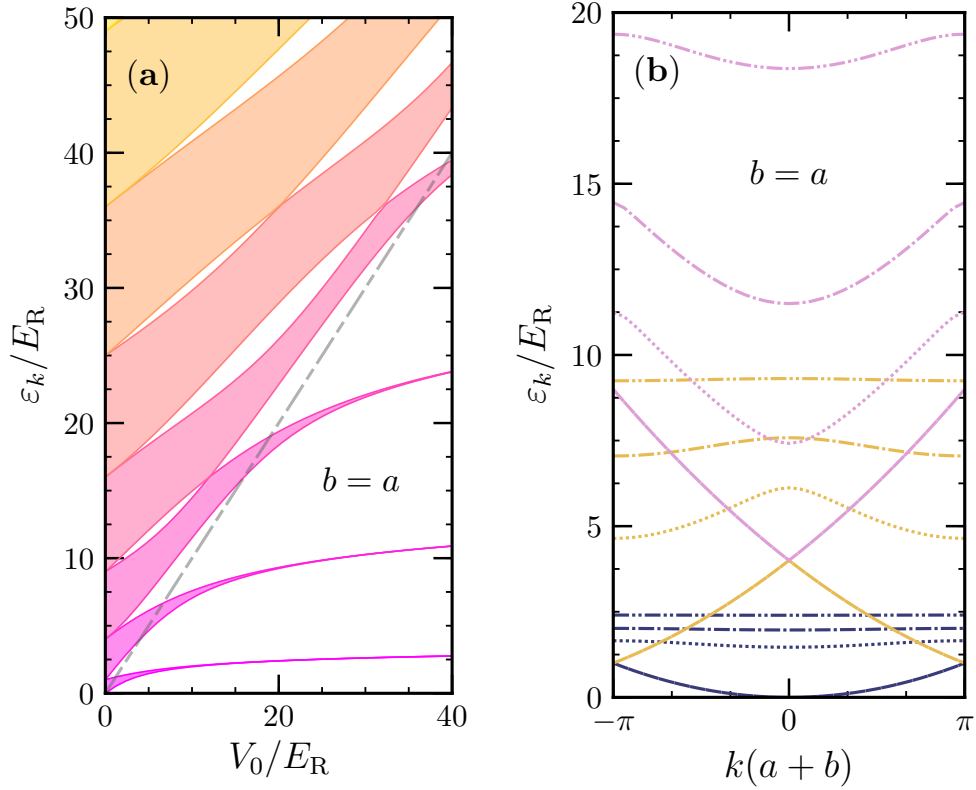
Figure 3.3: (Color online) Energy spectrum (in units of $E_\mathrm{R} = \hbar^2\pi^2/2ml^2$, see Section 3.4) for a square lattice $b = a$. **(a)**: as a function of the potential magnitude V_0. The filled regions indicate the allowed energy bands, while the blank regions indicate the forbidden bands. The dashed line indicates $\varepsilon_k = V_0$. **(b)**: as a function of the quasimomentum k in the first Brillouin zone. The solid line shows the first three energy bands of the free, IBG. Dotted, dash-dot, and dash-dot-dot lines correspond to $V_0 = 5, 10$ and 20 times E_R, respectively.

(white regions) when V_0 is zero. As V_0 increases, the forbidden regions appear, and the continuum spectrum becomes a succession of allowed bands separated by forbidden bands. When the potential magnitude becomes large enough, the bands tend to collapse as energy levels very close to the limiting value

$$\varepsilon^{(j)} = (1 + r)^2 j^2 \left(\frac{\hbar^2 \pi^2}{2ml^2} \right), \tag{3.11}$$

where r is *lattice ratio* of the potential,

$$r \equiv \frac{b}{a}, \tag{3.12}$$

and j is the band index. In Fig. 3.3b, we show the first three bands of the spectrum as a function of the quasimomentum k in the first Brillouin zone (BZ). We can see how the bands become more narrow as the potential height V_0 increases, in agreement with results shown in Fig. 3.3a.

3.3. Bloch States of the Gross-Pitaevskii Equation

In Section 2.5, we have shown that the GPE is the primary tool to study the properties of the 1D Bose gas in the weakly-interacting regime at temperatures very close to absolute zero. We now want to study the properties of the interacting Bose gas in multi-rods, particularly the stationary states of the GPE. Therefore, we have to solve Eq. (2.80) with an external KP potential, i.e., with the Hamiltonian

$$\hat{\boldsymbol{H}}_{\mathrm{GP_{1D}}} = -\frac{\hbar^2}{2m}\frac{\partial^2}{\partial z^2} + V_{\mathrm{KP}}(z) + g_{\mathrm{1D}}\left|\Phi_{\mathrm{1D}}(z)\right|^2 \tag{3.13}$$

subject to the normalization condition (2.82). Despite being a nonlinear equation, Eq. (2.80) with Hamiltonian Eq. (3.13) has solutions in the form of Bloch states,

$$\Phi_{\mathrm{1D}}(z) = e^{ikz}\phi_k(z), \tag{3.14}$$

where $\phi_k(z)$ is a periodic function with the same period than the KP potential,

$$\phi_k(z+l) = \phi_k(z), \tag{3.15}$$

and k is the quasimomentum of the bosons. Direct substitution of (3.14) in Eqs. (3.13) and (2.80) lead us to the stationary GPE equation for $\phi_k(z)$,

$$\hat{\boldsymbol{H}}_{\mathrm{GP_{1D}}}^{(k)}\phi_k(z) = \mu_{\mathrm{1D}}^{(k)}\phi_k(z), \tag{3.16}$$

with

$$\hat{\boldsymbol{H}}_{\mathrm{GP_{1D}}}^{(k)}(z) = \frac{\hbar^2}{2m}(-i\partial_z + k)^2 + V_{\mathrm{KP}}(z) + g_{\mathrm{1D}}\left|\phi_k(z)\right|^2, \tag{3.17}$$

where we have used that for Bloch states $|\Phi_{\mathrm{1D}}(z)|^2 = |\phi_k(z)|^2$. Since the multi-rod system is periodic, and the unit cell repeats over and over, the total number

of particles is infinite. We redefine the normalization condition (2.77) in a way that it makes sense,

$$\int_0^l |\phi_k(z)|^2 \ dz = N_{\text{cell}}, \tag{3.18}$$

where N_{cell} is the average number of bosons in the condensate over a length equal to the potential period such that the average linear density of the system becomes

$$n_1 \equiv \frac{N_{\text{cell}}}{l}. \tag{3.19}$$

The energy of our system, analogously to Eq. (2.76), is

$$E[\Phi_{\text{1D}}] = \frac{\hbar^2}{2m} \int_0^l \left(|(-i\partial_z + k)\phi_k(z)|^2 \right) \ dz +$$
$$\int_0^l \left(V_{\text{ext}}(z) |\phi_k(z)|^2 + \frac{g_{\text{1D}}}{2} |\phi_k(z)|^4 \right) \ dz. \tag{3.20}$$

To solve the GPE with the corresponding boundary conditions, we express the function $\phi_k(z)$ in complex form,

$$\phi_k(z) = \sqrt{n_1(z)}e^{iS(z)}, \tag{3.21}$$

where the function $S(z)$ represents the phase and $n_1(z) \equiv |\phi_k(z)|^2 = |\Phi_{\text{1D}}(z)|^2$ is the particle density profile as a function of z.

Let be $R(z) = \sqrt{n_1(z)}$; we substitute Eq. (3.21) in Eq. (3.16) and separate the real and imaginary parts of the resulting expression. The real part is

$$-\frac{\hbar^2}{2m} \left(\partial_z^2 R(z) - R(z) \left(\partial_z S(z) \right)^2 \right) +$$
$$\left(\frac{\hbar^2 k}{m} \partial_z S(z) + \frac{\hbar^2 k^2}{2m} + V_{\text{KP}}(z) \right) R(z) + g_{\text{1D}} R(z)^3 = \mu_{\text{1D}}^{(k)} R(z), \tag{3.22}$$

while the imaginary part becomes

$$-\frac{\hbar^2}{2m} \left[2 \left(\partial_z R(z) \right) \left(\partial_z S(z) \right) + R(z) \partial_z^2 S(z) \right] - \frac{\hbar^2 k}{m} \partial_z R(z) = 0. \tag{3.23}$$

Equation (3.23) can be solved by separation of variables. First, we collect common terms, arriving at

$$R(z) \partial_z^2 S(z) = -2 \left(\partial_z R(z) \right) \left(k + \partial_z S(z) \right). \tag{3.24}$$

Under the change of variable $u(z) = \partial_z S(z)$, we can apply the separation of variables. The resulting differential equation for the phase is

$$\partial_z S(z) = -k + \frac{\alpha}{n_1(z)}, \tag{3.25}$$

where α is a constant of integration whose value is fixed by the boundary conditions of the problem. Hence, the phase becomes

$$S(z) = S_0 - kz + \int_0^z \frac{\alpha}{n_1(z')} \, dz', \tag{3.26}$$

where $S_0 = S(z = 0)$ is a constant of integration. Despite its simplicity, Eq. (3.26) is coupled with (3.22), as it depends on $n_1(z) = R(z)^2$. We substitute Eq. (3.25) in (3.22); after rearranging terms, we obtain a nonlinear differential equation for $R(z)$:

$$-\frac{\partial^2 R}{\partial z^2} + \frac{\alpha^2}{R(z)^3} + \frac{2m}{\hbar^2}\left(V_{\text{KP}}(z) - \mu_{1\text{D}}^{(k)}\right) R(z) + \frac{2mg_{1\text{D}}}{\hbar^2} R(z)^3 = 0. \tag{3.27}$$

In order to proceed further, we have to take into account the concrete functional form of $V_{\text{KP}}(z)$, following the work of [47, 100]. The KP potential is a piecewise function with two constant values: V_0 in the region occupied by the barriers, and zero in the wells region. First, we focus on the barriers region where $V_{\text{KP}}(z) = V_0$. If we multiply Eq. (3.27) by $\partial_z R(z)$ and integrate, after some algebraic steps, we arrive at

$$-\frac{1}{2}\left(\frac{\partial R}{\partial z}\right)^2 - \frac{\alpha^2}{2R(z)^2} + \frac{m}{\hbar^2}(V_0 - \mu_{1\text{D}})R(z)^2 + \frac{mg_{1\text{D}}}{2\hbar^2}R(z)^4 = \sigma, \tag{3.28}$$

with σ being a constant of integration. Finally, multiplying by $-8R(z)^2$ and rearranging terms, we arrive at

$$\left(\frac{dR^2}{dz}\right)^2 = 4\left[\frac{mg_{1\text{D}}}{\hbar^2}R(z)^6 + \frac{2m}{\hbar^2}(V_0 - \mu_{1\text{D}})R(z)^4 - 2\sigma R(z)^2 - \alpha^2\right]. \tag{3.29}$$

Here we have changed the partial derivatives to total derivatives as the equation only depends on z. Equation (3.29) is equivalent to the differential equation for the density

$$\left(\frac{dn_1}{dz}\right)^2 = \frac{4mg_{1\text{D}}}{\hbar^2}n_1^3(z) + \frac{8m}{\hbar^2}(V_0 - \mu_{1\text{D}})n_1^2(z) - 8\sigma n_1(z) - 4\alpha^2, \tag{3.30}$$

39

since $n_1(z) = R(z)^2$.

Equations (3.26) and (3.30) are equivalent to Eq. (3.16) for $\phi_k(z)$. They determine the complete wave function of the ground state of the system that is a Bloch state with quasimomentum k. Indeed, we have to supplement these equations with the adequate boundary conditions in order to obtain the concrete density profile, the energy of the system, and the chemical potential, among other properties. Also, we should remember that we have arrived at this equation by considering that we are in the region occupied by the barriers, where $V_{\text{KP}}(z) = V_0$. In the wells region where the potential is zero, the corresponding ODE for the density has the same structure as Eq. (3.30), but we have to set $V_0 = 0$, so only the quadratic term in $n_1(z)$ changes.

Despite the nonlinear nature of Eq. (3.30), it has an analytical solution for $n_1(z)$ given in terms of the Jacobi Elliptic functions [101],

$$n_1(z) = n_{1(\text{off})} + 4m_{\text{j}}\lambda^2 \operatorname{sn}^2\left(\sqrt{\frac{4m_{\text{j}}g_{1\text{D}}}{\hbar^2}}\lambda(z - z_{\text{off}})\,|m_{\text{j}}\right), \tag{3.31}$$

where $\operatorname{sn}(u|m_{\text{j}})$ is the Jacobi elliptic sine function of argument u in canonical form. The factor m_{j} is a real number known as the elliptic modulus; the factors $n_{1(\text{off})}$ and z_{off} are constant offsets on the value of the density and the position, respectively, while λ is a parameter that fixes the amplitude of the spatial density variations.

Before proceeding further, we should note that constant α has an important physical meaning. Following the definition of the current density for a stationary state,

$$j(z) = -\frac{i\hbar}{2m}\left(\Phi_{1\text{D}}^*(z)\partial_z\Phi_{1\text{D}}(z) - \Phi_{1\text{D}}(z)\partial_z\Phi_{1\text{D}}^*(z)\right), \tag{3.32}$$

we can show that, for a Bloch state Eq. (3.14), the current density is

$$j(z) = \frac{\hbar}{m}n_1(z)\left[k + \partial_z S(z)\right] = \frac{\hbar\alpha}{m}. \tag{3.33}$$

Then, the constant α is proportional to the current density corresponding to the order parameter.

3.3.1. Boundary Conditions

The expression for the density Eq. (3.31) is valid only for a constant potential. Because of the piecewise nature of the KP potential, we will have two

solutions for $\phi_k(z)$: one within the wells (w) region and another within the barriers (b) region. Then,

$$\phi_k(z) = \begin{cases} \phi_k^{\mathrm{b}}(z) = \sqrt{n_1^{\mathrm{b}}(z)}e^{iS^{\mathrm{b}}(z)}, & V_{\mathrm{KP}}(z) = V_0 \\ \phi_k^{\mathrm{w}}(z) = \sqrt{n_1^{\mathrm{w}}(z)}e^{iS^{\mathrm{w}}(z)}, & V_{\mathrm{KP}}(z) = 0 \end{cases}. \tag{3.34}$$

These functions must match smoothly at the interface of each potential barrier. Also, they have to be periodic with the same period as the potential. It follows, from Eq. (3.34), that each region has a set of parameters $n_{1(\mathrm{off})}$, λ, m_{j}, and z_{off} that fix the density profile (3.31). The relationship between these parameters will depend on the (suitable) boundary conditions imposed on the system. We can exploit the periodicity of the multi-rod system and $\phi_k(z)$ and focus our analysis on a single period of the lattice. This period extends from $z = -b$ to $z = a$, while the interface of the potential barriers locates at the origin $z = 0$. A picture of this situation is shown in Fig. 3.4.

We start by imposing that $\phi_k(z)$ must be continuous at the barrier interface, i.e., at $z = 0$. Accordingly,

$$\phi_k^{\mathrm{b}}(0) = \phi_k^{\mathrm{w}}(0). \tag{3.35}$$

This equality yields the following conditions:

$$n_1^{\mathrm{b}}(0) = \phi_k^{\mathrm{w}}(0), \tag{3.36}$$

$$S_0^{\mathrm{b}} - S_0^{\mathrm{w}} = 2n_s\pi, \qquad n_s \in \mathbb{Z}. \tag{3.37}$$

The first of these equations corresponds to the continuity of the density profile at the barrier interface. The second condition forces the phase difference between the function in one side and on the other side to be an integer multiple of 2π.
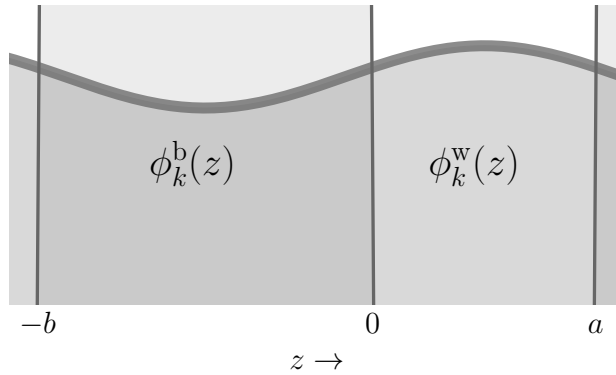

Figure 3.4: Identification of the periodic function $\phi_k(z)$ of the Bloch state by region. The darker regions correspond to the potential barriers (superscript "b"), while the blank regions correspond to the wells (superscript "w").

The periodicity of $\phi_k(z)$, Eq. (3.15), can be stated as

$$\phi_k^{\rm b}(-b) = \phi_k^{\rm w}(a), \tag{3.38}$$

which in turn corresponds to the conditions

$$n_1^{\rm b}(-b) = n_1^{\rm w}(a), \tag{3.39}$$

$$k(a+b) = 2n_s\pi + \int_{-b}^0 \frac{\alpha^{\rm b}}{n_1^{\rm b}(z')}\,dz' + \int_0^a \frac{\alpha^{\rm w}}{n_1^{\rm w}(z')}\,dz'. \tag{3.40}$$

In these equations, $\alpha^{\rm b}$ is the current density in the barriers region, and $\alpha^{\rm w}$ is the current density in the wells region.

Next, we impose the condition that the derivative of $\phi_k(z)$ must be continuous at the interface of the barriers,

$$\partial_z\phi_k^{\rm b}(0^-) = \partial_z\phi_k^{\rm w}(0^+). \tag{3.41}$$

This condition results in the following conditions,

$$\partial_z n_1^{\rm b}(0^-) = \partial_z n_1^{\rm w}(0^+), \tag{3.42}$$

$$\alpha^{\rm b} = \alpha^{\rm w}. \tag{3.43}$$

The first condition corresponds to the continuity of the derivative of the density. The second condition follows from the continuity of the derivative of the phase $S(z)$; according to Eq. (3.33), it is nothing more than the conservation of the current for a stationary state.

Finally, the derivative of $\phi_k(z)$ must be periodic too, which implies that

$$\partial_z n_1^{\rm b}(-b) = \partial_z n_1^{\rm w}(a). \tag{3.44}$$

The periodicity of the phase derivative, Eq. (3.25), follows from Eq. (3.44) and Eq. (3.43). Thus, Eqs. (3.35) to (3.44), together with the normalization condition

$$N_{\rm cell} = \int_{-b}^0 n_1^{\rm b}(z)\,dz + \int_0^a n_1^{\rm w}(z)\,dz \tag{3.45}$$

define the full set of solutions for the wave function of the condensate.

We can use the definition and the properties of the Jacobi elliptic functions in order to find a closed-form expression for the normalization condition. Following the notation of [101], we obtain that the integral of the density Eq. (3.31) is

$$\int_0^z n_1(z')\,dz' = (n_{1({\rm off})} + 4\lambda^2)z - $$
$$\frac{4\lambda}{\sqrt{4mg_{\rm 1D}/\hbar^2}} \times \Big(\mathcal{E}(u(z)|m_{\rm j}) - \mathcal{E}(u(0)|m_{\rm j}) \Big), \tag{3.46}$$

where $\mathcal{E}(u(z)|m_{\mathrm{j}})$ is the incomplete elliptic integral of the second kind of argument $u(z) = \sqrt{4g_{1\mathrm{D}}m/\hbar^2}\lambda(z - z_{\mathrm{off}})$ in canonical form [101]. Equation (3.46) corresponds to the average number of particles in the interval $[0, z]$. Please refer to the Appendix A additional details about the Jacobi elliptic functions and elliptic integrals. Then the normalization condition can be expressed in terms of Eq. (3.46), where each of the constants should be labeled to indicate the interval where the integration of $n_1(z)$ is being carried out.

We proceed similarly with the condition Eq. (3.40). First, the integral in the r.h.s. of Eq. (3.26) is, according to [101],

$$\int_0^z \frac{dz'}{n_1(z')} = \frac{1}{\sqrt{4mg_{1\mathrm{D}}/\hbar^2}\lambda n_{1(\mathrm{off})}} \times$$
$$\left(\Pi\left(n_{\mathrm{j}}; u(z)|m_{\mathrm{j}}\right) - \Pi\left(n_{\mathrm{j}}; u(0)|m_{\mathrm{j}}\right) \right), \tag{3.47}$$

where $\Pi(n_{\mathrm{j}}; u(z)|m_{\mathrm{j}})$ is the incomplete elliptic integral of the third kind of order $n_{\mathrm{j}} = -4m_{\mathrm{j}}\lambda/n_{1(\mathrm{off})}$. With this result, Eq. (3.40) can be expressed in terms of Eq. (3.47), with the correct labeling for the density.

3.4. Ground State Density Profile

Up to this point, we have found analytic expressions for the density profile, phase, and normalization condition of the condensate. Also, we established the boundary conditions that the wave function of the condensate must satisfy. In principle, by solving the nonlinear set of equations (3.35)–(3.44), we can find the unknowns that fix the density profile Eq. (3.31) such that $\phi_k(z)$ is correctly normalized. However, applying this procedure is not an easy task because of the complex dependence of the Jacobi elliptic functions on its arguments. A more convenient and robust approach to calculate the wave function is to use *nonlinear finite differences* [102] on Eq. (3.16). The method is applied by imposing periodic boundary conditions Eq. (3.38), as well as the normalization condition Eq. (3.18).

A remark on energy units: we know that l (the potential period) is the distance between the midpoints of any two consecutive barriers, as well as the distance between the midpoints of two consecutive wells. Making an analogy with an optical lattice, we can identify the recoil energy of our multi-rod system as

$$E_{\mathrm{R}} \equiv \frac{\hbar^2\pi^2}{2ml^2}, \tag{3.48}$$

43

which is equal to the recoil energy of an optical lattice with period l following Eq. (3.2). In this way, Eq. (3.48) becomes the natural energy scale of our system. On the other hand, we establish the base on which our system can be used to describe the physics of interacting Bose gases confined in a 1D optical lattice.

We start by calculating the density profile $n_1(z) = |\phi_k(z)|^2$ of the ground state, $k = 0$, of a Bose gas with repulsive interactions (positive $g_{1\mathrm{D}}$). In Fig. 3.5a, we show the density profile for a square lattice $b = a$ ($r = 1$) of height $V_0 = 5E_\mathrm{R}$. We have plotted the density profile for the IBG, as well as for $g_{1\mathrm{D}}n_1 = 0.5$, 1, 2, and 3 times V_0. Results show that the density profile changes notoriously concerning the IBG density as the interaction strength increases. For all cases, the density is maximum at the well's midpoint and minimum at the center of the barrier. Also, as the interaction strength increases, the density profile becomes flatter. We see an evident competition between the
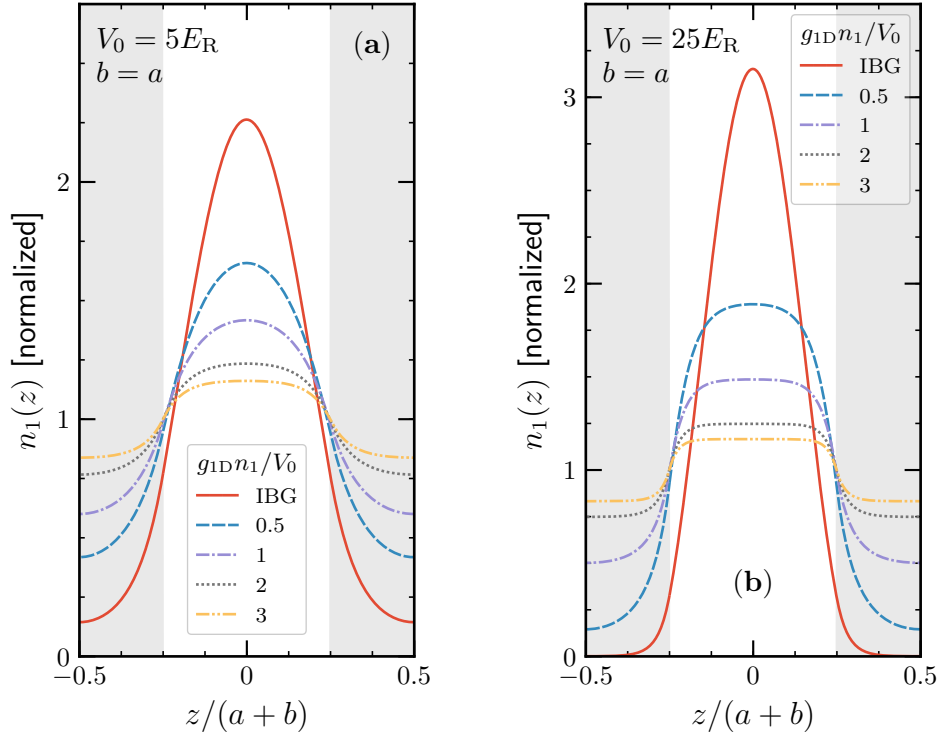

Figure 3.5: Ground state density profile for a square lattice for several values of the repulsive interaction strength. The dark regions indicate the location of the potential barriers.

repulsive potential barriers and the repulsive force between bosons. When the potential repulsion dominates, there is a notorious localization of the particles in the wells, which is maximum for the IBG. On the other hand, as the repulsion between particles increases, the localization diminishes, and the density profile becomes flatter. However, there is still a depletion of the condensate inside the barriers, which eventually disappears for $g_{1D}n_1 \gg V_0$, when the (normalized) density profile takes an almost constant value around unity.

We can change the geometry of the KP potential, so we no longer have a square lattice. For example, we have calculated the density profile for two nonsquare lattices keeping the height of the barriers fixed at $V_0 = 25E_R$. In Fig. 3.6a, we have a lattice with $b = 0.5a$, which means that the barriers are thinner than the wells. We see a density profile with similar characteristics than the density profile of the square lattice Fig. 3.5b; however, since the barriers are smaller, the size of the depleted region is reduced, and the condensate is slightly
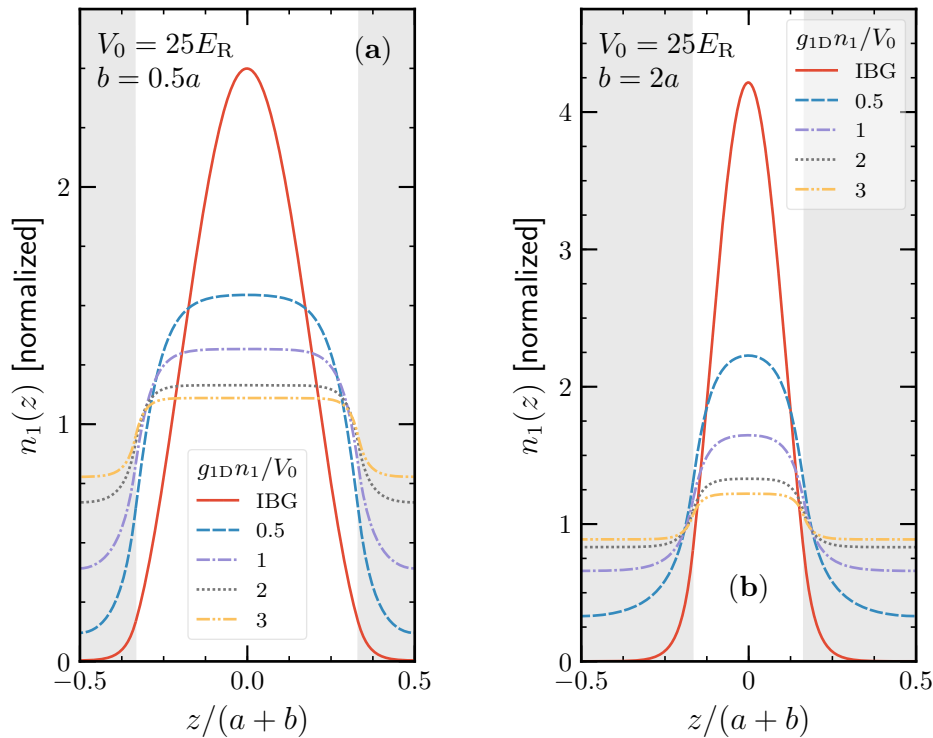

Figure 3.6: Ground-state density profile for a square lattice for several values of the repulsive interaction strength. The dark regions indicate the location of the potential barriers.

less localized (the peak density is lower than in Fig. 3.5b). In Fig. 3.6b, we show the density profile for a lattice with $b = 2a$, i.e., the barriers are broader than the wells. Beyond the evident similarities with Fig. 3.6a, we see an even greater localization when the barriers are wider than the wells, a direct consequence of the dominant repulsive effect of the external potential. Finally, as in the case of the square lattice, increasing the interaction strength makes the density more uniform.

3.5. Chemical Potential and Nonlinear Energy Spectrum

Solving the Gross-Pitaevskii equation gives us, at first instance, both the chemical potential μ_{1D} and the wave function of the condensate, $\Phi_{1D}(z)$. Then, we can calculate the total energy of the system from Eq. (3.20). We can find a direct relationship between the chemical potential and the total energy from Eq. (3.16). If we multiply both sides of Eq. (3.16) by $\phi_k^*(z)$ and integrate over a single period of the potential, we find that

$$\mu_{1D} = \frac{1}{N_{cell}} \int_0^l \phi_k^*(z) \hat{\boldsymbol{H}}_{GP_{1D}}^{(k)} \phi_k(z) \, dz, \tag{3.49}$$

result which we obtain after using the normalization condition Eq. (3.18). The term on the r.h.s. of Eq. (3.49) results to be very similar to the r.h.s. of Eq. (3.20). It is not hard to prove that

$$\mu_{1D} = \frac{E[\Phi_{1D}]}{N_{cell}} + \frac{g_{1D}}{2N_{cell}} \int_0^l n_1^2(z) \, dz, \tag{3.50}$$

where the Bloch state $\Phi_{1D}(z)$ has a quasimomentum k. Since $g_{1D} n_1$ is positive, the chemical potential is always greater than the energy per particle. Also, when the interaction between the particles vanishes, μ_{1D} reduces (as expected) to the energy per boson, which is precisely the chemical potential of a noninteracting, ideal Bose gas.

We saw in Fig. 3.3b that the energy spectrum of the ideal Bose gas has bands of accessible energies, separated by forbidden bands. How the presence of interactions changes the spectrum? We can look at the results in Fig. 3.7a, where we have plotted the energy per particle as a function of the quasimomentum k for the IBG (dashed line), as well as the energy for an interacting gas with $g_{1D} n_1 = 0.5 E_R$ (solid line), in a lattice with $V_0 = 5 E_R$ and $b = a$. Also, we plotted the chemical potential (dash-dot-dot line) of the interacting gas. For this particular example, the interaction factor $g_{1D} n_1$ is relatively small compared to the lattice height. Accordingly, the energy bands of the interacting gas look

slightly distorted concerning the bands of the IBG. Also, a small offset appears due to the interactions. The chemical potential does not change noticeably either.

When the interaction becomes more significant, such as the example shown in Fig. 3.7b where $g_{1D}n_1 = 5E_R$ (as large as the lattice height),there is a remarkable change in the bands of the interacting gas. First, the offset between the interacting gas energy and the IBG energy becomes larger. Second, loops appear in the energy bands at zero quasimomentum for the second band, and also at the edges of the first BZ for the first and third band. The presence of loops (commonly known as *swallowtails*) is a feature shared with other periodic structures such as the optical lattice potential [103] and the Dirac comb potential [104, 105].

E. Muller explained [106] the swallowtail phenomena origin in terms of the response of a superfluid 1D Bose gas within a periodic lattice to an external constant force field. In this situation, we start with a system in rest regarding
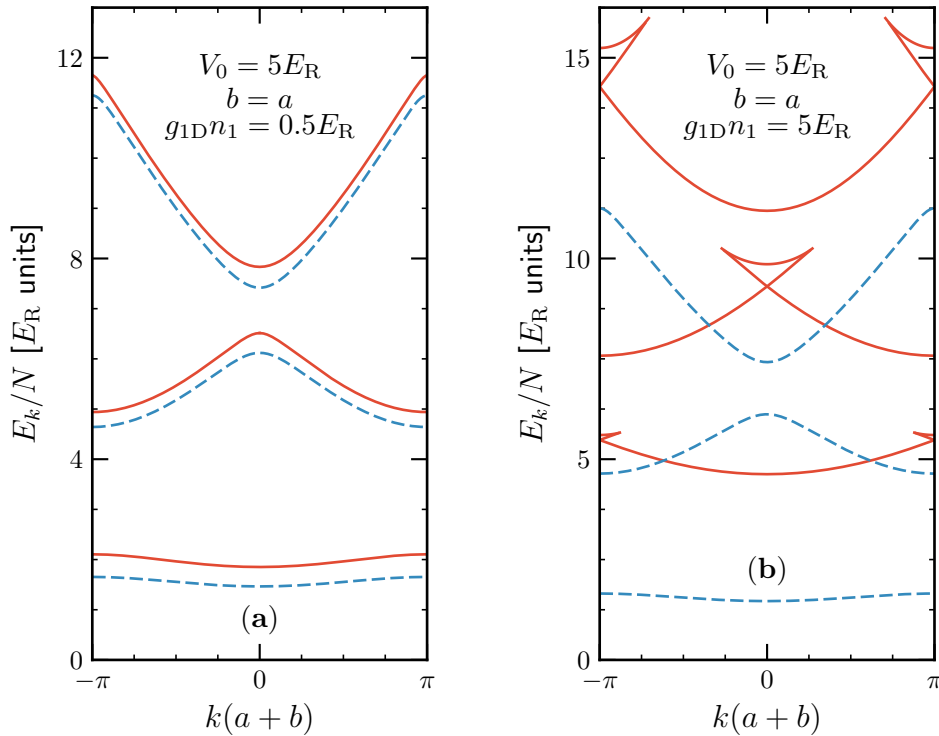

Figure 3.7: Nonlinear energy spectrum. The dashed line indicates the energy bands of the IBG. The solid line is the nonlinear energy spectrum.

the reference frame of the lattice, i.e., zero quasimomentum k (which lies in the lowest band of the energy spectrum). Then we apply a small constant force field additionally to the lattice potential [49]. For a Bose gas with relatively small interactions (like the one shown in Fig. 3.7a), the quasimomentum will increase with time. At the same time, the BEC energy will follow (under the adiabatic approximation) the solid curve that represents the band. Beyond the first BZ, the energy band repeats periodically; therefore, the group velocity of the condensate,

$$v_{\mathrm{g}} \equiv \frac{\partial E_k}{\partial k}, \tag{3.51}$$

will be periodic too. This phenomenon is known as *Bloch oscillations* [107, 108]. For a BEC with relatively strong interactions (like the one shown in Fig. 3.7b), the superfluid can screen out the lattice up to an extent. Then its energy spectrum will resemble more like the free Bose gas energy spectrum. As the gas accelerates, its energy will follow the path of the energy band; when its velocity exceeds the critical velocity of superfluidity, the gas can not screen the potential anymore, and the band terminates at some k, taking the characteristic swallowtail shape.

The loops are a consequence of the appearance of two local minima separated by a local maximum in the energy landscape defined by Eq. (3.20). To understand this change, we should remember that the states $\phi_k(z)$ that satisfy Eq. (3.16) subject to Eq. (3.18) are minimizers of the energy functional Eq. (3.20). When the interaction strength $g_{\mathrm{1D}}n_1$ is small compared with V_0, only one of such states exist, so the band has the typical shape that resembles the IBG bands. However, as the interaction increases, two local minima may appear for a single k value, which must be separated by a local maximum for purely topological reasons.

Regarding our system, a 1D Bose gas with contact-like interactions at zero temperature is a Lieb-Liniger Bose gas, which is a Luttinger liquid and also is a superfluid. Hence the applicability of the previous explanation about the origin of the swallowtails to our system is justified.

3.6. Compressibility

The compressibility it directly related to the chemical potential through the relation

$$\kappa^{-1} \equiv n_1 \frac{\partial \mu_{\mathrm{1D}}}{\partial n_1} \tag{3.52}$$

for a fixed k. It is an important quantity since it is required to calculate the sound velocity in the condensate (as we will see in Section 3.7). In Fig. 3.8, we show results of the chemical potential and the compressibility κ for the ground state $k = 0$ of a square lattice. Figure 3.8a shows both properties as functions of the interaction strength $g_{1D}n_1$, while Fig. 3.8b shows the dependence as a function of the lattice height V_0.

First, we focus on Fig. 3.8a, where we see that μ_{1D} is a monotonically increasing function of $g_{1D}n_1$. Also, we note that larger values of V_0 increase the value of μ_{1D} further. At zero $g_{1D}n_1$ (IBG), all the curves tend to group as V_0 increases. This behavior is an expected result, since for the IBG, the chemical potential is the energy of the ground state, and we have seen in Section 3.2 that as V_0 grows, the ground state energy approximates to the energy level $4E_R$ according to Eq. (3.11). Significant differences appear at intermediate values of $g_{1D}n_1$ when it is less or similar than V_0, but not greater. For $g_{1D}n_1 > V_0$, we appreciate that the chemical potential grows linearly with the interaction factor. Analytically, we can analyze this situation by looking at the density profiles of the gas in Fig. 3.5, where we can see that as the integration strength increases, the profiles become flatter. Then, for $g_{1D}n_1 \gg V_0$, the kinetic energy term, i.e., the term with the derivative in the GPE Eq. (3.16), will be negligible concerning the sum of the external potential and the interaction terms. The GPE reduces to

$$\left(V_{KP}(z) + g_{1D}|\phi_k(z)|^2 \right) \phi_k(z) = \mu_{1D}(z)\phi_k(z), \qquad (k = 0), \qquad (3.53)$$

which has the solution

$$n_1(z) = |\phi_k(z)|^2 = \left(\mu_{1D} - V_{KP}(z) \right)/g_{1D}, \qquad (k = 0). \qquad (3.54)$$

The normalization condition Eq. (3.18) fixes the chemical potential. Integrating both sides of Eq. (3.53) over one potential period, we find the result

$$\mu_{1D} = g_{1D}n_1 + \frac{r}{1+r}V_0, \qquad (k = 0). \qquad (3.55)$$

The assumption under which we neglect the kinetic energy term in the GPE is commonly known as the *Thomas-Fermi* (TF) approximation. It predicts that the energy to add a particle to the trapped gas is equal to the chemical potential of a free, uniform Bose gas with the same average density plus a constant term arising from the trapping potential $V_{KP}(z)$. Chemical potential results in Fig. 3.8 confirm this prediction.

Results in Fig. 3.8b show that we have infinite compressibility for zero $g_{1D}n_1$, precisely as an IBG at zero temperature. At nonzero $g_{1D}n_1$, we note

49

a reduction of the compressibility concerning the free Bose gas (solid line), which occurs mainly because of the repulsive interaction between the particles. The increase of the external potential, which is repulsive too, reduces the compressibility even further. This effect manifests more strongly in the intermediate regime of interactions. When $g_{1D}n_1 \gg V_0$, all the curves tend to gather around the expected result $\kappa^{-1} = g_{1D}n_1$ of the free Bose gas, which is the result predicted straightforwardly by the TF approximation from substituting Eq. (3.55) in Eq. (3.52).

Figure 3.8c shows the chemical potential as a function of the lattice height V_0. Each curve corresponds to a different value of $g_{1D}n_1$ (see figure caption).
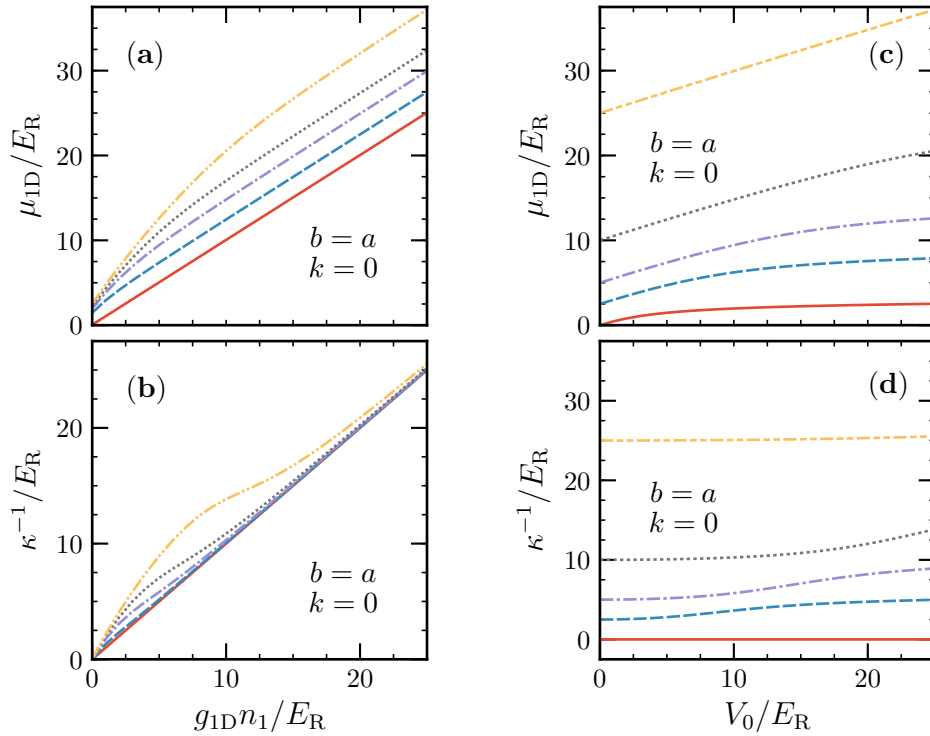
Figure 3.8: Chemical potential and compressibility for the ground state $k = 0$ of a square lattice $b = a$. **(a)** and **(b)**: as a function of the interaction strength. The solid line corresponds to the free gas. Dashed lines, from top to bottom, correspond to lattice heights $V_0 = 25, 15, 10$ and 5 times E_R. **(c)** and **(d)**: as a function of the lattice height. The solid line corresponds to the noninteracting gas. Dashed lines, from top to bottom, correspond to $g_{1D}n_1 = 25, 10, 5$, and 2.5 times E_R.

For the IBG (solid line), we have the same results as those shown in Fig. 3.3b, i.e., the chemical potential (which is equal to the energy of the ground state) tends to the value $4E_{\mathrm{R}}$ as V_0 increases. We can see that all of the curves start at $g_{1\mathrm{D}}n_1$ when the lattice height is zero since the gas is free, and the chemical potential follows the relation Eq. (2.71). For intermediate values of $g_{1\mathrm{D}}n_1$, the $\mu_{1\mathrm{D}}$ shows a similar behavior as the IBG. However, as the interaction approximates to V_0 or becomes larger (for instance, for $g_{1\mathrm{D}}n_1 = 25E_{\mathrm{R}}$), we can see a clear linear dependence of $\mu_{1\mathrm{D}}$ on V_0 as predicted by the TF approximation. The compressibility in Fig. 3.8d is infinite for the IBG.

3.7. Sound Velocity

For a Bose gas confined in a periodic structure like an optical lattice or a multi-rod lattice, the microscopic nature of the lattice, as well as the action of interactions between particles, have a direct influence on the energy spectrum E_k. Around a minimum of the energy, these effects get absorbed by the effective mass m_{eff},

$$m_{\mathrm{eff}}^{-1} \equiv \frac{1}{\hbar^2} \left. \frac{\partial^2 E_k}{\partial k^2} \right|_{k_0}. \tag{3.56}$$

On the other hand, that influence becomes reflected in the compressibility κ as we have seen in Section 3.6. Both effects influence the sound velocity of a Bose-Einstein condensate through the thermodynamic relation [50, 109]

$$c_{\mathrm{s}} = \frac{1}{\sqrt{\kappa m_{\mathrm{eff}}}}. \tag{3.57}$$

For a free, 1D weakly-interacting Bose gas, the inverse of the compressibility is $\kappa^{-1} = g_{1\mathrm{D}}n_1$, while $m_{\mathrm{eff}} = m$ due to the absence of a lattice, so the sound velocity is given by the well-known relation [45]

$$c_{\mathrm{s(free)}} = \sqrt{\frac{g_{1\mathrm{D}}n_1}{m}}. \tag{3.58}$$

In the presence of the multi-rod lattice, we have to resort to numerical calculations to estimate both the effective mass and compressibility.

In Fig. 3.9a, we show the dependence of the inverse of effective mass as a function of the interaction strength $g_{1\mathrm{D}}n_1$. The results show two behaviors: first, for a fixed value of $g_{1\mathrm{D}}n_1$, the effective mass becomes larger as the lattice height increases, since the bosons *seem* heavier due to the repulsive interaction with the external potential. Second, for a fixed value of V_0, the effective

mass raises as the interaction strength increases. This behavior reflects how the repulsive interactions counteract the localization effect of the barriers, which favors the tunneling of bosons since they seem lighter. The effective mass is a monotonically increasing function of the interaction strength. For large enough values of $g_{1D}n_1$, it will approximate to the real mass m due to the screening effect of the repulsive interactions between bosons on the lattice. In Fig. 3.9b, we show the dependence of m_{eff} on the lattice height for $g_{1D}n_1 = 0.25$, 0.5, and one times E_R. As expected, for zero lattice height, both effective mass and true mass coincide, while for nonzero V_0, the effective mass is a monotonically increasing function of V_0. The interaction strength causes a reduction of the m_{eff}, an effect that we also see in Fig. 3.9a.

Finally, in Fig. 3.10, we show the sound velocity (relative to the sound velocity of the weakly-interacting free Bose gas $c_{s(free)}$) as a function of the lattice height for $g_{1D}n_1 = 0.25$, 0.5 and one times E_R. We can see that, for zero lattice height, the sound velocity is equal to $c_{s(free)}$ for every value of $g_{1D}n_1$, as expected. Then it becomes a monotonically decreasing function of the lattice
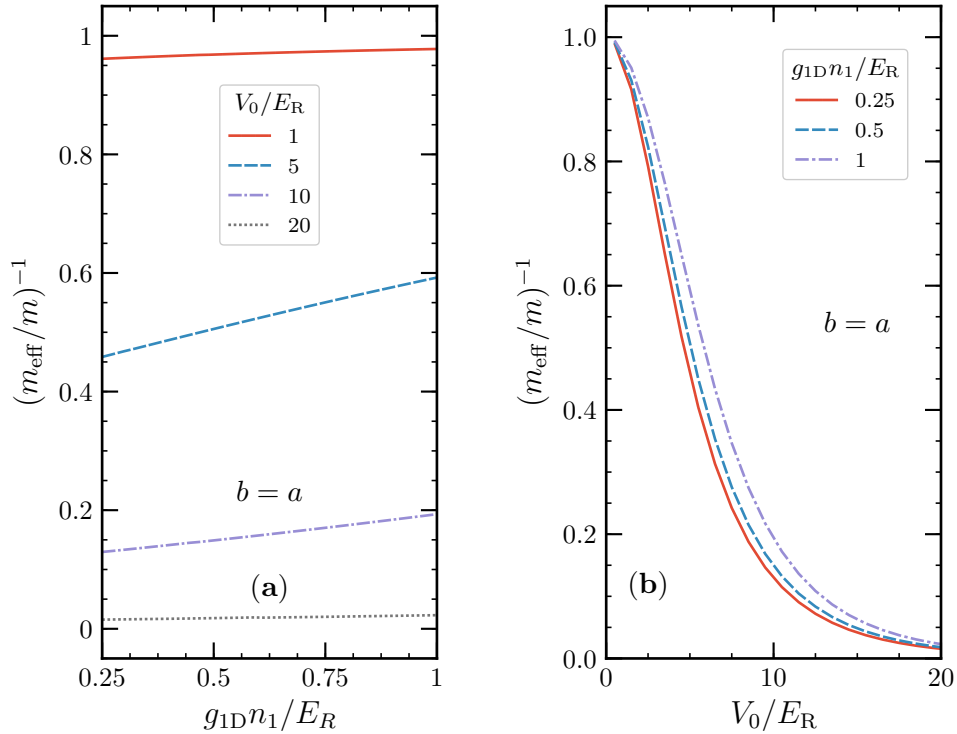
Figure 3.9: The inverse of the effective mass for the Bose gas in a square lattice.
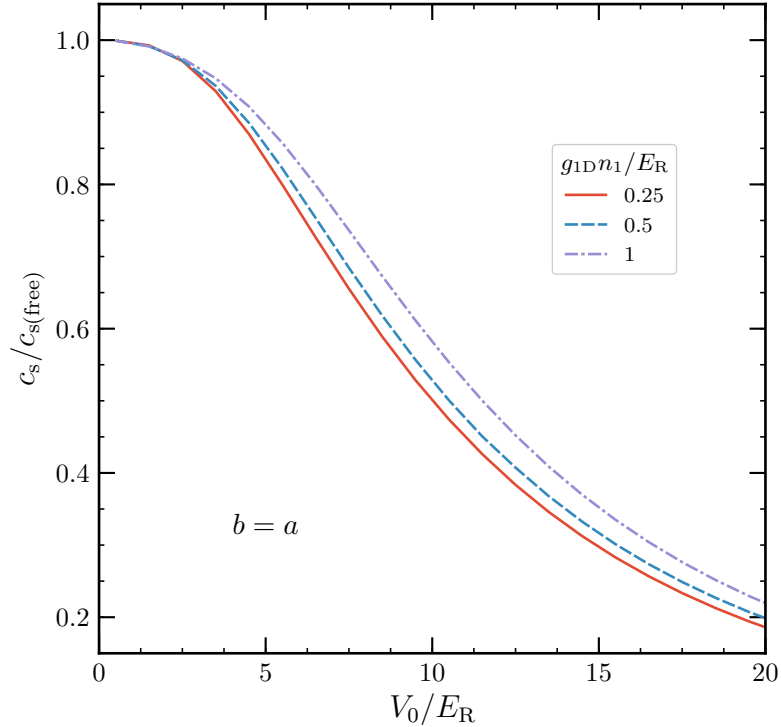
Figure 3.10: Sound velocity for a square lattice.

height. Comparing results in Fig. 3.10 with those in Fig. 3.9b, we see that the effective mass determines the qualitative behavior of c_{s}. Increasing the magnitude of the repulsive interactions increases the sound velocity.

3.8. The Limit of Ultranarrow Barriers

A feature of the KP potential is that as the barriers become very narrow and the barriers very height, but the product $V_0 b$ remains constant, every potential barrier approaches a Dirac-δ potential. Then, the KP potential becomes a succession of δ-functions centered in the positions jl, being j an integer and l the KP potential period, as well as the separation between two contiguous deltas. The expression Eq. (3.5) becomes the Dirac comb potential,

$$V_{\mathrm{DC}}(z) = V_0 b \sum_{j=-\infty}^{\infty} \delta(z - jl), \tag{3.59}$$

where the finite, constant value $V_0 b$ is the area below a single barrier of the KP potential. This area can be interpreted as a measure of permeability, as well

3. WEAKLY-INTERACTING BOSE GAS IN MULTI-RODS

as the strength of a single δ barrier. When $V_0 b$ becomes zero, we recover the homogeneous, free interacting Bose gas. On the other hand, as the delta strength increases and goes to infinite, the system resembles more and more succession of independent boxes separated by infinite walls of width l.

Significant research exists on the thermodynamics of noninteracting Bose gases subject to Dirac comb potential [110, 111]. Investigated properties include the Bose-Einstein condensation temperature and heat capacity. In the context of interacting Bose gases, the Dirac comb potential has been studied before; for instance, by [51, 104, 105, 112] [1]. Beyond the theoretical interest of the problem, in recent years, the experimental realization of the Dirac comb potential has become a reality [36, 37] (more on this subject in Section 3.8.1).

The delta strength $V_0 b$ is an energy times a length. As such, we can redefine it as

$$V_0 b \equiv s E_{\mathrm{R}} l, \tag{3.60}$$

where E_{R} is the recoil energy of the Dirac comb lattice, which, according to Eq. (3.59), is equal to Eq. (3.48). Definition Eq. (3.60) may seem somewhat arbitrary, but is very useful when we write Eq. (3.59) in terms of the scaled length $z' = z/l$ as

$$V_{\mathrm{DC}}(z') = s E_{\mathrm{R}} \sum_{j=-\infty}^{\infty} \delta(z' - j), \tag{3.61}$$

where we have used the scaling property of the delta function, $\delta(lz) = \delta(z)/l$. Then, the factor s arises naturally as the strength of the δ barriers in E_{R} units. Furthermore, it establishes a connection between the KP parameters and the DC potential. In Fig. 3.11a, we show the density profile for several values of the interaction factor $g_{1\mathrm{D}} n_1$, as the multi-rod lattice approximates to the Dirac comb limit. We have chosen $V_0 = 20 E_{\mathrm{R}}$ and $b = 0.05a$, such that the delta strength is $s = 1$, according to Eq. (3.60). The density profile shares some characteristics with the one of square lattice in Fig. 3.5: is maximum in the midpoint of the well, and it becomes flatter as $g_{1\mathrm{D}} n_1$ increases. However, in the region occupied by the barriers, the density profile shows a quick variation due to the relatively strong potential barriers. In Fig. 3.11b, we show analog results when the height of the barriers increases to $V_0 = 200 E_{\mathrm{R}}$, and their width reduces to $b = 0.005a$ such that we still have $s = 1$. We see that the density remains essentially unchanged, except at the barrier locations, where effectively it has a peak that is consistent with the results for a Dirac comb potential. We

---

[1]In these works, the Dirac comb potential is incorrectly referred to as the KP potential.
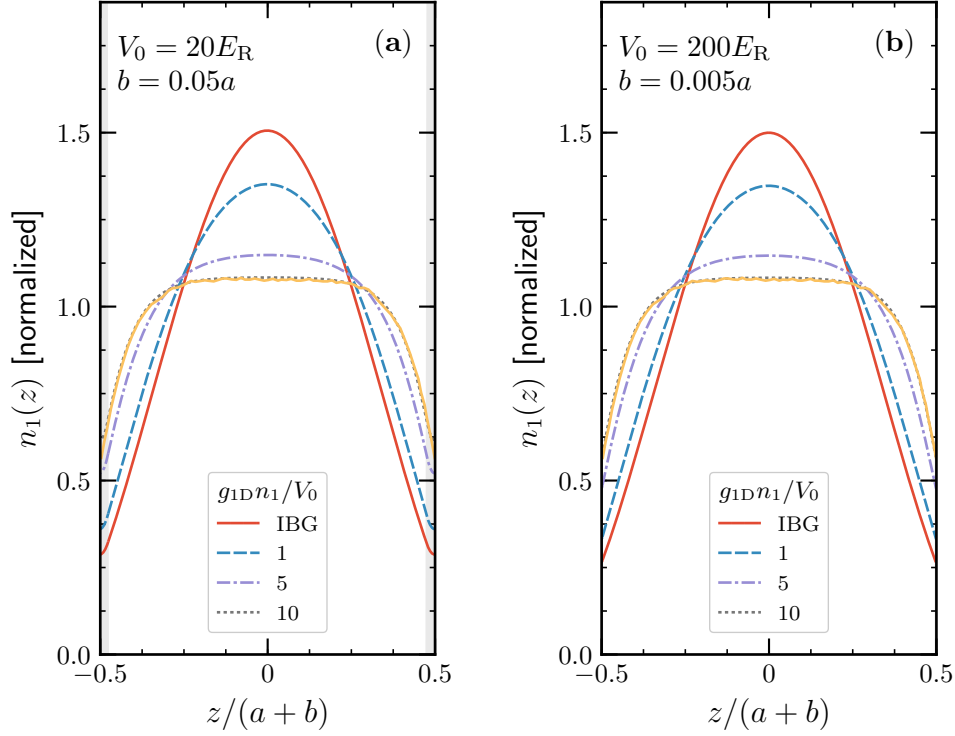
Figure 3.11: Ground state density profile for several values of the repulsive interaction strength in the Dirac comb approximation. The dark regions indicate the location of the potential barriers.

can conclude that for barriers of height $V_0 = 20E_R$ or higher, and $b = 0.05a$ or thinner, the multi-rod structure is an excellent approximation of the Dirac comb potential.

In Fig. 3.12a, we show the energy spectrum for the lattice with $V_0 = 20E_R$, $b = 0.05a$, and $g_{1D}n_1 = E_R$, which can be considered a condensate with relatively small interactions. We see that the interacting spectrum is very similar to the IBG spectrum, just slightly distorted and shifted to higher energies because of the repulsive KP. As we further increase the interacting factor to $g_{1D}n_1 = 10E_R$ in Fig. 3.12b, the swallowtails appear at the center and edges of the first Brillouin zone, just as in the case of the square lattice in Fig. 3.7. A particular result for the Dirac comb potential obtained by [104] states that the swallowtails appear if the interaction strength is $g_{1D}n_1 \geq 2sE_R$. Clearly, for results in Fig. 3.12 where $s = 1$, this criterion is not met for $g_{1D}n_1 = E_R$, but it is for $g_{1D}n_1 = 10E_R$.
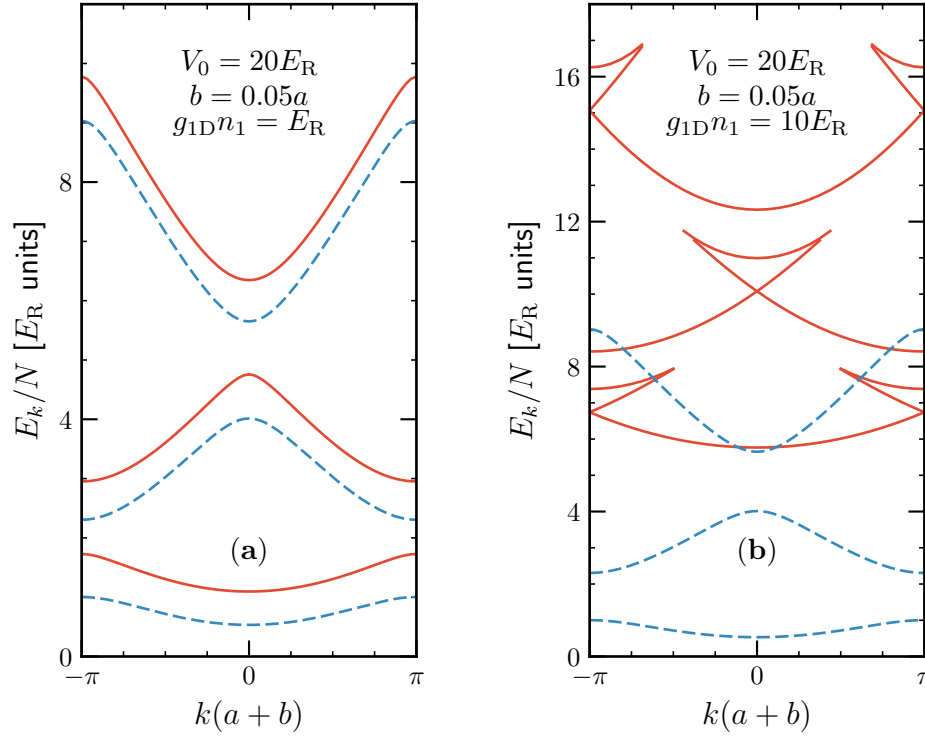
Figure 3.12: Nonlinear energy spectrum in the Dirac comb approximation. The dashed line indicates the energy bands of the IBG. The solid line indicates the nonlinear energy spectrum.

3.8.1. Ultranarrow Barriers to Study Subwavelength Optical Lattices

Atoms confined in optical lattices follow the spatial variations of the trapping light intensity. Consequently, the spatial resolution of the lattices is limited by the light wavelength λ_{OL}, which is of the order of hundreds of nanometers. In recent years there has been an increasing interest, as well as technical advances, to generate optical lattices with subwavelength spatial structure (SWOL) [36, 37, 113]; in these lattices, the barriers can reach widths less than ten nanometers. The result of these efforts is a conservative 1D optical lattice of the form

$$V_{\text{OL}}(z) = \frac{\epsilon^2 \cos^2(k_{\text{OL}} z)}{\left[\epsilon^2 + \sin^2(k_{\text{OL}} z)\right]^2} E_{\text{R}}, \tag{3.62}$$

where $k_{\text{OL}} = 2\pi/\lambda_{\text{OL}}$, E_{R} is the recoil energy of the optical lattice given by Eq. (3.2), and ϵ is a factor that depends on the optical fields used to produce
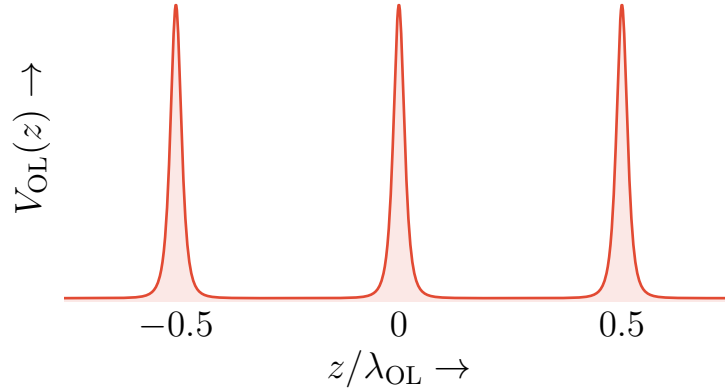
Figure 3.13: Subwavelength optical potential schematic with $\epsilon = 0.14$.

the lattice. In the limit when $\epsilon \ll 1$, this potential generates a lattice of narrow barriers separated by a distance $\lambda_{\mathrm{OL}}/2$, height $E_{\mathrm{R}}/\epsilon^2$, and width $\epsilon\lambda_{\mathrm{OL}}/2\pi \ll \lambda_{\mathrm{OL}}/2$. Effectively, this lattice is a very close representation of the Dirac comb (DC) potential formed by a sequence of δ-function potential barriers.

We model the subwavelength optical potential in the limit when $\epsilon \ll 1$ using our multi-rod system in the Dirac comb limit. First, both potentials should have the same period, i.e., $l = a + b = \lambda_{\mathrm{OL}}/2 = l_{\mathrm{OL}}$. Since the height of the optical potential and the average width are $E_{\mathrm{R}}/\epsilon^2$ and $\epsilon\lambda_{\mathrm{OL}}/2\pi$ respectively, only ϵ is a free parameter for the optical lattice. For the KP potential, the height V_0 and the barriers width b are free parameters. Second, we have to choose the parameters such that the strength of both potentials, i.e., the area below the curve $V_{\mathrm{OL}}(z)$ within one period, and the product $V_0 b$ for the KP potential, are equal.

Since a subwavelength optical potential with $\epsilon = 0.14$ is analyzed in [37], we will use this value to fix the parameters V_0 and b of our multi-rod lattice. On the other hand, we know that the width of a single barrier of Eq. (3.62) is $\epsilon\lambda_{\mathrm{OL}}/2\pi$ (with $\lambda_{\mathrm{OL}}/2$ the period of the lattice), then the barrier size is approximately $0.0466(\lambda_{\mathrm{OL}}/2)$. In the multi-rod model, we can get a similar relation between the width of the barrier and the potential period with a lattice ratio $r = 0.05$, which is the potential whose density profile and energy spectrum are shown in Fig. 3.11a and Fig. 3.12, respectively. Finally, using $b = r/(1 + r)l$ and matching the strength of both potentials, we obtain $V_0 \approx 74.3E_{\mathrm{R}}$, which is somewhat larger than the height $51.02E_{\mathrm{R}}$ of the subwavelength optical lattice peak.

In Fig. 3.14a, we show the density profile of the system derived in the previous paragraph: $V_0 = 74.3E_{\mathrm{R}}$ and $b = 0.05a$. We show the results for the
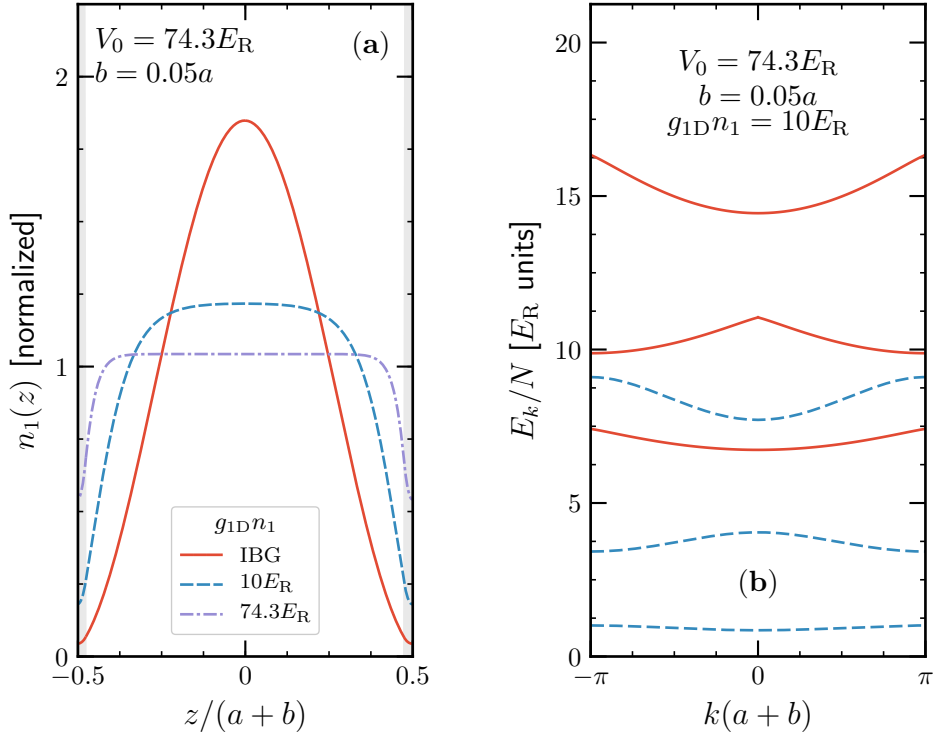
Figure 3.14: **(a)**: Density profile for the KP lattice with ultranarrow barriers for the IBG and $g_{1D}n_1 = 10$ and 74.3 times E_R. Results correspond to $\epsilon = 0.14$ in the subwavelength optical potential Eq. (3.62). The darker regions indicate the location of the barriers. **(b)**: The nonlinear energy spectrum of the same system with $g_{1D}n_1 = 10E_R$. The dashed line indicates the energy bands of the IBG, while the solid line shows the nonlinear energy spectrum.

noninteracting case, i.e., the IBG, as well as for $g_{1D}n_1 = 10$ and 74.3 times E_R. For the interacting cases, it is clear the effect of the interactions, since the density profiles differ considerably from the IBG profile. In Fig. 3.14b, we show the energy spectrum for $g_{1D}n_1 = 10E_R$ where, although it differs significantly from the IBG spectrum, swallowtails are not significant.

Finally, we would like to analyze under which conditions the density profile and energy spectrum in Fig. 3.14 could be considered good predictions. We know that any result obtained from the GPE will be accurate if the Bose gas belongs to the weakly-interacting regime (at zero temperature). This condition is fixed by Eq. (2.66), which is a high-density limit in a one-dimensional Bose gas. We saw in Section 2.8 that the exact description of a 1D Bose gas with contact-like, repulsive interactions is given by the Lieb-Liniger model [24] and

the LL parameter $\gamma = mg/\hbar^2 n_1$, which must satisfy $\gamma \ll 1$ in order to the GPE picture to be valid.

We can relate the interaction factor $g_{1D}n_1$ and the LL parameter γ through the relation

$$\gamma = \frac{1}{2}\left(\frac{n_1 l}{\pi}\right)^{-2}\frac{g_{1D}n_1}{E_R} \tag{3.63}$$

where the dimensionless quantity $n_1 l$ is also referred to as *filling factor* since it quantifies the average number of particles contained in an interval with length equal to a single potential period. However, we have to note that the l.h.s. of Eq. (3.63) is a parameter of a model without external potential (LL), while the r.h.s. is a parameter for a model with or without an external potential (KP), but with a length scale l such that we can define E_R following Eq. (3.2). When we set the height of the multi-rod potential barriers to zero, we recover the free, weakly-interacting Bose gas whose properties (as functions of $n_1 l$ and $g_{1D}n_1$) can be compared to the LL model properties.

In Fig. 3.15, we show results for the energy of the exact LL model as a function of the interaction parameter, for an average density (or equivalently, the filling factor) $n_1 = 10$, 100, 250 and 500 times l^{-1}. We compare these results with the ground state energy of the weakly-interacting, free Bose gas $E/N = g_{1D}n_1/2$. For the case $n_1 = 10l^{-1}$, results show a clear difference between the exact LL and GPE results, which is a sign that for such low densities, the predictions of the mean-field theory will not be accurate (in the interval of $g_{1D}n_1$ analyzed). Results show that only in the high-density case $n_1 = 500l^{-1}$, the GPE gives accurate results over the full interval of interaction $g_{1D}n_1$. Higher densities should provide results even more accurate. For $n_1 = 100l^{-1}$, we can see small discrepancies between the GPE predictions and the LL theory. Numerical results indicate that for $n_1 = 250l^{-1}$, the GPE and LL exact results are almost identical, and it can be taken as a lower limit for suitable densities. Greater values of n_1 than $250l^{-1}$ are within the range of typical experimental densities for Bose gases in the 1D regime [57, 114].

Finally, we show the expected ground-state energy of the Bose gas constrained within the SWOL (modeled as an ultranarrow multi-rod lattice) in Fig. 3.15 by the solid, red line. The lattice raises the energy concerning the free Bose gas, and its dependence is not linear with $g_{1D}n_1$. Then, the observed energy band structure of the gas for $g_{1D}n_1 = 10E_R$ should be similar to the one shown in Fig. 3.14b.
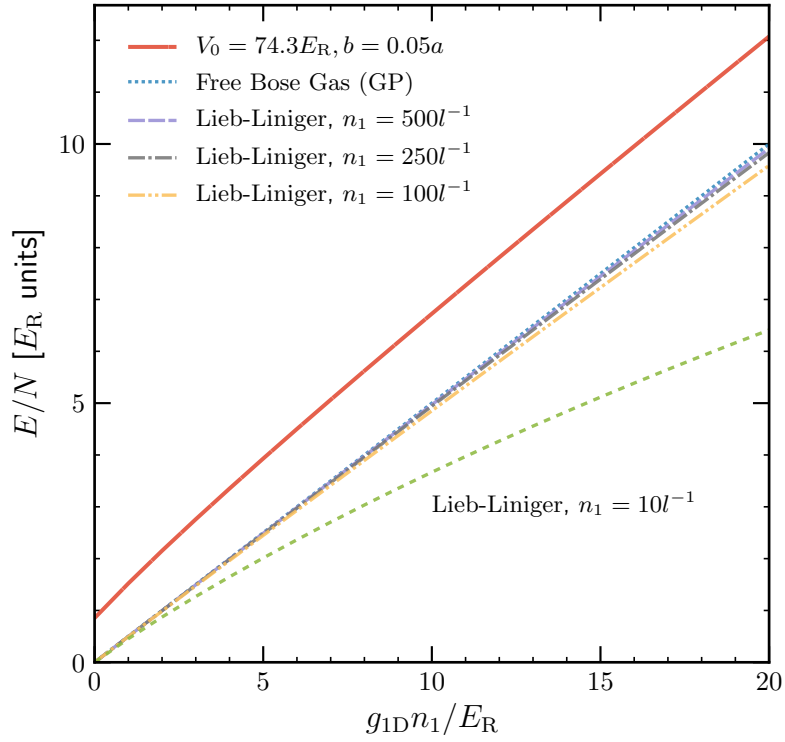
Figure 3.15: Ground-state energy as a function of the interaction strength for the Lieb-Liniger model and the multi-rod model. The solid line corresponds to the Bose gas subject to the multi-rod potential close to the Dirac comb limit. The dotted line shows the mean-field results for a free, interacting Bose gas.

4

Quantum Monte Carlo Methods

Solving the Schrödinger equation for a many-body quantum system is a challenging problem. With the advent of electronic computers, it became possible to study the properties of the ground state of a quantum many-body system using *ab-initio* methods, instead of analytical approximations to the solution of the many-body Schrödinger equation. Among many techniques developed for such a goal, there is a type of stochastic methods commonly known as *Quantum Monte Carlo* (QMC) methods. Variants of these methods differ in the way they solve the many-body problem; for instance, the *Variational Monte Carlo* (VMC) employs the variational principle of quantum mechanics to give an upper bound to the ground state energy of a quantum system. In comparison, with the *Diffusion Monte Carlo* (DMC) method, one can obtain the exact value of the ground state energy, as well as other properties, by solving the Schrödinger equation in imaginary time. Both VMC and DMC work for systems at zero temperature, and mainly for the ground state, although obtaining some information of excited states is feasible. To study systems at finite temperature, one can use *Path Integral Monte Carlo* (PIMC), a method that uses the thermal density matrix and Feynman's path-integral formulation to obtain the system properties.

Since we want to study a quantum, 1D Bose gas at zero temperature, we focus exclusively on the VMC and DMC methods.

4.1. The Quantum Many-Body Problem

Let us consider a system of N quantum, interacting particles of mass m under the effect of an external potential, that interact between them through pairwise interaction potential. In the coordinate representation, the Hamiltonian

of this system is

$$\hat{H} = -\frac{\hbar^2}{2m}\sum_{i=1}^{N}\nabla_{\mathbf{r}_i}^2 + \sum_{i=1}^{N} V_{\text{ext}}(\mathbf{r}_i) + \sum_{i=1}^{N}\sum_{j=i+1}^{N} V_{\text{int}}(\mathbf{r}_i - \mathbf{r}_j), \qquad (4.1)$$

where $\mathbf{r}$ is the position of a single particle, and the indexes i and j label each one of them. The first term on the r.h.s of Eq. (4.1) is the total kinetic energy of the system; the second one accounts for the energy due to the external, trapping potential $V_{\text{ext}}(\mathbf{r})$ acting over the entire system; and the third one corresponds to the interaction energy of the system.

Now, suppose that we want to obtain the stationary states of the Schrödinger equation. We have to solve the equation

$$\hat{H}\Phi_n(\mathbf{R}) = E_n\Phi_n(\mathbf{R}) \qquad (4.2)$$

where $\Phi_n(\mathbf{R})$ and E_n are the eigenstate and eigenenergy, respectively, and $\mathbf{R} = \{\mathbf{r}_1, \mathbf{r}_2, \ldots, \mathbf{r}_N\}$ is the $3N$-dimensional vector with the positions of the particles. The first obstacle in this quest is immediate: obtaining exact solutions to Eq. (4.2) generally unrealizable. On the other hand, most of the time, we do not need all the solutions of Eq. (4.2), but the main goal is the study about the ground state and its properties, so one's effort can be focused on finding $\Phi_0(\mathbf{R}) = \langle \mathbf{R}|\Phi_0\rangle$. Therefore, some assumptions valid under specific conditions may be used, like in the case of the theory for weakly-interacting Bose gases and the Gross-Pitaevskii (Gross-Pitaevskii) equation, which has a special place in the research of dilute Bose gases. Another example is density functional theory (DFT) [115] for electronic systems, and more recently, for bosons [116, 117].

Knowing the ground state wave function of the system, we can obtain, in principle, the expected value of any observable $\hat{O}$:

$$\left\langle \hat{O}\right\rangle_{\Phi_0} = \frac{\langle\Phi_0|\hat{O}|\Phi_0\rangle}{\langle\Phi_0|\Phi_0\rangle}. \qquad (4.3)$$

The most common property is the ground state energy, i.e., the expected value of the Hamiltonian:

$$E_0 = \left\langle \hat{H}\right\rangle_{\Phi_0} = \frac{\langle\Phi_0|\hat{H}|\Phi_0\rangle}{\langle\Phi_0|\Phi_0\rangle}. \qquad (4.4)$$

Even for the ground state, solving Eq. (4.2) is a difficult task, although physicists have found analytic solutions for some specific systems in 1D geometries, like the Tonks-Girardeau gas [23], the Lieb-Liniger model [24], or the

Calogero model [25]. In addition to the necessary work to find the ground state $\Phi_0(\boldsymbol{R})$, there is an evident difficulty in evaluating the expected value Eq. (4.3), as it requires the evaluation of a multidimensional integral, which is not an easy task either. One may resort to numerical techniques to make the task doable; however, there is a trade-off between feasibility and ease of execution.

4.2. Monte Carlo Quadrature

Numerical evaluation of integrals in high dimensions is a hard problem. Standard methods for evaluating integrals based on cartesian products of one-dimensional quadrature rules suffer from the so-called *curse of dimensionality*, that is, the computing time required to evaluate an integral in a d-dimensional space (up to a required precision) grows exponentially with the dimension. A robust alternative consists of using stochastic integration techniques known as *Monte Carlo* quadratures, which depend on *quasi-random* numbers specially generated to approximate an integral through an arithmetic-mean. Compared to standard cartesian-product quadratures, stochastic methods may be less accurate for low-dimensional integrals. However, they have a remarkable (and valuable) property: their accuracy is independent of the dimension of the integrand. Accordingly, to integrate an arbitrary function, Monte Carlo methods show an accuracy of order $O(N^{-1/2})$, where N is the number of function evaluations used to approximate the integral. To improve the accuracy of an integral estimation by a factor of two, one has to evaluate the function four more times. Nevertheless, they do not suffer from any curse of dimensionality, and that is the reason why these are the most used methods to evaluate high dimensional integrals.

The description of the Monte Carlo quadrature method is closely related to the concept of expected value. Let us consider the function $f : \mathbb{R}^N \to \mathbb{R}$, and a *probability distribution function* (pdf), $g : \mathbb{R}^N \to \mathbb{R}$. The expected value of the function $f(\boldsymbol{R})$, where $\boldsymbol{R} \in \mathbb{R}^N$ is distributed according to $g(\boldsymbol{R})$, is given by the N-dimensional integral

$$\langle f \rangle = \int g(\boldsymbol{R}) f(\boldsymbol{R}) \, d\boldsymbol{R}. \tag{4.5}$$

The pdf $g(\boldsymbol{R})$ is a function that is nonnegative and satisfies the normalization condition,

$$1 = \int g(\boldsymbol{R}) \, d\boldsymbol{R}. \tag{4.6}$$

This type of integrals frequently appears in quantum mechanics as it is a common task to estimate expected values of operators that represent physical ob-

servables, the most important being the Hamiltonian $\hat{\boldsymbol{H}}$ since it corresponds to the energy of the system.

Let us consider a set sequence of M random points in the N dimensional space $\mathcal{S} = \{\boldsymbol{R}_1, \boldsymbol{R}_2, \dots, \boldsymbol{R}_M\}$ drawn from the pdf $g(\boldsymbol{R})$. We define the function $\overline{f}$ as the arithmetic mean of this collection,

$$\overline{f} = \frac{1}{M} \sum_{i=1}^{M} f(\boldsymbol{R}_i). \tag{4.7}$$

We should note that since the $\boldsymbol{R}_i$ points are random, the function $\overline{f}$ is a random function too. The basis of Monte Carlo integration is the *law of large numbers* [118],

$$\left\langle \overline{f} \right\rangle \underset{M \to \infty}{=} \langle f \rangle = \int g(\boldsymbol{R}) f(\boldsymbol{R}) d\boldsymbol{R}. \tag{4.8}$$

It states that the function $\overline{f}$ has the same mean as $f(\boldsymbol{R})$ when the number of random points M goes to infinity. The function $\overline{f}$ is called an *estimator* of $\langle f \rangle$, that is, a random number that fluctuates around the theoretical value $\langle f \rangle$ for different sequences of random points $\mathcal{S}$ [119]. Since it fluctuates, we can calculate the dispersion of the estimator, i.e., its variance:

$$\sigma_{\overline{f}}^2 = \left\langle \overline{f}^2 \right\rangle - \left\langle \overline{f} \right\rangle^2. \tag{4.9}$$

Analogously, the variance of $f(\boldsymbol{R})$ is

$$\sigma_f^2 = \left\langle f^2 \right\rangle - \langle f \rangle^2, \tag{4.10}$$

where the expected values $\langle f^2 \rangle$ and $\langle f \rangle$ are given by Eq. (4.5).

When the random variables $\boldsymbol{R}_i$ are all independent (which is not necessarily true in a Monte Carlo calculation), the variance of estimator $\overline{f}$ becomes

$$\sigma_{\overline{f}}^2 = \frac{1}{M} \sigma_f^2. \tag{4.11}$$

Equation (4.11) shows that the variance of the estimator $\overline{f}$ decreases as $1/N$. Then, as the number of random points $\boldsymbol{R}_i$ increases, the mean value of the estimator $\overline{f}$ becomes a better approximation to the mean value of $f(\boldsymbol{R})$. Both Eq. (4.8) and Eq. (4.11) are the main reasons of why Monte Carlo integration works, and why the error of the approximation of $\overline{f}$:

$$\epsilon_{\overline{f}} = \sqrt{\sigma_{\overline{f}}^2}, \tag{4.12}$$

decreases as $N^{-1/2}$ independently of the space dimension.

A major difficulty in evaluating Eq. (4.7) is drawing a sequence of points from the pdf $g(\boldsymbol{R})$. If $g(\boldsymbol{R})$ is a typical distribution, for instance: the normal or gaussian distribution, the binomial distribution, the Poisson distribution, among others, we can generate samples from them in a relatively easy way. However, this problem becomes a lot more complicated in quantum mechanics, because the distribution function that we use to calculate expected values of observables depends on the probability density of the many-body system, which is out of our hands for the most cases. Then, it is not clear how the Monte Carlo quadrature may be useful to accomplish our goals. In order to sample the target probability distribution $g(\boldsymbol{R})$, we employ a stochastic process known as *Markov chain*, which we describe in the following section.

4.3. Markov Processes

A Markov process is a stochastic process that represents the evolution of a random variable. It consists of a set of points (or states) commonly known as a Markov chain: $\{\boldsymbol{R}_1, \boldsymbol{R}_2, \ldots, \boldsymbol{R}_{j-1}, \boldsymbol{R}_j, \ldots, \boldsymbol{R}_M\}$ in the N-dimensional space with an associated transition probability $P(\boldsymbol{R}_\mathrm{f}|\boldsymbol{R}_\mathrm{i})$ of going from an initial state $\boldsymbol{R}_\mathrm{i} = \boldsymbol{R}_{j-1}$ to a final state $\boldsymbol{R}_\mathrm{f} = \boldsymbol{R}_j$, that is independent of the previous states, i.e., before $\boldsymbol{R}_{j-1}$. An evolving random configuration $\boldsymbol{R}$ it is commonly known as a *random walker*.

We want to sample the target distribution $g(\boldsymbol{R})$ through a Markov process, starting from an arbitrary initial distribution $g_\mathrm{ini}(\boldsymbol{R})$, e.g., a delta function at some arbitrary point: $g_\mathrm{ini}(\boldsymbol{R}) = \delta(\boldsymbol{R} - \boldsymbol{R}_0)$. The initial distribution should evolve to the target distribution by a repeated application of the transition probability. Therefore, the Markov process must be *ergodic*, i.e., it must be possible to move between any pair of states in a finite number of steps, so all states in the configuration space can be visited. Also, one imposes the *detailed balance condition*:

$$P(\boldsymbol{R}_\mathrm{f}|\boldsymbol{R}_\mathrm{i})\rho(\boldsymbol{R}_\mathrm{i}) = P(\boldsymbol{R}_\mathrm{i}|\boldsymbol{R}_\mathrm{f})\rho(\boldsymbol{R}_\mathrm{f}), \tag{4.13}$$

which forces the probability flux between the states $\boldsymbol{R}_\mathrm{i}$ and $\boldsymbol{R}_\mathrm{f}$ to be the same. Eq. (4.13) is a sufficient condition for $g(\boldsymbol{R})$ to be the target distribution [118, 120, 121].

The previous description of a Markov process leads to an obvious question: can we find a transition probability $P(\boldsymbol{R}_\mathrm{f}|\boldsymbol{R}_\mathrm{i})$, which gives rise to the target pdf $g(\boldsymbol{R})$? The answer to this question is yes, and we give some details about it in the following section.

4.3.1.   The Metropolis-Hastings Algorithm

Sampling from an arbitrary probability distribution function by direct methods is usually a difficult task. The Metropolis-Hastings (MH) algorithm, developed by Nicholas Metropolis et al. in 1953 [38] and later by W. K. Hastings in 1970 [122], is a widely recognized procedure to sample an arbitrary probability distribution in a relatively easy way. We can describe it as an iterative *accept-reject* method with a properly defined transition probability between two states. The repeated application of this probability over an initial distribution defines a Markov chain, which after a long enough number of iterations, gives rise to the target pdf $g(\boldsymbol{R})$. Also, it has a significant benefit: it is relatively simple to implement in a computer program.

The accept-reject procedure requires a probability to propose a movement from, $P_{\text{prop}}(\boldsymbol{R}'|\boldsymbol{R})$, which must be nonnegative and normalized to unity,

$$\int d\boldsymbol{R}' P_{\text{prop}}(\boldsymbol{R}'|\boldsymbol{R}) = 1. \tag{4.14}$$

A temporary point $\boldsymbol{R}'$ is drawn from this probability; it is accepted with a probability $P_{\text{acc}}(\boldsymbol{R}'|\boldsymbol{R})$ or rejected with probability $1 - P_{\text{acc}}(\boldsymbol{R}'|\boldsymbol{R})$. The transition probability is

$$P(\boldsymbol{R}'|\boldsymbol{R}) = \begin{cases} P_{\text{acc}}(\boldsymbol{R}'|\boldsymbol{R}) P_{\text{prop}}(\boldsymbol{R}'|\boldsymbol{R}) & \text{if} \quad \boldsymbol{R} \neq \boldsymbol{R} \\ 1 - \int d\boldsymbol{R}' \, P_{\text{acc}}(\boldsymbol{R}'|\boldsymbol{R}) P_{\text{prop}}(\boldsymbol{R}'|\boldsymbol{R}) & \text{if} \quad \boldsymbol{R}' = \boldsymbol{R} \end{cases}. \tag{4.15}$$

Finally, the acceptance probability is chosen such that $P(\boldsymbol{R}'|\boldsymbol{R})$ fulfills the detailed balance condition:

$$\frac{P_{\text{acc}}(\boldsymbol{R}'|\boldsymbol{R})}{P_{\text{acc}}(\boldsymbol{R}|\boldsymbol{R}')} = \frac{P_{\text{prop}}(\boldsymbol{R}|\boldsymbol{R}')g(\boldsymbol{R}')}{P_{\text{prop}}(\boldsymbol{R}'|\boldsymbol{R})g(\boldsymbol{R})}. \tag{4.16}$$

The acceptance probability, as chosen by Metropolis et al. [38], is

$$P_{\text{acc}}(\boldsymbol{R}'|\boldsymbol{R}) = \min\left\{1, \frac{P_{\text{prop}}(\boldsymbol{R}|\boldsymbol{R}')g(\boldsymbol{R}')}{P_{\text{prop}}(\boldsymbol{R}'|\boldsymbol{R})g(\boldsymbol{R})}\right\}. \tag{4.17}$$

We can make some observations about this formula:

- We do not have to normalize the target probability $g(\boldsymbol{R})$ in order to sample it since only the ratio $g(\boldsymbol{R}')/g(\boldsymbol{R})$ is needed.

- The proposal-of-movement probability $P_{\text{prop}}(\boldsymbol{R}'|\boldsymbol{R})$, although arbitrary, should be relatively easy to sample by direct methods so one can draw points $\boldsymbol{R}'$ from it.

- If the proposal probability is symmetric: $P_{\mathrm{prop}}(\boldsymbol{R'}|\boldsymbol{R}) = P_{\mathrm{prop}}(\boldsymbol{R}|\boldsymbol{R'})$, only the ratio $g(\boldsymbol{R'})/g(\boldsymbol{R})$ defines the acceptance probability.

A usual MH implementation (although not the only one) draws a a uniformly-distributed random state $\boldsymbol{R'}$ from a region in the N-dimensional space $\Omega_{\boldsymbol{R}}$ centered in the actual state $\boldsymbol{R}$:

$$P(\boldsymbol{R'}|\boldsymbol{R}) = \begin{cases} \frac{1}{\Delta^N} & \text{if} \quad \boldsymbol{R'} \in \Omega_{\boldsymbol{R}} \\ 0 & \text{if} \quad \boldsymbol{R'} \notin \Omega_{\boldsymbol{R}} \end{cases} \tag{4.18}$$

Then a new state $\boldsymbol{R'}$ is proposed following the formula

$$\boldsymbol{R'} = \boldsymbol{R} + \frac{\Delta}{2}\boldsymbol{U}_\xi, \tag{4.19}$$

where $\boldsymbol{U}_\xi$ is a vector with N random components in the interval $(-1, 1)$ drawn from a uniform distribution. The parameter Δ is the length of the side of a cube in the N-dimensional space centered around the current state $\boldsymbol{R}$ where the new state will be located. Since Eq. (4.18) is a symmetric probability, an iterative procedure using this proposal probability could be:

1. Let be $\boldsymbol{R} = \boldsymbol{R}_i$ the current state labeled by the index i.

2. Propose a new state $\boldsymbol{R'}$ according to Eq. (4.19).

3. Take the quotient $q_i = g(\boldsymbol{R'})/g(\boldsymbol{R}_i)$. Then

   - If $q_i \geq 1$, move to the new state: $\boldsymbol{R}_{i+1} = \boldsymbol{R'}$.

   - If $q_i < 1$, take a random number ξ_i from a uniform distribution in $[0, 1)$. If $q_i > \xi_i$ move to the new state: $\boldsymbol{R}_{i+1} = \boldsymbol{R'}$, otherwise stay in the same state: $\boldsymbol{R}_{i+1} = \boldsymbol{R}_i$.

   In both cases, define the acceptance probability according to Eq. (4.17).

After applying this procedure a large enough number of times, the Markov chain will sample the target distribution $g(\boldsymbol{R})$. The period during which the initial distribution evolves to the target one is known as *equilibration*. It also is known as the *burn-in* or *thermalization* phase. Generally, it is assumed that the states that belong to this phase do not sample the target distribution; in practice, they are discarded from the Markov chain and never used to evaluate any estimator.

4.3.2. Reblocking Analysis and Correlation Time

The MH algorithm is a robust procedure to generate a sample of points that follows the pdf $g(\boldsymbol{R})$, so it is possible to obtain an approximation to an expected value through the estimator Eq. (4.7), as well as an approximation of the error from Eq. (4.12). However, one must note that the samples generated by the MH algorithm are always serially correlated. Therefore, Eq. (4.12) must take into account this correlation; otherwise, the value it yields will become an unreliable approximation to the error of the estimator that can severely underestimate the real error. There are several methods to quantify the correlation of serially generated data, for instance: calculation of correlation times, *reblocking analysis*, or the Jackknife analysis [119]. We focus on the reblocking technique, also called *binning analysis*, due to its relative simplicity.

The reblocking technique consists in dividing an initial set of measurements $\{\mathcal{O}_n \mid n = 1, 2, \ldots, N\}$, N being the length of the set, in contiguous subgroups with b data elements called *blocks* or *bins*. This splitting creates a new data series with N_b elements such that $N = N_\mathrm{b} b$. For each block, we calculate its mean (the block average):

$$\mathcal{O}_{\mathrm{B},n} = \frac{1}{b} \sum_{i=1}^{b} \mathcal{O}_{(n-1)b+i}, \quad n = 1, 2, \ldots, N_\mathrm{b} \tag{4.20}$$

so effectively $\mathcal{O}_{\mathrm{B},n}$ becomes the n-th element of the new time series. One can prove that the mean of this series, i.e.,

$$\overline{\mathcal{O}_\mathrm{B}} = \frac{1}{N_\mathrm{b}} \sum_{n=1}^{N_\mathrm{b}} \mathcal{O}_{\mathrm{B},n} \tag{4.21}$$

is equal to the mean of the original series,

$$\overline{\mathcal{O}} = \frac{1}{N} \sum_{n=1}^{N} \mathcal{O}_n. \tag{4.22}$$

However, the new series variance is different from the original series variance. As the size of the block increases, one finds that the variance keeps increasing until it reaches a top value. When this occurs, the block size is large enough that we can think of every block to be practically uncorrelated from each other.

The block size at which the variance of the estimator Eq. (4.7) reaches a maximum can be related to the *autocorrelation time* of the data series. Starting from the definition of the estimator variance Eq. (4.9), we obtain

$$\sigma_{\overline{\mathcal{O}}}^2 = \frac{1}{N^2} \sum_{i,j=1}^{N} \left[\langle \mathcal{O}_i \mathcal{O}_j \rangle - \langle \mathcal{O}_i \rangle \langle \mathcal{O}_j \rangle \right]. \tag{4.23}$$

This expression can be rewritten as a term that includes diagonal measurements, plus a term from the nondiagonal ones,

$$\sigma_{\overline{\mathcal{O}}}^2 = \frac{1}{N^2} \sum_{i=1}^N \left[\left\langle \mathcal{O}_i^2 \right\rangle - \langle \mathcal{O}_i \rangle^2 \right] + \frac{1}{N^2} \sum_{\substack{i,j=1 \\ i \neq j}}^N \left[\langle \mathcal{O}_i \mathcal{O}_j \rangle - \langle \mathcal{O}_i \rangle \langle \mathcal{O}_j \rangle \right]. \quad (4.24)$$

The first term in the r.h.s. can be identified as the variance of the original data measurements $\sigma_{\mathcal{O}_i}^2$ times $1/N$. Also, it is the variance of the estimator as if the measurements were serially uncorrelated. The second term accounts for the serial correlations. Factoring $\sigma_{\mathcal{O}_i}^2$, we obtain a compact formula for the estimator variance,

$$\sigma_{\overline{\mathcal{O}}}^2 = \frac{\sigma_{\mathcal{O}_i}^2}{N} 2\tau_{\mathcal{O}}, \quad (4.25)$$

where $\tau_{\mathcal{O}}$ is the *integrated autocorrelation time* of the data series,

$$\tau_{\mathcal{O}} = \frac{1}{2} + \sum_{k=1}^N A(k) \left(1 - \frac{k}{N} \right), \quad (4.26)$$

with

$$A(k) = \frac{\langle \mathcal{O}_i \mathcal{O}_{i+k} \rangle - \langle \mathcal{O}_i \rangle \langle \mathcal{O}_{i+k} \rangle}{\langle \mathcal{O}_i^2 \rangle - \langle \mathcal{O}_i \rangle^2}, \quad (4.27)$$

where $A(0) = 1$.

Equation (4.25) shows that the variance of the autocorrelated measurements is greater than the variance of the independent measurements by a factor of $2\tau_{\mathcal{O}}$. This is equivalent to say that the original data series has an effective number of elements $N_{\text{eff}} = N/2\tau_{\mathcal{O}} \leq N$, and the estimator variance is equal to the variance of the uncorrelated data divided by N_{eff}:

$$\sigma_{\overline{\mathcal{O}}}^2 = \frac{\sigma_{\mathcal{O}_i}^2}{N_{\text{eff}}}. \quad (4.28)$$

Furthermore, the statistical error $\epsilon_{\overline{\mathcal{O}}}$ of the estimator $\overline{\mathcal{O}}$ becomes

$$\epsilon_{\overline{\mathcal{O}}} = \sqrt{\frac{\sigma_{\mathcal{O}_i}^2}{N_{\text{eff}}}}. \quad (4.29)$$

This result shows that, even when we take into account the correlations, the statistical error of the estimator decreases as $N_{\text{eff}}^{-1/2}$, like in the uncorrelated case.

An additional, important remark: to avoid an underestimation of the true variance of the measurements, one should use the *unbiased*, or *bias-corrected*, variance formula [119]:

$$\sigma_{\mathcal{O}_i}^2 = \frac{1}{N-1} \sum_{i=1}^{N} (\mathcal{O}_i - \overline{\mathcal{O}})^2. \tag{4.30}$$

To conclude this section, we note that the correlation degree of the measurements forming a Markov chain will depend on the characteristics of the proposal probability distribution we use to draw random points. How large the correlation time becomes will depend, mainly, on the size of the random movements. Small movements will lead to a high correlation between points, and to a high *acceptance rate* (the proportion of movements that are accepted during the MH procedure). On the other hand, large movements result in lower correlations, but with a lower acceptance rate.

Finally, there are several factors to take into account when sampling the target pdf $g(\boldsymbol{R})$. For instance, there is a discussion about which is the optimum acceptance rate. A Monte Carlo calculation with large movements but a shallow acceptance rate will not cover the entire configuration space. Instead, it will sample only a relatively small region. Hence, the generated Markov chain will not reliably sample the target distribution. In comparison, a Monte Carlo calculation with small movements but a high acceptance rate implies a high correlation between samples, and it will require a very long Markov chain to cover the largest area of the configuration space as possible. Traditionally, a Monte Carlo calculation aiming at an acceptance rate of 50% is a *rule of thumb*: the best compromise between data correlations and a satisfactory exploration of the configuration space. However, there is no particular reason for saying that the 50% rule is the optimal one.

A broader discussion about data correlations and error estimations can be read in [119].

4.4. Variational Monte Carlo Method

Variational Monte Carlo (VMC) method is a Monte Carlo variant used to calculate an approximation to the ground state energy of a quantum system at zero temperature based on the variational principle of quantum mechanics. This principle states that the expected value of the Hamiltonian $\hat{H}$ over an arbitrary state $|\Psi_\mathrm{T}\rangle$ that has a nonzero overlap with the ground state $|\Phi_0\rangle$ of $\hat{H}$, i.e.,

$\langle \Psi_T | \Phi_0 \rangle \neq 0$, is an upper bound of the energy of the ground state,

$$E = \frac{\langle \Psi_T | \hat{H} | \Psi_T \rangle}{\langle \Psi_T | \Psi_T \rangle} \geq E_0. \tag{4.31}$$

The trial wave functions $\Psi_T(\boldsymbol{R}) = \langle \boldsymbol{R} | \Psi_T \rangle$ depend on one or more variational parameters whose optimum values are those that minimize the energy Eq. (4.31).

In the position representation, the wave function of N particles depends on the positions of all of the particles: $\boldsymbol{R} = \{\boldsymbol{r}_1, \boldsymbol{r}_2, \ldots, \boldsymbol{r}_N\}$. Then, the expected value Eq. (4.31) becomes

$$E = \frac{\displaystyle\int d\boldsymbol{R}\; \Psi_T^*(\boldsymbol{R})\hat{H}\,\Psi_T(\boldsymbol{R})}{\displaystyle\int d\boldsymbol{R}\; \Psi_T^*(\boldsymbol{R})\Psi_T(\boldsymbol{R})}. \tag{4.32}$$

To calculate the energy, we have to evaluate two $3N$-dimensional integrals. However, the integrals in Eq. (4.32) (and other expected values of similar structure that we will see later) can be rearranged in such a way that we can calculate the energy using Monte Carlo integration. First, we must write the expected value of the Hamiltonian as an integral of the form Eq. (4.5), which is not particularly difficult: we define the pdf

$$g(\boldsymbol{R}) = \frac{|\Psi_T(\boldsymbol{R})|^2}{\displaystyle\int d\boldsymbol{R}\; |\Psi_T(\boldsymbol{R})|^2}, \tag{4.33}$$

and the local energy

$$E_L(\boldsymbol{R}) = \frac{1}{\Psi_T(\boldsymbol{R})}\hat{H}\,\Psi_T(\boldsymbol{R}). \tag{4.34}$$

Then the expected value of $\hat{H}$ becomes

$$E = \int d\boldsymbol{R}\; g(\boldsymbol{R})E_L(\boldsymbol{R}). \tag{4.35}$$

Besides the evaluation of the expected value of the energy, VMC calculations involve the minimization of Eq. (4.35). We achieve this by adjusting the variational parameters of the wave function. We will approach this subject with more detail in Section 4.6.

Other observables can be approximated by the VMC method too. In these cases, the expected value

$$\left\langle \hat{O} \right\rangle_{\text{var}} = \frac{\int d\boldsymbol{R} \ \Psi_{\text{T}}^*(\boldsymbol{R}) \hat{O} \ \Psi_{\text{T}}(\boldsymbol{R})}{\int d\boldsymbol{R} \ \Psi_{\text{T}}^*(\boldsymbol{R}) \Psi_{\text{T}}(\boldsymbol{R})}. \tag{4.36}$$

is referred to as the *variational estimator* of $\hat{O}$. This estimator can be written as

$$\mathcal{O} = \int d\boldsymbol{R} \ g(\boldsymbol{R}) \mathcal{O}_{\text{L}}(\boldsymbol{R}), \tag{4.37}$$

where $\mathcal{O}$ is the "local observable"

$$\mathcal{O}_{\text{L}}(\boldsymbol{R}) = \frac{1}{\Psi_{\text{T}}(\boldsymbol{R})} \hat{O} \ \Psi_{\text{T}}(\boldsymbol{R}). \tag{4.38}$$

4.4.1. Stochastic Realization

To realize a VMC calculation, we start with a random point $\boldsymbol{R}_1$ drawn from an arbitrary probability distribution, although a point generated in a regular pattern is equally valid. Whichever the choice is, the positions $\{\boldsymbol{r}_1, \boldsymbol{r}_2, \ldots, \boldsymbol{r}_N\}$ of the N particles should cover the largest available volume of the system in question. This initial point represents the initial distribution

$$g_{\text{ini}}(\boldsymbol{R}) = \delta(\boldsymbol{R} - \boldsymbol{R}_1). \tag{4.39}$$

Having $g_{\text{ini}}(\boldsymbol{R})$, we use the Metropolis-Hasting algorithm to sample the next $\boldsymbol{R}_2$ element of the chain that will eventually converge to the target distribution. This point may be equal to $\boldsymbol{R}_1$, according to the accept-reject procedure of a MH step. This procedure is repeated to generate the next point $\boldsymbol{R}_3$, then $\boldsymbol{R}_4$, and as many points as required. After a large enough number of steps, and after dropping the first M_{burn} steps that form the burn-in phase, the resulting Markov chain $\mathcal{S} = \{\boldsymbol{R}_1, \boldsymbol{R}_2, \ldots, \boldsymbol{R}_{M-1}, \boldsymbol{R}_M\}$ with M samples will have converged to the target distribution Eq. (4.33). Then, following Eq. (4.7) and Eq. (4.35), the expected value of the Hamiltonian on the state $\Psi_{\text{T}}(\boldsymbol{R})$ is given by the estimator

$$\overline{E} = \frac{1}{M} \sum_{i=1}^{M} E_{\text{L}}(\boldsymbol{R}_i). \tag{4.40}$$

One can calculate the statistical error of Eq. (4.40) according to Eq. (4.29):

$$\epsilon_{\overline{E}} = \sqrt{\frac{\sigma_{E_i}^2}{N_{\text{eff}}}}, \tag{4.41}$$

where $\sigma_{E_i}^2$ should be the unbiased variance of the set $\{E_i\}_{i=1,...,M}$, being $E_i = E_{\mathrm{L}}(\boldsymbol{R}_i)$:

$$\sigma_{E_i}^2 = \frac{1}{M-1} \sum_{i=1}^{M} \left(E_i - \overline{E}\right)^2. \tag{4.42}$$

Also, one can calculate the number of effective samples $N_{\mathrm{eff}} = M/2\tau_{E_i}$ by a reblocking analysis, as outlined in Section 4.3.2.

4.5. Diffusion Monte Carlo Method

In VMC, the accuracy of the approximation Eq. (4.32) and its statistical error, are limited by choice of the trial wave function $\Psi_{\mathrm{T}}(\boldsymbol{R})$. This limitation can be overcome with the use of one of the so-called *Projector Monte Carlo* techniques [123]. The method we use in this work is the *Diffusion Monte Carlo* (DMC) method.

The basis of the DMC method is the time-dependent, "shifted" many-body Schrödinger equation:

$$
\begin{aligned}
i\hbar \frac{\partial \Psi(\boldsymbol{R}, t)}{\partial t} &= \left(\hat{\boldsymbol{H}} - E_{\mathrm{T}}\right) \Psi(\boldsymbol{R}, t) \\
&= \left(-\frac{\hbar^2}{2m} \nabla_{\boldsymbol{R}}^2 + V(\boldsymbol{R}) - E_{\mathrm{T}}\right) \Psi(\boldsymbol{R}, t).
\end{aligned}
\tag{4.43}
$$

Here, $\Psi(\boldsymbol{R}, \tau)$ is the state of the system as a function of the positions of the particles and the time, $\hat{\boldsymbol{H}}$ is the many-body Hamiltonian Eq. (4.1)

$$\nabla_{\boldsymbol{R}}^2 = \sum_{i=1}^{N} \nabla_{\boldsymbol{r}_i}^2, \quad V(\boldsymbol{R}) = \sum_{i=1}^{N} V_{\mathrm{ext}}(\boldsymbol{r}_i) + \sum_{i=1}^{N} \sum_{j=i+1}^{N} V_{\mathrm{int}}(\boldsymbol{r}_i, \boldsymbol{r}_j), \tag{4.44}$$

and E_{T} is an energy shift which should be as close as possible to the exact ground state energy.

The DMC method solves the Schrödinger equation in imaginary time, i.e., for $\tau = it/\hbar$:

$$
\begin{aligned}
-\frac{\partial \Psi(\boldsymbol{R}, \tau)}{\partial \tau} &= \left(\hat{\boldsymbol{H}} - E_{\mathrm{T}}\right) \Psi(\boldsymbol{R}, \tau) \\
&= \left(-D\nabla_{\boldsymbol{R}}^2 + V(\boldsymbol{R}) - E_{\mathrm{T}}\right) \Psi(\boldsymbol{R}, \tau),
\end{aligned}
\tag{4.45}
$$

where $D = \hbar^2/2m$. The units of τ are inverse of energy. We can identify Eq. (4.45) as a modified diffusion equation in the $3N$-dimensional space. If

the term $V(\boldsymbol{R}) - E_{\mathrm{T}}$ is removed, it becomes the common diffusion equation with a diffusion constant D. On the other hand, if the term with the Laplacian is removed, the equation would represent an exponential growth or decrease of the function $\Psi(\boldsymbol{R}, \tau)$.

Solving Eq. (4.45) represents a way to access the ground state of the system. The wave function $\Psi(\boldsymbol{R}, \tau)$ can be expanded as a linear combination of the Hamiltonian eigenstates $\{\Phi_n(\boldsymbol{R})\}$ (see Eq. (4.2)):

$$\Psi(\boldsymbol{R}, \tau) = \sum_{n=0}^{\infty} c_n \, e^{-(E_n - E_{\mathrm{T}})\tau} \Phi_n(\boldsymbol{R}). \tag{4.46}$$

Here, $\{E_n\}$ are the Hamiltonian eigenenergies. While the amplitudes of each one of the terms in Eq. (4.46) may increase or decrease in time depending on the value of E_{T}, for long times τ, the term proportional to $e^{-(E_0 - E_{\mathrm{T}})\tau}$ dominates the sum. Then, the wave function becomes

$$\Psi(\boldsymbol{R}, \tau) \underset{\tau \to \infty}{=} c_0 \, e^{-(E_0 - E_{\mathrm{T}})\tau} \Phi_0(\boldsymbol{R}) \tag{4.47}$$

The DMC technique evolves, in a stochastic fashion, an initial, arbitrary (up to some degree) many-body state $\Psi(\boldsymbol{R}, \tau = 0)$ in imaginary time, until a sufficiently long time passes and only the ground state contributes with a substantial weight to the many-body wave function according to Eq. (4.47). During the stochastic realization, the energy shift E_{T} is continuously adjusted until it becomes practically equal to the exact ground state energy E_0 (up to a statistical error).

A solution of Eq. (4.45) corresponds to the imaginary-time evolution of the state $|\Psi(\tau)\rangle$:

$$|\Psi(\tau)\rangle = \hat{\boldsymbol{U}}(\tau) |\Psi(\tau = 0)\rangle, \quad \hat{\boldsymbol{U}}(\tau) = e^{-(\hat{\boldsymbol{H}} - E_{\mathrm{T}})\tau}, \tag{4.48}$$

where $\hat{\boldsymbol{U}}(\tau)$ is the "shifted" evolution operator. The projection of $|\Psi(\tau)\rangle$ in the position space: $\Psi(\boldsymbol{R}, \tau) = \langle \boldsymbol{R} | \Psi(\tau) \rangle$, results in the formal solution of Eq. (4.45):

$$\Psi(\boldsymbol{R}, \tau) = \int d\boldsymbol{R}' \, G(\boldsymbol{R}, \boldsymbol{R}'; \tau) \Psi(\boldsymbol{R}', 0), \tag{4.49}$$

being $\Psi(\boldsymbol{R}, 0)$ the wave function at the initial time, and $G(\boldsymbol{R}, \boldsymbol{R}'; \tau)$ the Green's function of Eq. (4.45) (also known as the imaginary-time propagator):

$$G(\boldsymbol{R}, \boldsymbol{R}'; \tau) = \langle \boldsymbol{R} | \, e^{-(\hat{\boldsymbol{H}} - E_{\mathrm{T}})\tau} \, | \boldsymbol{R}' \rangle, \tag{4.50}$$

subject to the initial-type boundary condition $G(\boldsymbol{R}, \boldsymbol{R}'; 0) = \delta(\boldsymbol{R}' - \boldsymbol{R})$.

In general, we can not calculate the many-body Green's function Eq. (4.50) for all times τ. However, the imaginary-time evolution can be applied repeatedly, in a step-by-step process, according to

$$|\Psi(\tau + \delta\tau)\rangle = \hat{\boldsymbol{U}}(\delta\tau)\,|\Psi(\tau)\rangle\,, \quad \hat{\boldsymbol{U}}(\delta\tau) = e^{-(\hat{\boldsymbol{H}} - E_{\mathrm{T}})\delta\tau}, \tag{4.51}$$

where $\delta\tau$ is the size of the imaginary time-step. Analogously to Eq. (4.49), projecting in the position space one obtains

$$\Psi(\boldsymbol{R}, \tau + \delta\tau) = \int d\boldsymbol{R}'\, G(\boldsymbol{R}, \boldsymbol{R}'; \delta\tau)\Psi(\boldsymbol{R}', \tau). \tag{4.52}$$

The DMC method requires the repeated application of the evolution operator Eq. (4.51) since the many-body Green's function is known analytically only in the short-time limit when $\delta\tau$ is small. Let be $\delta\tau = \tau/M$, where M is a large integer, then an approximation to the final state Eq. (4.48) is obtained by applying M times the short-time evolution operator $\hat{\boldsymbol{U}}(\delta\tau)$ over the initial state $|\Psi(\tau = 0)\rangle$.

4.5.1. Short-Time Green's Function

Using the Trotter formula [124], we can obtain an approximation of the evolution operator in the short-time limit up to terms of order $O(\delta\tau^2)$. Since $\hat{\boldsymbol{H}} - E_{\mathrm{T}} = \hat{\boldsymbol{T}} + \hat{\boldsymbol{V}} - E_{\mathrm{T}}$,

$$\hat{\boldsymbol{U}}(\delta\tau) = e^{-(\hat{\boldsymbol{T}} + \hat{\boldsymbol{V}})\delta\tau}e^{E_{\mathrm{T}}\delta\tau} \approx e^{-\hat{\boldsymbol{V}}\delta\tau/2}e^{-\hat{\boldsymbol{T}}\delta\tau}e^{-\hat{\boldsymbol{V}}\delta\tau/2}e^{E_{\mathrm{T}}\delta\tau} + O(\delta\tau^2). \tag{4.53}$$

With this approximation, the Green's function Eq. (4.50) becomes

$$G(\boldsymbol{R}, \boldsymbol{R}'; \delta\tau) = (4\pi D\delta\tau)^{-3N/2}e^{-\frac{\|\boldsymbol{R} - \boldsymbol{R}'\|^2}{4D\delta\tau}} \times e^{-\left(\frac{V(\boldsymbol{R}) + V(\boldsymbol{R}')}{2} - E_{\mathrm{T}}\right)\delta\tau}, \tag{4.54}$$

which can be written as the product of a diffusion term:

$$P_{\mathrm{diff}}(\boldsymbol{R}, \boldsymbol{R}'; \delta\tau) = (4\pi D\delta\tau)^{-3N/2}e^{-\frac{\|\boldsymbol{R} - \boldsymbol{R}'\|^2}{4D\delta\tau}}, \tag{4.55}$$

times a rate term:

$$W(\boldsymbol{R}, \boldsymbol{R}'; \delta\tau) = e^{-\left(\frac{V(\boldsymbol{R}) + V(\boldsymbol{R}')}{2} - E_{\mathrm{T}}\right)\delta\tau}. \tag{4.56}$$

Then, the Green's function Eq. (4.54) becomes:

$$G(\boldsymbol{R}, \boldsymbol{R}'; \delta\tau) = P_{\mathrm{diff}}(\boldsymbol{R}, \boldsymbol{R}'; \delta\tau)W(\boldsymbol{R}, \boldsymbol{R}'; \delta\tau), \tag{4.57}$$

and solution Eq. (4.52) can be written as

$$\Psi(\boldsymbol{R}, \tau + \delta\tau) = \int d\boldsymbol{R}' \, P_{\text{diff}}(\boldsymbol{R}, \boldsymbol{R}'; \delta\tau) W(\boldsymbol{R}, \boldsymbol{R}'; \delta\tau) \Psi(\boldsymbol{R}', \tau). \quad (4.58)$$

In principle, Eq. (4.58) suggests how to realize a DMC calculation: evolve $\Psi(\boldsymbol{R}, \tau)$ through a procedure which can be depicted as a stochastic Gaussian diffusion of N particles following the probability distribution Eq. (4.55), with a corresponding weight given by the term Eq. (4.56). However, this is valid only if we interpret $\Psi(\boldsymbol{R}, \tau)$ as a probability, so it should be positive everywhere. An additional difficulty comes from the presence of the potential $V(\boldsymbol{R})$ in the weight term: if the potential diverges when two particles are very close, then the weight associated with the N particles will diverge too. This problem leads to stability problems during the realization.

A more efficient way to deal with the previous problems is to introduce *importance sampling*, by employing a proper trial wave function to approximate the real ground state, as we did for VMC calculations.

4.5.2. Importance-Sampling

In DMC, the ground state expected value of an observable $\hat{\boldsymbol{O}}$ is obtained from

$$\left\langle \hat{\boldsymbol{O}} \right\rangle_{\text{mix}} = \frac{\langle \Psi_{\text{T}} | \hat{\boldsymbol{O}} | \Psi(\tau \to \infty) \rangle}{\langle \Psi_{\text{T}} | \Psi(\tau \to \infty) \rangle}, \quad (4.59)$$

where $\Psi(\boldsymbol{R}, \tau)$ is the solution of Eq. (4.45) whose time-evolution is fixed by Eq. (4.52), and $\Psi_{\text{T}}(\boldsymbol{R})$ is a known trial wave function. The expected value Eq. (4.59) is referred to as a *mixed estimator* since it is evaluated over two different states. Then, the ground state energy E_0 of the system is the mixed estimator of $\hat{\boldsymbol{H}}$:

$$E_0 = \left\langle \hat{\boldsymbol{H}} \right\rangle_{\text{mix}} = \frac{\langle \Psi_{\text{T}} | \hat{\boldsymbol{H}} | \Psi(\tau \to \infty) \rangle}{\langle \Psi_{\text{T}} | \Psi(\tau \to \infty) \rangle}. \quad (4.60)$$

In the position representation, this expression becomes

$$E_0 = \frac{\displaystyle\int d\boldsymbol{R} \, \Psi_{\text{T}}^*(\boldsymbol{R}) \hat{\boldsymbol{H}} \Psi(\boldsymbol{R}, \tau \to \infty)}{\displaystyle\int d\boldsymbol{R} \, \Psi_{\text{T}}^*(\boldsymbol{R}) \Psi(\boldsymbol{R}, \tau \to \infty)}. \quad (4.61)$$

Unless a complex trial wave function becomes a requirement, for instance, when imposing *twisted boundary conditions* on $\Psi_{\text{T}}(\boldsymbol{R})$ [125], one works with

real wave functions only. Then, the complex conjugation $\Psi_{\mathrm{T}}^*(\boldsymbol{R})$ in Eq. (4.61) becomes unnecessary. By applying similar algebraic transformations as we did for the expected value Eq. (4.35), we obtain the following equivalent expression for E_0:

$$E_0 = \frac{\displaystyle\int d\boldsymbol{R}\ f(\boldsymbol{R},\tau\to\infty)E_{\mathrm{L}}(\boldsymbol{R})}{\displaystyle\int d\boldsymbol{R}\ f(\boldsymbol{R},\tau\to\infty)}, \tag{4.62}$$

where we have defined the *mixed distribution* as

$$f(\boldsymbol{R},\tau) = \Psi_{\mathrm{T}}(\boldsymbol{R})\Psi(\boldsymbol{R},\tau). \tag{4.63}$$

At the same time, the local energy is given by Eq. (4.34).

To calculate the ground state energy, we need a method to sample the mixed distribution $f(\boldsymbol{R},\tau)$ in the limit $\tau\to\infty$. The time evolution of $f(\boldsymbol{R},\tau)$ can be obtained by multiplying Eq. (4.45) by $\Psi_{\mathrm{T}}(\boldsymbol{R})$. After using some vectorial identities, one obtains

$$-\frac{\partial f(\boldsymbol{R},\tau)}{\partial\tau} = -D\nabla_{\boldsymbol{R}}^2 f(\boldsymbol{R},t) + D\nabla\cdot[f(\boldsymbol{R},\tau)\boldsymbol{F}(\boldsymbol{R})]$$
$$+ \left(E_{\mathrm{L}}(\boldsymbol{R}) - E_{\mathrm{T}}\right)f(\boldsymbol{R},t). \tag{4.64}$$

Here, the quantity

$$\boldsymbol{F}(\boldsymbol{R}) = 2\frac{\nabla\Psi_{\mathrm{T}}(\boldsymbol{R})}{\Psi_{\mathrm{T}}(\boldsymbol{R})} = \nabla_{\boldsymbol{R}}\ln|\Psi_{\mathrm{T}}(\boldsymbol{R})|^2 \tag{4.65}$$

is called the *drift force* or sometimes *drift velocity*.

Equation (4.64) describes a (modified) diffusion process for the mixed probability distribution $f(\boldsymbol{R},\tau)$. It contains a rate term proportional to the difference $E_{\mathrm{L}}(\boldsymbol{R}) - E_{\mathrm{T}}$, unlike the rate term in Eq. (4.45) that depends on the potential $V(\boldsymbol{R})$. With a suitable choice of $\Psi_{\mathrm{T}}(\boldsymbol{R})$, the local energy remains finite, unlike the potential. Furthermore, as the trial wave function gets improved, the so-called *excess energy* [126] approaches to the ground state energy E_0, and the rate term vanishes, which is favorable to the calculations. The most notable difference concerning Eq. (4.45) is the additional term $\nabla\cdot[f(\boldsymbol{R},\tau)\boldsymbol{F}(\boldsymbol{R})]$, which imposes a drift on the diffusion process that depends on the trial wave function.

In the large time limit, the mixed distribution becomes proportional to the ground state wave function

$$f(\boldsymbol{R},\tau)\underset{\tau\to\infty}{=} c_0\,e^{-(E_0-E_{\mathrm{T}})\tau}\Psi_{\mathrm{T}}(\boldsymbol{R})\Phi_0(\boldsymbol{R}). \tag{4.66}$$

4.5.3. Importance-Sampling Green's Function

The formal solution of Eq. (4.64) is

$$f(\boldsymbol{R}, \tau + \delta\tau) = \int d\boldsymbol{R}' \; \tilde{G}(\boldsymbol{R}, \boldsymbol{R}'; \delta\tau) f(\boldsymbol{R}', \tau). \tag{4.67}$$

Here, $\tilde{G}(\boldsymbol{R}, \boldsymbol{R}'; \delta\tau)$ is the *importance-sampling Green's function*, which is a solution of Eq. (4.64) with boundary condition

$$\tilde{G}(\boldsymbol{R}, \boldsymbol{R}'; 0) = \delta(\boldsymbol{R}' - \boldsymbol{R}) \tag{4.68}$$

Using the Trotter formula, the analytical expression in the short time approximation for the Green's function of Eq. (4.64) is expressed as

$$\tilde{G}(\boldsymbol{R}, \boldsymbol{R}'; \delta\tau) = \tilde{P}_{\text{diff}}(\boldsymbol{R}, \boldsymbol{R}'; \delta\tau)\tilde{W}(\boldsymbol{R}, \boldsymbol{R}'; \delta\tau), \tag{4.69}$$

where

$$\tilde{P}_{\text{diff}}(\boldsymbol{R}, \boldsymbol{R}'; \delta\tau) = (4\pi D\delta\tau)^{-3N/2} e^{-\frac{\|\boldsymbol{R} - \boldsymbol{R}' - D\delta\tau \boldsymbol{F}(\boldsymbol{R}')\|^2}{4D\delta\tau}} \tag{4.70}$$

and

$$\tilde{W}(\boldsymbol{R}, \boldsymbol{R}'; \delta\tau) = e^{-\left(\frac{E_{\text{L}}(\boldsymbol{R}) + E_{\text{L}}(\boldsymbol{R}')}{2} - E_{\text{T}}\right)\delta\tau}. \tag{4.71}$$

Importance-sampling Green's function Eq. (4.69) meaning is clear: Eq. (4.70) represents an isotropic diffusion process followed by a drift, with a corresponding weight Eq. (4.70) that depends on the local energy instead of the potential.

4.5.4. Stochastic Realization

A practical implementation of DMC always uses importance sampling. The stochastic realization of a single time-step follows Eq. (4.67): it corresponds to a weighed, isotropic, Gaussian diffusion process where all of the particles are subject to a drift force. Compared to a VMC calculation, it is more complex to implement.

Initialization

We start at an initial distribution $f_{\text{ini}}(\boldsymbol{R}, 0)$, which can be a random configuration $\boldsymbol{R}_1$ drawn from an arbitrary probability distribution. More commonly,

to start with a better distribution, a VMC calculation precedes the DMC realization. Then, the initial configuration is drawn from the VMC distribution Eq. (4.33),

$$f_{\text{ini}}(\boldsymbol{R}) = f(\boldsymbol{R}, 0) = |\Psi_{\text{T}}(\boldsymbol{R})|^2, \tag{4.72}$$

after a long enough number of Metropolis-Hastings steps.

Several methods exist to take into account the effect of the weight term, the more common being the *branch-and-death with variable population* sampling variant [126]. In this variant, at each time step, we will track the configurations of a set of random walkers:

$$\mathcal{R}_k = \{\boldsymbol{R}_{k,\alpha} \mid \alpha = 1, 2, \ldots, N_{\text{w},k}\}. \tag{4.73}$$

Here, k is the time step index, $\tau_k = k\delta\tau$ is the current time, and $N_{\text{w},k}$ is the number of random walkers which may change between steps. At all times, the walkers will have a unit weight: $w_{k,\alpha} = 1$, for $k = 1, 2, \ldots, M$, being M the number of time steps of the DMC calculation. Also, the energy shift $E_{\text{T},k}$ can change between steps, as well as the energy estimator $\overline{E}_{0,k}$ (see Eq. (4.78)). The full stochastic realization is described as follows:

At time-step $k = 0$, we start with a set of $N_{\text{w},0}$ random walkers $\mathcal{R}_0$. The number of walkers is somewhat arbitrary, but it could be of the order of one hundred. These walkers can be drawn from the probability distribution Eq. (4.72); although it is not mandatory, it helps to speed up the calculation. Since an initial estimate for E_{T} is needed, we can use the mean of the local energies of the walkers,

$$E_{\text{T},0} = \frac{1}{N} \sum_{\alpha=1}^{N_{\text{w},0}} E_{\text{L}}(\boldsymbol{R}_{0,\alpha}). \tag{4.74}$$

The subindex "0" in the energy shift E_{T} indicates that it changes between steps in the main procedure.

Main Procedure

The following procedure corresponds to time steps $1, 2, \ldots, M$.

1. For each random walker in $\mathcal{R}_{k-1}$, draw a new configuration from the distribution $\tilde{P}_{\text{diff}}(\boldsymbol{R}, \boldsymbol{R}'; \delta\tau)$ according to Eq. (4.70). We achieve this by proposing the following random move:

$$\boldsymbol{R}_{k,\alpha} = \boldsymbol{R}_{k-1,\alpha} + D\delta\tau \boldsymbol{F}(\boldsymbol{R}_{k-1,\alpha}) + \boldsymbol{\chi}, \tag{4.75}$$

where χ is a random configuration in the N-dimensional space drawn from the multivariate Gaussian distribution with zero mean and variance $\sigma^2 = 2D\delta\tau$. The new configurations form a new population $\mathcal{R}_k$.

2. For each random walker in $\mathcal{R}_k$, calculate the *branching probability*:

$$w_\alpha = \tilde{W}(\boldsymbol{R}_{k,\alpha}, \boldsymbol{R}_{k-1,\alpha}; \delta\tau). \tag{4.76}$$

Here one has to calculate the local energies $E_\mathrm{L}(\boldsymbol{R}_{k,\alpha})$ and $E_\mathrm{L}(\boldsymbol{R}_{k-1,\alpha})$ in order to calculate w_α.

3. For each random walker in $\mathcal{R}_k$, calculate the *branching factor*:

$$n_\alpha = \mathrm{int}(w_\alpha + \xi). \tag{4.77}$$

Here, n_α is the closest integer to $w_\alpha + \xi$, where ξ is a random number drawn from the uniform distribution in $[0, 1)$. If $n_\alpha \geq 1$, replace $\boldsymbol{R}_{k,\alpha}$ with n_α identical copies of itself in $\mathcal{R}_k$. If $n_\alpha = 0$, eliminate $\boldsymbol{R}_{k,\alpha}$ from $\mathcal{R}_k$. This is the *branch-and-death* stage. Generally, the number of walkers in $\mathcal{R}_k$ will change due to branching.

4. Update the energy estimator $\overline{E_{0,k}}$, according to Eq. (4.78). Update other estimators if needed.

5. Repeat Steps 1 to 4 until the target number of time steps M is reached. The quantity $\overline{E_{0,M}}$ will be the best approximation of the ground state.

The ground state energy depends on the average of the local energy over the stationary distribution $f_\infty(\boldsymbol{R}) = f(\boldsymbol{R}, \tau \to \infty)$, according to Eq. (4.62). The estimator for $\overline{E_0}$ after a long enough DMC calculation of M time steps is

$$\overline{E_0} = \frac{\displaystyle\sum_{k=1}^{M}\sum_{\alpha=1}^{N_{\mathrm{w},k}} w_{k,\alpha} E_\mathrm{L}(\boldsymbol{R}_{k,\alpha})}{\displaystyle\sum_{k=1}^{M}\sum_{\alpha=1}^{N_{\mathrm{w},k}} w_{k,\alpha}}. \tag{4.78}$$

Since the stationary distribution is reached only after a large enough number of time steps, it is recommended to evaluate Eq. (4.78) after a burn-in phase of M_burn time steps. During this lapse of time, only steps 2 to 4 are realized, but not step 5.

Ideally, to calculate Eq. (4.78), no restrictions over the number of walkers should be imposed at any time. In practice, the number of walkers can grow

large enough that, in order to track their evolution, the computational resources are insufficient: whether available memory is exhausted, or the computation time of a single time step is prohibitive. Hence, a *population-control* stage is introduced in the sampling procedure after updating the estimators of interest in step 5. In this stage, the trial energy is updated according to

$$E_{\text{T},k} = \overline{E_{0,k}} - \frac{C}{\delta\tau} \ln\left(\frac{N_{\text{w},k}}{N_{\text{w,ref}}}\right), \tag{4.79}$$

where C is a constant, and $N_{\text{w,ref}}$ is a desired average number of walkers we would like to maintain during the calculation. The population-control procedure has benefits but introduces a systematic *bias* on the stationary distribution. This bias introduces an error on $\overline{E_{0,k}}$, which is generally small and decreases as $1/N_{\text{w},k}$.

4.5.5. Statistical Error

The statistical error of Eq. (4.80) is more difficult to calculate than the error of the VMC energy estimator Eq. (4.40) since the former is the quotient of two estimators:

$$\overline{E_0} = \frac{\overline{Ew}}{\overline{w}}. \tag{4.80}$$

Here,

$$\overline{Ew} = \frac{1}{M}\sum_{k=1}^{M} E_k W_k, \quad \overline{w} = \frac{1}{M}\sum_{k=1}^{M} W_k, \tag{4.81}$$

where

$$W_k = \sum_{\alpha=1}^{N_{\text{w},k}} w_{k,\alpha}, \quad E_k = \frac{1}{W_k}\sum_{\alpha=1}^{N_{\text{w},k}} w_{k,\alpha} E_{\text{L}}(\boldsymbol{R}_{k,\alpha}). \tag{4.82}$$

By propagation of uncertainty, the variance of $\overline{E_0}$ is

$$\sigma_{\overline{E_0}}^2 = \left(\overline{E_0}\right)^2 \left[\frac{\sigma_{\overline{Ew}}^2}{\overline{Ew}^2} + \frac{\sigma_{\overline{w}}^2}{\overline{w}^2} - 2\frac{\left\langle \overline{Ew}; \overline{w} \right\rangle}{\overline{Ew}\,\overline{w}}\right], \tag{4.83}$$

where $\langle X; Y \rangle = \langle XY \rangle - \langle X \rangle \langle Y \rangle$ is the covariance between the random variables X and Y. Note that the variance estimator Eq. (4.83) has a bias that decreases as $1/M$.

The variances of $\overline{Ew}$, $\overline{w}$, and the covariance between them, can be related to their integrated autocorrelation times according to Eq. (4.26),

$$\sigma^2_{\overline{Ew}} = \sigma^2_{E_i w_i} \frac{2\tau_{E_i w_i}}{M}, \tag{4.84a}$$

$$\sigma^2_{\overline{w}} = \sigma^2_{w_i} \frac{2\tau_{w_i}}{M}, \tag{4.84b}$$

$$\left\langle \overline{Ew}; \overline{w} \right\rangle = \langle E_i w_i; w_i \rangle \frac{2\tau_{\langle E_i w_i; w_i \rangle}}{M}. \tag{4.84c}$$

The autocorrelation time of the covariance between the estimators is [119]

$$\tau_{\langle E_i w_i; w_i \rangle} = \tau_{\langle w_i; E_i w_i \rangle} = \frac{1}{2} + \sum_{k=1}^{M} \frac{\langle E_i w_i; w_k \rangle}{\langle E_i w_i; w_i \rangle} \left(1 - \frac{k}{M} \right). \tag{4.85}$$

To calculate the autocorrelation times, we can use a reblocking analysis, as described in Section 4.3.2. Hence, the statistical error of the ground state energy is given by

$$\epsilon_{\overline{E_0}} = \left| \overline{E_0} \right| \left[\frac{\sigma^2_{E_i w_i}}{\overline{Ew}^2} \frac{2\tau_{E_i w_i}}{M} + \frac{\sigma^2_{w_i}}{\overline{w}^2} \frac{2\tau_{w_i}}{M} - 2\frac{\langle E_i w_i; w_i \rangle}{\overline{Ew}\,\overline{w}} \frac{2\tau_{\langle E_i w_i; w_i \rangle}}{M} \right]^{1/2}. \tag{4.86}$$

The statistical error of other estimators can be calculated in a similar way than the energy error.

4.5.6. Time-Step Dependence

The DMC algorithm previously described is valid only in the short time $\delta\tau$ limit. For sufficiently small time steps, the ground state energy Eq. (4.78) scales linearly:

$$\overline{E}_0(\delta\tau) = E_0 + \kappa\delta\tau. \tag{4.87}$$

When high accuracy is required, the energy estimator is calculated for two or more time steps $\{\delta\tau_i\}$. Then, the exact ground state energy is obtained by extrapolating to $\delta\tau = 0$ [].

Some improvements have been proposed in order to reduce or eliminate the time-step dependence; for instance, in Ref. [127]. In this work, the authors propose the inclusion of an accept-reject stage, through a Metropolis-Hastings algorithm, during the diffusion process to make the ground state energy estimator practically independent of $\delta\tau$. Also, in Ref. [32], the authors introduce

a higher-order decomposition for the short-time Green's function such that the ground state energy depends quadratically on the time step. Hence, it becomes plausible to calculate the properties of the system with high accuracy using only one value of $\delta\tau$.

4.5.7. Pure Estimators

Calculation of mixed estimators Eq. (4.59) suffers from a significant limitation: it gives an exact result for the ground state only when the operator $\hat{O}$ commutes with the Hamiltonian. In this case, the ground state $\Phi_0(\boldsymbol{R})$ is both an eigenstate of $\hat{H}$ and $\hat{O}$, so it holds that

$$O_0 = \frac{\langle \Psi_\mathrm{T}| \hat{O} |\Phi_0\rangle}{\langle \Psi_\mathrm{T}|\Phi_0\rangle} = \frac{\langle \Psi_\mathrm{T}| \hat{O} |\Psi(\tau \to \infty)\rangle}{\langle \Psi_\mathrm{T}|\Psi(\tau \to \infty)\rangle} = \left\langle \hat{O} \right\rangle_\mathrm{mix}. \tag{4.88}$$

If $\hat{O}$ does not commute with $\hat{H}$, then $O_0 \neq \langle O\rangle_\mathrm{mix}$ even in the limit $\tau \to \infty$. In this case, the exact expected value corresponds to the *pure estimator*

$$\left\langle \hat{O} \right\rangle_\mathrm{pure} = \frac{\langle \Phi_0| \hat{O} |\Phi_0\rangle}{\langle \Phi_0|\Phi_0\rangle}. \tag{4.89}$$

Several techniques exist to calculate expected values that do not commute with the Hamiltonian, being the *extrapolation method* the most widely known. Using this method, one can obtain an approximation of the pure estimator from the values of the mixed estimator and the variational estimator (see Eq. (4.36)), assuming that the difference between the trial wave function $\Psi_\mathrm{T}(\boldsymbol{R})$ and the ground state $\Phi_0(\boldsymbol{R})$ is small: $\delta\Psi(\boldsymbol{R}) = \Phi_0(\boldsymbol{R}) - \Psi_\mathrm{T}(\boldsymbol{R})$. The approximated value of the pure estimator with a second-order error in $\delta\Psi(\boldsymbol{R})$ can be written as

$$\left\langle \hat{O} \right\rangle_\mathrm{pure} = 2 \left\langle \hat{O} \right\rangle_\mathrm{mix} - \left\langle \hat{O} \right\rangle_\mathrm{var} + \mathcal{O}(\delta\Psi^2). \tag{4.90}$$

Here, $\left\langle \hat{O} \right\rangle_\mathrm{pure}$ is obtained from a VMC and a DMC. The main limitation of this method is evident: the extrapolated estimate depends heavily on the quality of the wave function $\Psi_\mathrm{T}(\boldsymbol{R})$ used for importance sampling, and the bias of the approximation is difficult to quantify.

To overcome the limitations of the extrapolation method, we can use *forward walking* methods to sample the pure estimator directly from the mixed distribution. Let us consider the pure estimator Eq. (4.89) of a local observable:

$\langle \boldsymbol{R}| \hat{\boldsymbol{O}} |\boldsymbol{R'}\rangle = \hat{\boldsymbol{O}}(\boldsymbol{R'})\delta(\boldsymbol{R'} - \boldsymbol{R})$, which can be written as

$$\left\langle \hat{\boldsymbol{O}} \right\rangle_{\text{pure}} = \frac{\int d\boldsymbol{R}\ \Psi_{\text{T}}^*(\boldsymbol{R}) \left[\dfrac{\Phi_0^*(\boldsymbol{R})}{\Psi_{\text{T}}^*(\boldsymbol{R})} \right] \hat{\boldsymbol{O}}(\boldsymbol{R})\Phi_0(\boldsymbol{R})}{\int d\boldsymbol{R}\ \Psi_{\text{T}}^*(\boldsymbol{R}) \left[\dfrac{\Phi_0^*(\boldsymbol{R})}{\Psi_{\text{T}}^*(\boldsymbol{R})} \right] \Phi_0(\boldsymbol{R})}. \tag{4.91}$$

If we consider only real trial wave functions as we have done in previous sections, then the pure estimator can be written in terms of the mixed distribution Eq. (4.63):

$$\left\langle \hat{\boldsymbol{O}} \right\rangle_{\text{pure}} = \frac{\int d\boldsymbol{R}\ f(\boldsymbol{R}, \tau \to \infty) \left[\dfrac{1}{\Psi_{\text{T}}(\boldsymbol{R})}\hat{\boldsymbol{O}}(\boldsymbol{R})\Psi_{\text{T}}(\boldsymbol{R})\dfrac{\Phi_0(\boldsymbol{R})}{\Psi_{\text{T}}(\boldsymbol{R})} \right]}{\int d\boldsymbol{R}\ f(\boldsymbol{R}, \tau \to \infty) \left[\dfrac{\Phi_0(\boldsymbol{R})}{\Psi_{\text{T}}(\boldsymbol{R})} \right]}. \tag{4.92}$$

This expression for the pure estimator looks similar to the mixed estimator Eq. (4.62) but for the function

$$\mathcal{O}(\boldsymbol{R}) = \frac{1}{\Psi_{\text{T}}(\boldsymbol{R})}\hat{\boldsymbol{O}}(\boldsymbol{R})\Psi_{\text{T}}(\boldsymbol{R})\frac{\Phi_0(\boldsymbol{R})}{\Psi_{\text{T}}(\boldsymbol{R})}. \tag{4.93}$$

Here, the operator $\hat{\boldsymbol{O}}$ acts over the ground state $\Phi_0(\boldsymbol{R})$, which we do not know but until the end of the DMC calculation. Then, it is not clear how we can sample the mixed distribution and, at the same time, obtain the pure estimator Eq. (4.89).

According to [128], the quotient $\Phi_0(\boldsymbol{R})/\Psi_{\text{T}}(\boldsymbol{R})$ is proportional to the population obtained from a walker $\boldsymbol{R}$ in the asymptotic regime, i.e., when $\tau \to \infty$. Then, the number of descendants of this walker can be used as a weight $W(\boldsymbol{R})$. Therefore, the pure estimator Eq. (4.92) becomes

$$\left\langle \hat{\boldsymbol{O}} \right\rangle_{\text{pure}} = \frac{\sum\limits_{k} \mathcal{O}_{\text{L}}(\boldsymbol{R}_k)W(\boldsymbol{R}_k)}{\sum\limits_{k} W(\boldsymbol{R}_k)}. \tag{4.94}$$

Here, $\mathcal{O}_{\text{L}}(\boldsymbol{R})$ is the local observable defined in Eq. (4.38), and the summation $\sum_k$ runs over all the walkers and all times in the asymptotic regime. Algorithms capable of tracking which walker of a preceding configuration originated a present walker at any time of a DMC calculation have been devised [129]. Then, Eq. (4.94) can be used. An alternative algorithm was introduced by J.

Boronat and J. Casulleras in [33]. This method has the advantage that operates only over the generation of walkers present at a given time step, without tagging. Also, it can be introduced in the DMC algorithm without significant modifications. The following instructions should be implemented in the context of the procedure described in Section 4.5.4.

Initialization

At time-step $k = 0$, calculate the local observable over each one of the walkers:

$$\mathcal{O}_{0,\alpha} = \mathcal{O}_{\mathrm{L}}(\boldsymbol{R}_{0,\alpha}), \quad \alpha = 1, \ldots, N_{\mathrm{w},0} \tag{4.95}$$

Main procedure

At time steps $1, 2, \ldots M$:

- In Step 1.

  Before the gaussian diffusion: for each walker in the previous population $\mathcal{R}_{k-1}$, keep track of the corresponding measurement:

  $$(\mathcal{O}_{k,\alpha})_{\mathrm{parent}} = \mathcal{O}_{k-1,\alpha}. \tag{4.96}$$

  After the gaussian diffusion: evaluate the local observable for each one of the walkers in the new population $\mathcal{R}_k$:

  $$\mathcal{O}_{k,\alpha} = \mathcal{O}_{\mathrm{L}}(\boldsymbol{R}_{k,\alpha}). \tag{4.97}$$

- In Step 3.

  After the branching of the walker $\boldsymbol{R}_{k,\alpha}$, replicate (or drop) the measurement $\mathcal{O}_{k,\alpha}$ as many times as the walker. Then, for each surviving walker in the new population, keep track of the observable value corresponding to their "parent" walker $(\mathcal{O}_{k,\alpha})_{\mathrm{parent}}$ before the diffusion in Step 1.

- In Step 4.

  For each one of the walkers, update $\mathcal{O}_{k,\alpha}$ according to:

  $$\mathcal{O}_{k,\alpha} \leftarrow \mathcal{O}_{k,\alpha} + (\mathcal{O}_{k,\alpha})_{\mathrm{parent}}. \tag{4.98}$$

To reach the asymptotic regime, we repeat this process (and accumulate measurements) until we reach a sufficiently long time. After M time steps of this forward walking, we end up with $N_{\mathrm{w},M}$ walkers and the same number of measurements $\{\mathcal{O}_{M,\alpha}\}_{\alpha=1,\ldots,N_{\mathrm{w},M}}$. The pure estimator of $\hat{O}$ is

$$\left\langle \hat{O} \right\rangle_{\mathrm{pure}} = \frac{1}{M \times N_{\mathrm{w},M}} \sum_{\alpha=1}^{N_{\mathrm{w},M}} \mathcal{O}_{M,\alpha}. \tag{4.99}$$

4.6. Trial Wave Functions

Up to this point, we have not specified the mathematical form of the trial wave functions. A trial wave function $\Psi_{\mathrm{T}}(\boldsymbol{R})$ of good quality is an essential part of VMC and DMC calculations. First, it should be a good approximation of the ground state of the system. At the same time, its derivatives should be easy to compute since they are evaluated repeatedly in the calculations due to the action of the Hamiltonian.

There is a standard mathematical form for ground-state trial wave functions for systems with two-body interactions, i.e., where $V_{\mathrm{int}}(\boldsymbol{r}_i, \boldsymbol{r}_j) = V_{\mathrm{int}}(\boldsymbol{r}_i - \boldsymbol{r}_j)$, known as *Slater-Bijl-Jastrow* wave functions, initially used by A. Bijl [130] and R. Jastrow [131] to analyze the ground state of quantum many-body systems. The idea behind these wave functions consists of the following factorization:

$$\Psi_{\mathrm{T}}(\boldsymbol{R}) = \mathcal{S}(\boldsymbol{R})\mathcal{J}(\boldsymbol{R}). \tag{4.100}$$

The factor $\mathcal{S}(\boldsymbol{R})$ defines the symmetry of $\Psi_{\mathrm{T}}(\boldsymbol{R})$ in the face of the exchange of particles. For fermions, it must be antisymmetric, and it is generally constructed as a Slater determinant of specially chosen one-body particle orbitals. If required, spin states should be incorporated too. For bosons, the typical approach is to set $\mathcal{S}(\boldsymbol{R})$ equal to one.

The factor $\mathcal{J}(\boldsymbol{R})$ is known as the Bijl-Jastrow term and is constructed as follows:

$$\mathcal{J}(\boldsymbol{R}) = \prod_{i=1}^{N} f_1(\boldsymbol{r}_i) \times \prod_{i=1}^{N} \prod_{j=i+1}^{N} f_2(r_{ij}), \tag{4.101}$$

which is a product of one-body functions $f_1(\boldsymbol{r}_i)$ that depend only on the position of a single particle $\boldsymbol{r}_i$, times a second product of two-body functions and $f_2(r_{ij})$ that depend on the distance between any two pair of particles: $r_{ij} = |\boldsymbol{r}_i - \boldsymbol{r}_j|$. The choice of the one-body and two-body functions in Eq. (4.101) depends on the characteristics of the system under study. In general, the one-body functions are approximations to the eigenfunctions of the one-particle Hamiltonian

with the external potential $V_{\text{ext}}(\boldsymbol{r})$. Similarly, the two-body functions should be an approximation to the eigenfunctions of the two-body Hamiltonian with the interaction potential $V_{\text{int}}(\boldsymbol{r}_j - \boldsymbol{r}_j)$ only, but no external potential.

An alternative form for Eq. (4.100) is

$$\Psi_{\text{T}}(\boldsymbol{R}) = \mathcal{S}(\boldsymbol{R}) \exp(-U(\boldsymbol{R})), \tag{4.102}$$

where

$$U(\boldsymbol{R}) = \sum_{i=1}^{N} u_1(\boldsymbol{r}_i) + \sum_{i=1}^{N} \sum_{j=i+1}^{N} u_2(r_{ij}), \tag{4.103}$$

being the Jastrow term $\mathcal{J}(\boldsymbol{R}) = \exp(-U(\boldsymbol{R}))$. There is a direct relation between Eq. (4.100) and Eq. (4.102), since

$$u_1(\boldsymbol{r}_i) = -\ln f_1(\boldsymbol{r}_i), \quad u_2(r_{ij}) = -\ln f_2(r_{ij}), \tag{4.104}$$

so both forms are mathematically equivalent. However, the form Eq. (4.102) is more suitable for numerical calculations since it involves sums, making calculations more stable. The form Eq. (4.100), containing only products, may become a very large or tiny number even for a system with a small number of particles, so that it may lead to inaccurate results.

We can infer some properties of the one-body and two-body functions. For instance, in a homogeneous system, i.e., not external potential, the wave function must depend only on the relative distance between the particles due to translational invariance. Then, the one-body functions $u_1(\boldsymbol{r})$ must vanish,

$$u_1(\boldsymbol{r}) = 0 \implies f_1(\boldsymbol{r}) = 1. \tag{4.105}$$

Analogously, for a noninteracting system, the two-body functions $u_2(r)$ must vanish,

$$u_2(r) = 0 \implies f_2(r) = 1. \tag{4.106}$$

For an interacting system, the effect of interactions must decrease as the interparticle distance increases, whether the interactions are short range or long range. Then, two-body functions must fulfill

$$\lim_{r \to \infty} u_2(r) = 0 \implies \lim_{r \to \infty} f_2(r) = 1. \tag{4.107}$$

4.6.1. Optimization

Up to this point, we have omitted the explicit dependence of the trial wave function on any sort of free parameters beyond physical variables, like the position, for instance. Indeed, $\Psi_T(\boldsymbol{R})$ is also a function of some set of variational parameters $\boldsymbol{p} = \{p_1, p_2, \ldots, p_{N_p}\}$:

$$\Psi_T(\boldsymbol{R}) \equiv \Psi_T(\boldsymbol{R}; \boldsymbol{p}). \tag{4.108}$$

Parameters $\boldsymbol{p}$ affect the value of the energy estimator during a VMC calculation. Therefore, they should be chosen such that they minimize the variational energy Eq. (4.40). This process is called *optimization*.

Trial wave function optimization is not an easy task, even when the number of variational parameters is small since wave functions usually depend on a nonlinear fashion on them. Therefore, some sort of automatic procedure is needed to find the optimum values of the variational parameters. One such method is the *variance minimization* technique [132], whose primary goal is to minimize the variance of the local energy:

$$\sigma_{\text{opt}}^2 = \frac{\displaystyle\sum_{i=1}^{N_{\text{opt}}} [E_L(\boldsymbol{R}_i; \boldsymbol{p}) - E_{\text{guess}}] \, w(\boldsymbol{R}_i; \boldsymbol{p})}{\displaystyle\sum_{i=1}^{N_{\text{opt}}} w(\boldsymbol{R}_i; \boldsymbol{p})}. \tag{4.109}$$

Here, E_{guess} is a guess of the energy of the state. The weights $w(\boldsymbol{R}; \boldsymbol{p})$ are

$$w(\boldsymbol{R}; \boldsymbol{p}) = \left| \frac{\Psi_T(\boldsymbol{R}; \boldsymbol{p})}{\Psi_T(\boldsymbol{R}; \boldsymbol{p}_0)} \right|^2, \tag{4.110}$$

where $\boldsymbol{p}_0$ is the best set of variational parameters at the start of the optimization process.

The variance minimization process starts by choosing a set of configurations $\{\boldsymbol{R}_i\}_{i=1,\ldots,N_{\text{opt}}}$, from a previous VMC realization, for instance. This set remains fixed during the optimization procedure. One takes an initial set $\boldsymbol{p}_0$, while the VMC energy estimator corresponding to $\boldsymbol{p}_0$ may become an initial energy estimate E_{guess}. Then, employing some routine for global optimization of nonlinear problems, one obtains a new set of parameters $\boldsymbol{p}$ as a result. This procedure is repeated as many times as needed in order to reach a minimum of the variance.

Other methods used to optimize the trial wave functions minimize the expectation value of the energy $\overline{E}$ (see, e.g., [133]). These methods require several

full VMC calculations of $\overline{E}$ before an optimal set of variational parameters is found. Consequently, they are computationally more expensive than variance minimization. For this reason, variance minimization is the most frequently used technique for wave function optimization in QMC.

The optimization process is an essential step in a VMC calculation. On the other hand, although it is not a requirement in DMC since the algorithm samples the true ground state in the large time limit, a properly optimized wave function can reduce the number of time steps needed in order to reach the required numeric accuracy.

4.7. The Fixed-Node Approximation

The trial wave function of a fermionic system must be antisymmetric with respect to the exchange of particles. Then, it must have regions where it is positive as well as regions where it becomes negative, separated by nodal surfaces in the N-dimensional space. Naturally, the mixed distribution Eq. (4.63) shows similar behavior. A major problem that arises from the antisymmetry of the trial wave function is the so-called *fermionic sign problem*, a pathology of the algorithm where the signal-to-noise ratio due to the changing sign of the trial wave function is practically zero.

The most commonly used approach to overcome the fermionic sign problem is the *Fixed-Node Approximation* (FN-DMC). The basic idea of the approximation is to force the nodes of the fermionic ground state function to be the same as those of the trial wave function $\Psi_{\mathrm{T}}(\boldsymbol{R})$. In the N-dimensional space, these nodes define a hypersurface of $N-1$ dimensions. Then, the domain is partitioned in many nodal pockets whose walls (of infinite strength, i.e., they are impenetrable) are fixed by the nodes of $\Psi_{\mathrm{T}}(\boldsymbol{R})$. In each nodal pocket, the wave function and the mixed distribution $\Psi_{\mathrm{T}}(\boldsymbol{R})\Psi(\boldsymbol{R},\tau)$ have the same, fixed sign. Then, the solution of the many-body problem consists of solving the Schrödinger equation within these nodal pockets, subject to vanishing boundary conditions on the nodal surface.

Let v_α the volume of the nodal pockets delimited by the nodal surface. In each pocket, the mixed distribution is

$$f_\alpha(\vec{R}, \tau) = \Psi_{\mathrm{T}}(\boldsymbol{R})\Psi_\alpha(\boldsymbol{R}, \tau), \tag{4.111}$$

and it is positive (or negative, but with fixed-sign). Its time evolution is realized as we have explained in Section 4.5.4, with the constraint that the short-time Green's function only permits random moves within the same nodal pocket α: any random walker that crosses the nodal surface is killed. Then, in each pocket,

the FN-DMC yields an approximated ground state energy $E_{0,\alpha}$ and ground state function $\Phi_{0,\alpha}(\boldsymbol{R})$ that satisfy the relation

$$\hat{\boldsymbol{H}}\Phi_{0,\alpha}(\boldsymbol{R}) = E_{0,\alpha}\Phi_{0,\alpha}(\boldsymbol{R}), \quad \boldsymbol{R}_\alpha \in v_\alpha. \tag{4.112}$$

In a FN-DMC calculation, the initial distribution of walkers should cover as many pockets as possible. Then, the expected value of the energy becomes

$$E = \frac{\displaystyle\int d\boldsymbol{R}\, f(\boldsymbol{R}, \tau \to \infty) E_{\mathrm{L}}(\boldsymbol{R})}{\displaystyle\int d\boldsymbol{R}\, f(\boldsymbol{R}, \tau \to \infty)}, \tag{4.113}$$

where the full mixed distribution at large times is

$$f_\infty(\boldsymbol{R}) = f(\boldsymbol{R}, \tau \to \infty) = \sum_\alpha c_\alpha \Psi_{\mathrm{T}}(\boldsymbol{R})\Phi_{0,\alpha}(\boldsymbol{R}), \tag{4.114}$$

with the constant c_α depending on the initial population in the pocket v_α.

The energy Eq. (4.113) is also an upper bound to the ground state energy E_0 [126], and its best value will be obtained when all the nodal pockets have been populated. If somehow we knew how the true nodes of the ground state are, we would find that all of the nodal pockets have the same ground-state energy. Therefore, the initial distribution of the walkers is irrelevant. However, since we do not know the nodal surface exactly, the FN energy becomes a variational approximation: nodal surfaces of better quality, i.e., closer to the true ones, will yield better approximations to the exact ground state energy E_0.

4.8. Extended Systems

Realistically, QMC simulations are always realized on a finite volume of the space. The study of extended systems, i.e., those whose extent is unbounded (for instance, crystals or other structures with some type of periodicity) require additional procedures to correctly estimate the properties of the system from results calculated on finite subspaces.

Calculations on extended systems can be realized employing the *supercell approximation* [134] to reduce the study to a finite, manageable volume. This method consists in studying only a finite region of the space with volume Ω_{SC}, called *supercell*, which should contain (in principle) many primitive cells of the system. Then, QMC calculations are realized in this finite *simulation cell*. Let us call $\boldsymbol{R}$ to the set positions of the particles in Ω_{SC}: $\boldsymbol{R} = \{\boldsymbol{r}_1, \boldsymbol{r}_2, \ldots, \boldsymbol{r}_N\}$, and $\{\boldsymbol{l}\}$ the set of all lattice vectors of the system fixed by its structure, and possibly

by some external potential $V_{\text{ext}}(\boldsymbol{r})$ with a periodicity of $\{\boldsymbol{l}\}$. Then, the whole system is reconstructed (approximately) via translations of the particles in Ω_{SC} by supercell lattice vectors $\{\boldsymbol{L}\}$, which are a subset of $\{\boldsymbol{l}\}$. These translations create an infinite set of cells, which are exact images of the original cell Ω_{SC}, so the Hamiltonian of the whole system of the extended system is

$$\hat{\boldsymbol{H}} = \sum_{k=1}^{\infty} \hat{\boldsymbol{H}}_{\text{SC}}(\boldsymbol{R}_k) = \sum_{k=1}^{\infty} \left[\hat{\boldsymbol{h}}(\boldsymbol{R}_k) + \hat{\boldsymbol{V}}_{\text{int}-\text{im}}(\boldsymbol{R}_k) \right]. \tag{4.115}$$

Here, $\boldsymbol{R}_k = \{\boldsymbol{r}_{k,1}, \boldsymbol{r}_{k,2}, \ldots, \boldsymbol{r}_{k,N}\}$ represents the positions of particles in the k-th supercell. If n is the average density of the system, $N = n\Omega_{\text{SC}}$ is the number of particles in the cell. The Hamiltonian $\hat{\boldsymbol{h}}(\boldsymbol{R}_k)$ accounts for the interactions between particles in the k-th cell and is given by Eq. (4.1). The additional term $\hat{\boldsymbol{V}}_{\text{int}-\text{im}}(\boldsymbol{R}_k)$ represents the interactions of particles in the group $\boldsymbol{R}_k$ with other particles that lie in the infinitely large set of images of Ω_{SC}. Since the j-th particle in $\boldsymbol{R}_k$ has a set of images at positions $\boldsymbol{r}_{k,j} + \boldsymbol{L}$ and interacts with all of them, the expression for $\hat{\boldsymbol{V}}_{\text{int}-\text{im}}(\boldsymbol{R}_k)$ becomes

$$\hat{\boldsymbol{V}}_{\text{int}-\text{im}}(\boldsymbol{R}_k) = \frac{1}{2} \sum_{i=1}^{N} \sum_{j=1}^{N} \sum_{\boldsymbol{L} \neq \boldsymbol{0}} V_{\text{int}}(\boldsymbol{r}_{k,i} - \boldsymbol{r}_{k,j} - \boldsymbol{L}). \tag{4.116}$$

Consequently, the Hamiltonian of the supercell can be written as

$$\hat{\boldsymbol{H}}_{\text{SC}}(\boldsymbol{R}) = -\frac{\hbar^2}{2m} \sum_{i=1}^{N} \nabla_{\boldsymbol{r}_i}^2 + \sum_{i=1}^{N} V_{\text{ext}}(\boldsymbol{r}_i)$$
$$+ \frac{1}{2} \sum_{i=1}^{N} \sum_{j=1}^{N} \sum_{\boldsymbol{L} \neq \boldsymbol{0}} V_{\text{int}}(\boldsymbol{r}_i - \boldsymbol{r}_j - \boldsymbol{L}). \tag{4.117}$$

4.8.1. Twisted Boundary Conditions

Hamiltonian Eq. (4.117) (and consequently Eq. (4.115)) is invariant under the translation of any particle by a lattice vectors $\boldsymbol{L}$:

$$\hat{\boldsymbol{H}}_{\text{SC}}(\boldsymbol{r}_1, \ldots, \boldsymbol{r}_i + \boldsymbol{L}, \ldots, \boldsymbol{r}_N) = \hat{\boldsymbol{H}}_{\text{SC}}(\boldsymbol{r}_1, \ldots, \boldsymbol{r}_i, \ldots, \boldsymbol{r}_N). \tag{4.118}$$

Accordingly, the eigenfunctions of $\hat{\boldsymbol{H}}_{\text{SC}}$ are many-particle Bloch waves:

$$\Psi_{\boldsymbol{K},\alpha}(\boldsymbol{R}) = \Phi_{\boldsymbol{K},\alpha}(\boldsymbol{R}) \exp\left(i\boldsymbol{K} \cdot \sum_{j=1}^{N} \boldsymbol{r}_j \right) \tag{4.119}$$

In this expression, $\boldsymbol{K}$ is the lattice momentum, α is a band index, and $\Phi_{\boldsymbol{K},\alpha}(\boldsymbol{R})$ is a function that is invariant under the translation of any particle by a vector $\boldsymbol{L}$.

Let be $\boldsymbol{L}_j$, $j = 1, 2, 3$, with $\boldsymbol{L}_j \in \{\boldsymbol{L}\}$, the simulation cell "primitive" lattice vectors, such that $\Omega_{\mathrm{SC}} = |\boldsymbol{L}_1 \cdot (\boldsymbol{L}_2 \times \boldsymbol{L}_3)|$. Like the single-particle Bloch waves, many-particle Bloch waves acquire a phase when any particle is translated by a primitive supercell lattice vector:

$$\Psi_{\boldsymbol{K},\alpha}(\boldsymbol{r}_1, \ldots, \boldsymbol{r}_i + \boldsymbol{L}_j, \ldots, \boldsymbol{r}_N) =$$
$$e^{i\boldsymbol{K}\cdot\boldsymbol{L}_j}\, \Psi_{\boldsymbol{K},\alpha}(\boldsymbol{r}_1, \ldots, \boldsymbol{r}_i, \ldots, \boldsymbol{r}_N) \tag{4.120}$$

For zero $\boldsymbol{K}$, the phase is equal to one, and the wave function returns to the same value when the particle was in its original position. In this case, we say that the system satisfies *periodic boundary conditions*. On the other hand, if the momentum $\boldsymbol{K}$ is nonzero, the wave function does not return to its original value; we say that the system fulfills *twisted boundary conditions* [125].

An approximation to the ground-state energy can be obtained by taking the lowest band index only: $\alpha = 0$. Since the system has an infinite extent, the wave vector $\boldsymbol{K}$ varies continuously in the first Brillouin zone. Accordingly, the ground-state energy in the supercell can be written as [135]

$$E_{\mathrm{SC}} = \left\langle \hat{\boldsymbol{H}}_{\mathrm{SC}} \right\rangle = \frac{\Omega_{\mathrm{SC}}}{(2\pi)^3} \int_{\boldsymbol{K}\in\,\mathrm{F.B.Z.}} \left\langle \Psi_{\boldsymbol{K},0} \right| \hat{\boldsymbol{H}}_{\mathrm{SC}} \left| \Psi_{\boldsymbol{K},0} \right\rangle d. \tag{4.121}$$

In practice, this integral is approximated by a discrete sum over a finite number of $\boldsymbol{K}$ points; as the simulation cell volume Ω_{SC} increases, a smaller number of $\boldsymbol{K}$ points are required to represent the integral. The expected values of other operators are calculated similarly.

4.8.2. Fixed-Phase Approximation

In the study of systems subject to twisted boundary conditions, additional difficulties arise since the trial wave function must be complex-valued according to Eq. (4.120). Consequently, calculating the energy Eq. (4.121) gives rise to complex quantities during the evaluation of the local energy Eq. (4.34). In VMC calculations, this is not a significant problem: first, because the sampled probability distribution Eq. (4.33) is always real, and second, because expectation values of hermitian operators like the Hamiltonian are real, hence only the real part of the local energy is calculated and used. However, for DMC calculations, the mixed distribution Eq. (4.63) becomes complex, and can not be sampled following the methods described in Section 4.5 and Section 4.7. A complex trial wave function requires an alternative approach: the *fixed-phase method*.

As we know, during a DMC calculation, the mixed distribution $f(\boldsymbol{R}, \tau) = \Psi_{\mathrm{T}}^*(\boldsymbol{R})\Psi(\boldsymbol{R}, \tau)$ must remain positive. When using real wave functions, this

is not a significant difficulty for a bosonic system, whereas, for a fermionic system, this can be achieved using the fixed-node approximation. In the fixed-phase method, one starts by expressing the complex wave function in polar form: $\Psi(\boldsymbol{R}, \tau) = |\Psi(\boldsymbol{R}, \tau)| \exp(\varphi(\boldsymbol{R}, \tau))$, where both amplitude $|\Psi|$ and phase φ are real-valued functions. In a similar way to the fixed-node method, to obtain a real-valued mixed distribution, one forces Ψ to have the same phase as the trial wave function: $\Psi_{\mathrm{T}}(\boldsymbol{R}) = |\Psi_{\mathrm{T}}(\boldsymbol{R})| \exp(\varphi_{\mathrm{T}}(\boldsymbol{R}))$. This way, the mixed distribution $f(\boldsymbol{R}, \tau) = |\Psi_{\mathrm{T}}(\boldsymbol{R})| \, |\Psi(\boldsymbol{R}, \tau)|$ becomes a real-valued, positive function that can be sampled using DMC while keeping constant the phase φ_{T}. Like the fixed-node approximation, this procedure yields a variational upper bound estimate to the true ground-state energy of the system. A detailed discussion of the *fixed-phase* approximation is beyond the scope of this thesis but can be consulted in Ref. [136].

<div style="text-align: right">**5**</div>

QMC Study of the Bose Gas in Multi-Rods

In Chapter 3, we obtained the ground-state properties of a 1D Bose gas in a multi-rod lattice in the mean-field regime. Beyond this regime, e.g., when the interactions between particles are large enough, we have to resort to a different theory to correctly describe the system. In this chapter, we show how Quantum Monte Carlo (QMC) methods are used to numerically calculate the ground-state properties of our system for arbitrarily strong interactions. Also, we show how our results can be used in the context of the Luttinger liquid theory (see Section 2.9) to obtain the superfluid *vs.* Mott-insulator quantum phase diagram as a function of the parameters of our model.

5.1. The Hamiltonian of a Multi-Rod Lattice

Confinement Induced Resonances offer a way to probe the influence of interactions in one-dimensional trapped Bose gases (see Section 2.7). Moreover, the inclusion of an optical lattice in the axial direction provides a way to simulate periodic matter. The combination of CIRs and optical lattices may lead to the appearance of new phenomena and novel phase transitions [92].

Here, we proceed to analyze the physical properties for a degenerate, interacting 1D Bose gas within a multi-rod lattice. This structure is composed of a succession of permeable rods of width b, separated by empty regions of length a, along the z direction, so the period of the potential is $l = a + b$. We model the multi-rod periodic structure through a Krong-Penney potential (see Section 3.2). A noteworthy feature of the KP potential is its deep relation to the Dirac-comb potential. As we saw in Section 3.8.1, realizing novel types of optical lattices with sub-wavelength structure (SWOL) [36, 37] opens a way to

realize experiments with lattices formed by *nearly* Dirac-δ potentials, and even more complex combinations [113].

Our model allows repulsive interactions of arbitrary magnitude; therefore, the mean-field theory approach and GPE are generally not applicable. Still, we consider contact-like interactions between particles. Therefore, if we remove the multi-rod lattice, our system effectively corresponds to the Lieb-Liniger Bose gas (see Section 2.8). Hence, we can write the Hamiltonian of the full system as the Lieb-Liniger Hamiltonian plus an external potential,

$$
\begin{aligned}
\hat{\boldsymbol{H}} &= \hat{\boldsymbol{H}}_{\text{LL}} + \hat{\boldsymbol{V}}_{\text{ext}} \\
&= -\frac{\hbar^2}{2m} \sum_{i=1}^{N} \frac{\partial^2}{\partial z_i^2} + g_{\text{1D}} \sum_{i=1}^{N} \sum_{j=i+1}^{N} \delta(z_i - z_j) + \sum_{i=1}^{N} V_{\text{KP}}(z_i),
\end{aligned}
\tag{5.1}
$$

where N is the number of bosons, $V_{\text{KP}}(z)$ is the external KP potential, and g_{1D} is the interaction strength. The Lieb-Liniger parameter is $\gamma = mg_{\text{1D}}/\hbar^2 n_1$, where n_1 is the average linear density of the system.

5.2. Bijl-Jastrow Trial Wave Functions

A trial wave function for VMC and DMC calculations is constructed according to the general description of Slater-Bijl-Jastrow wave functions (see Section 4.6),

$$
\Psi_{\text{T}}(\boldsymbol{z}) = \mathcal{S}(\boldsymbol{z})\mathcal{J}(\boldsymbol{z}).
\tag{5.2}
$$

First, since we are studying a Bose gas, we need a symmetric wave function, so we set the symmetry factor to one: $\mathcal{S}(\boldsymbol{z}) = 1$. Next, we have to construct the Jastrow factor,

$$
\mathcal{J}(\boldsymbol{z}) = \prod_{i=1}^{N} f_1(z_i) \times \prod_{i=1}^{N} \prod_{j=i+1}^{N} f_2(r_{ij}),
\tag{5.3}
$$

where $\boldsymbol{z} = (z_1, z_2, \ldots, z_N)$ is the vector of positions of the bosons in the configuration space, and the relative distance is $r_{ij} = |z_i - z_j|$. Since we are studying an extended system, we will employ the supercell approximation, according to Section 4.8. In this work, we will be restricting ourselves to periodic boundary conditions, so real-valued wave functions are sufficient for our needs. Being a one-dimensional system, the primitive lattice vector of the multi-rod lattice is simply $\boldsymbol{l} = l\mathbf{e}_z$, where $\mathbf{e}_z$ is the unit-vector in the z direction, and l is the period of the lattice. The supercell lattice vector is chosen as $\boldsymbol{L} = m_z \boldsymbol{l}$, where m_z
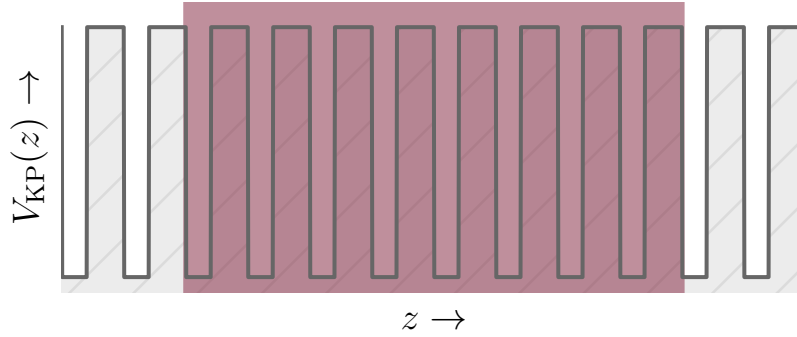
Figure 5.1: Supercell approximation. The primitive lattice is defined by the KP potential (gray barriers), while a supercell (red region) contains several primitive cells. The supercell repeats over and over to span the whole system.

is an integer greater or equal than one, so the simulation cell contains several primitive cells. This way, $\boldsymbol{L} = L\mathbf{e}_z$, with $L = m_z l$ being the length of the supercell.

We construct the one-body functions $f_1(z)$ as eigenfunctions of the single-particle Schrödinger equation with an external potential $V_{\mathrm{KP}}(z)$. As we saw in Section 3.2, these solutions are Bloch waves: $f_1(z) = e^{ik_z z}\phi_k(z)$, where k_z is the one-particle wave vector, and the function $\phi_k(z)$ has the same periodicity as the primitive lattice, i.e., $\phi_k(z + l) = \phi_k(z)$. We build the Jastrow factor from real-valued, Bloch waves with zero wave vector, which can be written as

$$f_1(z) = \begin{cases} \cos\left[\alpha_1\left(z - jl - a/2\right)\right], & V_{\mathrm{KP}}(z) = 0 \\ A\cosh\left[\kappa_1\left(z - jl + b/2\right)\right], & V_{\mathrm{KP}}(z) = V_0 \end{cases}, \tag{5.4}$$

where $l = a + b$ is the potential period, j is an integer, $\hbar\alpha_1 = \sqrt{2m\varepsilon_0}$, and $\hbar\kappa_1 = \sqrt{2m(V_0 - \varepsilon_0)}$. The parameter ε_0 is the ground state energy fixed by Eq. (3.10) with $k_z = 0$. At the same time, the continuity of the derivative of f_1 at the potential edges sets the constant A as

$$A = \sqrt{1 + \frac{V_0}{\varepsilon_0}\sinh^2\left(\frac{\kappa_1 b}{2}\right)}. \tag{5.5}$$

The two-body functions $f_2(r)$ are obtained as solutions of the two-particle Schrödinger equation with a mutual interaction $V_{\mathrm{int}}(r) = g_{\mathrm{1D}}\delta(r)$,

$$-\frac{\hbar^2}{2m_{\mathrm{red}}}\frac{d^2 f_2(r)}{dr^2} + g_{\mathrm{1D}}\delta(r)f_2(r) = \varepsilon f_2(r), \tag{5.6}$$

97

where $r = z_i - z_j$ is the relative coordinate, and $m^* = m/2$ is the reduced mass of the pair. Solutions with positive energy are plane waves, which we can simply write as

$$f_2(r) = A\cos(\alpha_2|r| + \varphi). \tag{5.7}$$

Here, both α_2 and φ are undetermined parameters of the wave function. These parameters are not entirely free since the presence of the delta potential at the origin gives rise to a discontinuity in the derivative of f_2 at the origin,

$$f_2'(0^+) - f_2'(0^-) = \frac{2}{|a_{1D}|}f_2(0). \tag{5.8}$$

If we conveniently write $\varphi = \alpha_2 r_0$ with r_0 being an offset and substitute Eq. (5.7) in Eq. (5.8), we find that

$$\alpha_2|a_{1D}|\tan(\alpha_2 r_0) = 1. \tag{5.9}$$

In the absence of an external potential, two-body functions should be a good representation of the exact ground-state wave function for an interval of g_{1D} as large as possible. This interval includes the limit of infinite interactions, i.e., the TG gas, whose ground-state wave function has the following form (up to normalization factor) [23]:

$$\Psi(\boldsymbol{z}) \propto \prod_{i=1}^{N}\prod_{j=i+1}^{N}\sin\left(\frac{\pi}{L}|z_i - z_j|\right). \tag{5.10}$$

Here, $\Psi(\boldsymbol{z})$ satisfies periodic boundary conditions under the translation of any of the bosons by L. The wave function Eq. (5.10) has the form of a Jastrow factor Eq. (4.101), which suggests the following extension for the trial wave function [34]:

$$f_2(r) = \begin{cases} A\cos(\alpha_2(|r| - r_0)) & 0 \le |r| < |r_m| \\ \sin\left(\frac{\pi|r|}{L}\right)^{\beta} & |r| > |r_m| \end{cases}. \tag{5.11}$$

This function can be interpreted in the following way: for $0 < |r| < |r_m|$ it is a solution of the Eq. (5.6) and takes into account the effect of the contact interaction at $r = 0$; for $|r| > |r_m|$, it approximates the ground-state wave function of a system that supports long-wavelength phonons [137] and is very close to Eq. (5.10) when $\beta = 1$. The distance $|r_m| < L/2$ is a variational parameter that separates both behaviors. Since bosons do not interact with other particles outside the simulation cell, the two-body function becomes equal to one at $|r| = L/2$, i.e., two bosons become uncorrelated. To determine the coefficients, we impose the following boundary conditions on Eq. (5.11):

- At the origin, it satisfies the relation $\alpha_2|a_{1\mathrm{D}}|\tan(\alpha_2 r_0) = 1$ due to the delta interaction between bosons (see Eq. (5.8)).

- It must be continuous a the matching point r_m:

$$A\cos(\alpha_2(|r_m| - r_0)) = \sin\left(\frac{\pi|r_m|}{L}\right)^{\beta}. \tag{5.12}$$

- Its derivative must be continuous at r_m. This condition, together with the continuity of f_2 yields the following equality:

$$-\alpha_2\tan(\alpha_2(|r_m| - r_0)) = \frac{\pi}{L}\beta\cot\left(\frac{\pi|r_m|}{L}\right). \tag{5.13}$$

- The local energy must be continuous at r_m. Together with the two previous conditions this condition yields

$$-\alpha_2^2 = \left(\frac{\pi}{L}\right)^2\beta\left[(\beta - 1)\cot^2\left(\frac{\pi|r_m|}{L}\right) - 1\right]. \tag{5.14}$$

These conditions fix the parameters α_2, A, β, and r_0 as functions of r_m.

5.3. Observables

Having defined the form of the trial wave function, here we show how to calculate some properties of the highest interest for us.

5.3.1. Local Energy

For both VMC and DMC calculations, the local energy is an essential quantity. According to its definition Eq. (4.34), and based on the Hamiltonian of our system Eq. (5.1), it can be written as

$$E_{\mathrm{L}}(\boldsymbol{z}) = -\frac{\hbar^2}{2m}\frac{1}{\Psi_{\mathrm{T}}(\boldsymbol{z})}\sum_{i=1}^{N}\frac{\partial^2}{\partial z_i^2}\Psi_{\mathrm{T}}(\boldsymbol{z})$$
$$+ g_{1\mathrm{D}}\sum_{i=1}^{N}\sum_{j=i+1}^{N}\delta(z_i - z_j) + \sum_{i=1}^{N}V_{\mathrm{KP}}(z_i). \tag{5.15}$$

In this expression, the calculation of potential energy is straightforward. On the other hand, the most laborious job is calculating the derivatives of the wave function. We can do this by defining

$$\mathcal{L}_{\mathrm{T}}(\boldsymbol{z}) = \ln\Psi_{\mathrm{T}}(\boldsymbol{z}) \implies \Psi_{\mathrm{T}}(\boldsymbol{z}) = \exp(\mathcal{L}_{\mathrm{T}}(\boldsymbol{z})). \tag{5.16}$$

Then, the action of the 1D-Laplacian $\nabla_z^2 = \sum_{i=1}^N \partial^2/\partial z_i^2$ is

$$
\begin{aligned}
\nabla_z^2 \Psi_{\mathrm{T}}(\boldsymbol{z}) &= \nabla_z^2 \exp(\mathcal{L}_{\mathrm{T}}(\boldsymbol{z})) && \text{(5.17a)} \\
&= \nabla_z \cdot \nabla_z \exp(\mathcal{L}_{\mathrm{T}}(\boldsymbol{z})) \\
&= \nabla_z \cdot [\exp(\mathcal{L}_{\mathrm{T}}(\boldsymbol{z})) \nabla_z \mathcal{L}_{\mathrm{T}}(\boldsymbol{z})] \\
&= \left[\nabla_z^2 \mathcal{L}_{\mathrm{T}}(\boldsymbol{z}) + \|\nabla_z \mathcal{L}_{\mathrm{T}}(\boldsymbol{z})\|^2 \right] \exp(\mathcal{L}_{\mathrm{T}}(\boldsymbol{z})) \\
&= \left[\nabla_z^2 \mathcal{L}_{\mathrm{T}}(\boldsymbol{z}) + \|\nabla_z \mathcal{L}_{\mathrm{T}}(\boldsymbol{z})\|^2 \right] \Psi_{\mathrm{T}}(\boldsymbol{z}). && \text{(5.17b)}
\end{aligned}
$$

Therefore, the local energy Eq. (5.15) becomes

$$
\begin{aligned}
E_{\mathrm{L}}(\boldsymbol{z}) = &-\frac{\hbar^2}{2m} \sum_{i=1}^N \left[\frac{\partial^2 \mathcal{L}_{\mathrm{T}}(\boldsymbol{z})}{\partial z_i^2} + \left(\frac{\partial \mathcal{L}_{\mathrm{T}}(\boldsymbol{z})}{\partial z_i} \right)^2 \right] \\
&+ g_{1\mathrm{D}} \sum_{i=1}^N \sum_{j=i+1}^N \delta(z_i - z_j) + \sum_{i=1}^N V_{\mathrm{KP}}(z_i).
\end{aligned} \tag{5.18}
$$

From the mathematical form of the trial wave function Eq. (5.2), it follows that

$$
\mathcal{L}_{\mathrm{T}}(\boldsymbol{z}) = \sum_{i=1}^N \ln f_1(z_i) + \sum_{i=1}^N \sum_{j=i+1}^N \ln f_2(z_i - z_j). \tag{5.19}
$$

After some steps, the full expression for the local energy can be written as

$$
\begin{aligned}
E_{\mathrm{L}}(\boldsymbol{z}) = &-\frac{\hbar^2}{2m} \sum_{i=1}^N \left[\frac{1}{f_1(z)} \frac{\partial^2 f_1}{\partial z^2} - \left(\frac{1}{f_1(z)} \frac{\partial f_1}{\partial z} \right)^2 \right]_{z=z_i} \\
&-\frac{\hbar^2}{2m} \sum_{i=1}^N \sum_{j=1}^N {}' \left[\frac{1}{f_2(r)} \frac{\partial^2 f_2}{\partial r^2} - \left(\frac{1}{f_2(r)} \frac{\partial f_2}{\partial r} \right)^2 \right]_{r=r_{ij}} \\
&-\frac{\hbar^2}{2m} \sum_{i=1}^N \left[\frac{1}{f_1(z_i)} \frac{\partial f_1}{\partial z} \bigg|_{z_i} + \sum_{j=1}^N {}' \frac{1}{f_2(r_{ij})} \frac{\partial f_2}{\partial r} \bigg|_{r_{ij}} \frac{r_{ij}}{|r_{ij}|} \right]^2,
\end{aligned} \tag{5.20}
$$

where the prime in the nested sums indicate $j \neq i$, and $r_{ij} = z_i - z_j$. The first two terms of Eq. (5.20) correspond to $\nabla_z^2 \mathcal{L}_{\mathrm{T}}(\boldsymbol{z})$; the third term arises from $\|\nabla_z \mathcal{L}_{\mathrm{T}}(\boldsymbol{z})\|^2$, and it is proportional to the squared modulus of the drift force Eq. (4.65):

$$
\boldsymbol{F}(\boldsymbol{z}) = 2 \frac{\nabla_z \Psi_{\mathrm{T}}(\boldsymbol{z})}{\Psi_{\mathrm{T}}(\boldsymbol{z})} = 2 \nabla_z \mathcal{L}_{\mathrm{T}}(\boldsymbol{z}). \tag{5.21}
$$

The form of Eq. (5.20) suggests the following definitions:

$$K_{\mathrm{L}}^{(1)}(z) = -\frac{1}{f_1(z)}\frac{\partial^2 f_1}{\partial z^2} + \left(\frac{1}{f_1(z)}\frac{\partial f_1}{\partial z}\right)^2, \tag{5.22a}$$

$$K_{\mathrm{L}}^{(2)}(r) = -\frac{1}{f_2(r)}\frac{\partial^2 f_2}{\partial r^2} + \left(\frac{1}{f_2(r)}\frac{\partial f_2}{\partial r}\right)^2, \tag{5.22b}$$

$$F_i(\boldsymbol{z}) = 2\left(\frac{1}{f_1(z_i)}\frac{\partial f_1}{\partial z}\bigg|_{z_i} + \sum_{j=1}^{N}{}'\frac{1}{f_2(r_{ij})}\frac{\partial f_2}{\partial r}\bigg|_{r_{ij}}\frac{r_{ij}}{|r_{ij}|}\right), \tag{5.22c}$$

Then, substituting these expressions in Eq. (5.20), together with the definition of the drift force, we obtain

$$E_{\mathrm{L}}(\boldsymbol{z}) = \frac{\hbar^2}{2m}\sum_{i=1}^{N}\left[K_{\mathrm{L}}^{(1)}(z_i) + \sum_{j=1}^{N}{}'K_{\mathrm{L}}^{(2)}(r_{ij}) - \frac{1}{4}F_i^2(\boldsymbol{z})\right]. \tag{5.23}$$

According to Eq. (5.22), the contribution to the local energy from the one-body functions Eq. (5.4) is

$$K_{\mathrm{L}}^1(z) = \begin{cases} \alpha_1^2\left(1 + \tan^2[\alpha_1(z - a/2)]\right) & V_{\mathrm{KP}}(z) = 0 \\ \kappa_1^2\left(-1 + \tanh^2\left[\kappa_1(z - l + b/2)\right]\right) & V_{\mathrm{KP}}(z) = V_0 \end{cases} ; \tag{5.24}$$

from the two-body functions Eq. (5.11), the contribution is

$$K_{\mathrm{L}}^2(r) = \begin{cases} \alpha_2^2\left(1 + \tan^2(\alpha_2(|r| - r_0))\right) & 0 \le |r| < |r_m| \\ \left(\frac{\pi}{L}\right)^2\beta\left(1 + \cot^2\left(\frac{\pi|r|}{L}\right)\right) & |r| > |r_m| \end{cases} , \tag{5.25}$$

while the i-th component of the drift force contributes with

$$\begin{aligned} F_i(\boldsymbol{z}) = {}&2\begin{cases} -\alpha_1\tan[\alpha_1(z_i - a/2)] & V_{\mathrm{KP}}(z) = 0 \\ \kappa_1\tanh\left[\kappa_1(z_i - l + b/2)\right] & V_{\mathrm{KP}}(z) = V_0 \end{cases} \\ &+ 2\sum_{j=1}^{N}{}'\frac{r_{ij}}{|r_{ij}|}\begin{cases} -\alpha_2\tan(\alpha_2(|r_{ij}| - r_0)) & 0 \le |r_{ij}| < |r_m| \\ \left(\frac{\pi}{L}\right)\beta\cot\left(\frac{\pi|r_{ij}|}{L}\right) & |r_{ij}| > |r_m| \end{cases}. \end{aligned} \tag{5.26}$$

Once determined the full expression of the local energy, we can calculate an approximation of the ground-state energy according to Eq. (4.40) for VMC, or Eq. (4.78) for DMC.

5.3.2. Static Structure Factor

The presence of a lattice can promote a quantum phase transition in the system from a superfluid (SF) state to a Mott-insulator (MI) state [91, 92] or vice-versa. A fingerprint of these phases can be obtained from the static structure factor $S(k)$ [138]:

$$S(k) = \frac{1}{N} \left(\langle \hat{\boldsymbol{n}}_{1;k}^\dagger \hat{\boldsymbol{n}}_{1;k} \rangle - \langle \hat{\boldsymbol{n}}_{1;k}^\dagger \rangle \langle \hat{\boldsymbol{n}}_{1;k} \rangle \right). \tag{5.27}$$

Here, the operator $\hat{\boldsymbol{n}}_k$ is the Fourier transform of the density operator $\hat{\boldsymbol{n}}_1(z)$,

$$\hat{\boldsymbol{n}}_{1;k} = \int dz\, e^{ikz} \hat{\boldsymbol{n}}_1(z), \tag{5.28}$$

so the static structure factor is determined by the fluctuations of the density. For a system with N particles at positions $\{z_1, z_2, \ldots, z_N\}$,

$$\hat{\boldsymbol{n}}_1(z) = \sum_{j=1}^{N} \delta(z - z_j) \implies \hat{\boldsymbol{n}}_{1;k} = \sum_{j=1}^{N} e^{ikz_j}. \tag{5.29}$$

Since $\hat{\boldsymbol{n}}_{1;k}^\dagger = \hat{\boldsymbol{n}}_{1;-k}$, one obtains

$$S(k) = \frac{1}{N} \left(\langle \hat{\boldsymbol{n}}_{1;k} \hat{\boldsymbol{n}}_{1;-k} \rangle - |\langle \hat{\boldsymbol{n}}_{1;k} \rangle|^2 \right). \tag{5.30}$$

The static structure factor (as well as its dynamic counterpart $S(k,\omega)$) is an important quantity that gives valuable information about single and collective excitations of a quantum gas. It is a quantity that can be probed by Bragg spectroscopy [139], where k is the momentum of a system excitation. For small momenta, it is sensitive to the structure and collective excitations of the system, showing a non-trivial behavior. On the other hand, for high-k values, it approximates to the model-independent value $\lim_{k\to\infty} S(k) = 1$.

Regarding the numerical side, one evaluates $S(k)$ in the following way. First, we split the Fourier density operator into both real and imaginary parts:

$$\hat{\boldsymbol{n}}_{1;k} = \sum_{j=1}^{N} \cos(kz_j) + i \sum_{j=1}^{N} \sin(kz_j). \tag{5.31}$$

Substituting this expression in Eq. (5.30), we arrive at

$$S(k) = \frac{1}{N} \left\langle \left(\sum_{j=1}^{N} \cos(kz_j) \right)^2 + \left(\sum_{j=1}^{N} \sin(kz_j) \right)^2 \right\rangle$$
$$- \frac{1}{N} \left(\left\langle \sum_{j=1}^{N} \cos(kz_j) \right\rangle^2 + \left\langle \sum_{j=1}^{N} \sin(kz_j) \right\rangle^2 \right). \tag{5.32}$$

This expression can be evaluated straightforwardly during VMC and QMC calculations for any random configuration z. For an extended system with periodic boundary conditions (which is our case), the value of k is not arbitrary but is quantized:

$$k_j = \frac{2\pi}{L} j, \qquad j \in j = 0, 1, 2, \ldots, \tag{5.33}$$

Here, L is the size of the simulation cell. As we have set $L = m_z l$, where $l = a + b$ is the period of the multi-rod lattice, then

$$k_j = \frac{2\pi}{l} \frac{j}{m_z}, \qquad j = 0, 1, 2, \ldots. \tag{5.34}$$

Finally, we can notice that calculating $S(k)$ involves the expected values of operators that do not commute with the Hamiltonian $\hat{H}$. To obtain a good approximation of the ground-state static structure factor, one has to resort to the extrapolation method or the forward walking method (see Section 4.5.7). In this thesis, we will employ the latter, since it is the only method that gives *bias*-free predictions for $S(k)$ and other local observables that do not commute with $\hat{H}$.

5.4. Ground-State Energy of the LL Bose Gas

In the absence of the multi-rod lattice, our system becomes the Lieb-Liniger Bose gas. This reduction suggests a way for testing the goodness of the trial wave function and the exactness of QMC implementations. The energy of the LL Bose gas can be obtained as indicated in Appendix A.1, and it can be compared directly to VMC and DMC results.

For the LL Bose gas, the magnitude of the interactions is measured in terms of the Lieb-Liniger parameter $\gamma = 2/n_1 a_{1D}$. As we saw in Section 2.8, the limit $n_1 a_{1D} \gg 1$ ($\gamma \ll 1$) corresponds to the weakly-interacting Bose gas that can be studied using GP formalism. On the other hand, for $n_1 a_{1D} \ll 1$ ($\gamma \gg 1$), the gas approaches to the TG Bose gas, whose properties are well known [23]. Based on Section 2.8, we know that for arbitrary values of $n_1 a_{1D}$, the LL ground-state energy is $E/N = (\hbar^2/2m)n_1^2 e(\gamma)$; by multiplying and dividing by a_{1D}^2 on the r.h.s. of Eq. (2.100), we obtain

$$\frac{\tilde{E}}{N} = (n_1 a_{1D})^2 e(\gamma). \tag{5.35}$$

Here, $\tilde{E} \equiv E/\varepsilon_{a_{1D}}$ is the energy of the gas rescaled in terms of $\varepsilon_{a_{1D}} \equiv \hbar^2/2m a_{1D}^2$. Consequently, we can always determine the function $e(\gamma)$ from any QMC calculation of the ground-state energy. In the mean-field regime, we have $e(\gamma) \to \gamma$;

from Eq. (5.35), we immediately obtain the behavior of the energy in this regime,

$$\frac{\tilde{E}}{N} \to 2n_1 a_{1D}. \tag{5.36}$$

On the other hand, in the TG regime $\gamma \to \pi^2/3$, so in the limit of impenetrable bosons, we obtain

$$\frac{\tilde{E}}{N} \to \frac{\pi^2}{3}(n_1 a_{1D})^2. \tag{5.37}$$

In Fig. 5.2, we have plotted the full behavior of the LL Bose gas ground-state energy as a function of $n_1 a_{1D}$, together with the energy in both Eq. (5.36) and Eq. (5.37) regimes. Also, we plot ground-state energy results calculated using DMC (and VMC) for $n_1 a_{1D} = 0.01$, 0.1, 0.3, 1, 10, 30, and 100, using $N = 100$ particles. Remarkably, both VMC and DMC energy results fall on
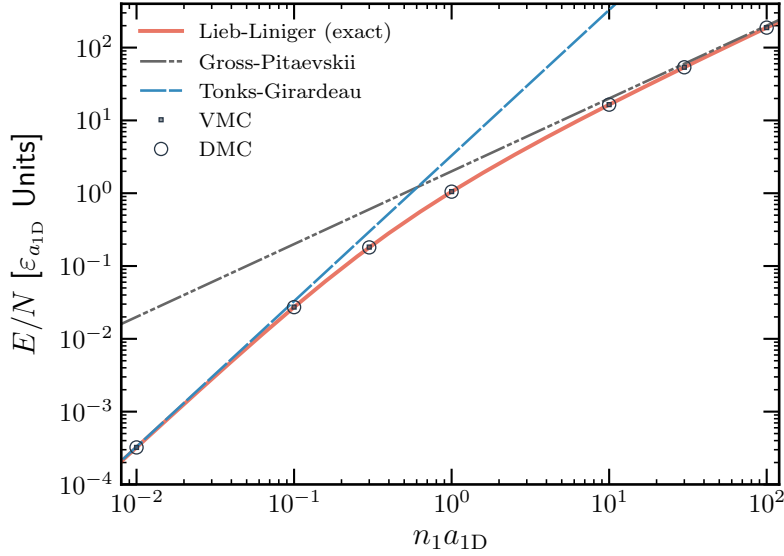
Figure 5.2: Ground-state energy of the Lieb-Liniger Bose gas, as a function of the gas parameter $n_1 a_{1D}$. Results using the exact LL energy Eq. (5.35) (solid red line), VMC (dark squares), and DMC (dark circles), are shown. Both Gross-Pitaevskii (dashed blue line) and Tonks-Girardeau (dash-dot-dot gray line) regimes are shown. An intermediate regime where both GP and TG results become inapplicable is visible, whereas VMC and DMC results lie above the exact energy for any value of $n_1 a_{1D}$.

the exact results obtained for the LL Bose gas. On the one hand, the results validate the accuracy of the computer program developed for both VMC and DMC methods. On the other hand, the results validate the goodness of the trial wave function Eq. (5.2) [34].

5.5. Mott Transition

Without a lattice potential, a Luttinger liquid is a superfluid at zero temperature [85, 140]. The introduction of a lattice potential may give rise to a quantum phase transition from the superfluid state to a Mott-insulator state, commonly known as *Mott-transition*. The essence of such a quantum phase transition is captured by the Bose-Hubbard model [4, 91, 92, 141, 142]: a system of bosonic particles with repulsive interactions subject to a lattice potential that can hop from a lattice site to the nearest sites only by quantum tunneling. The Mott transition is driven by the permanent competition between the particle interactions in a lattice site (captured by a U parameter) and the tunneling between adjacent lattice sites (captured by a J parameter). In the Mott-insulator state, each lattice site is filled by the same number of particles.

The first class of Mott transition can occur for sufficiently strong repulsive interactions and sufficiently high lattices, when the average density and the lattice period are commensurate, i.e., when its product (the filling) is an integer. The second class of transition can be driven by varying the chemical potential (which is equivalent to change the filling) while keeping the interactions (and the lattice height) constant. The first Mott transition class that occurs at commensurate filling is known as Mott-U transition, while the second one is known as Mott-δ transition. Remarkably, in 1D gases, an arbitrarily weak potential is enough to drive a Mott transition provided that the interactions are sufficiently strong [143].

In Section 2.9, we gave a general description of the Luttinger liquid theory for a homogeneous Bose gas. When a periodic potential $V(z)$ is introduced in the system, the low-energy Hamiltonian Eq. (2.114) ($\hat{\boldsymbol{H}}_0$ in the current context) becomes modified by a perturbation $\hat{\boldsymbol{H}}_V$ that accounts for the effects of the potential. Due to the periodicity of $V(z)$, the final form of $\hat{\boldsymbol{H}}$ corresponds to the quantum sine-Gordon model [78, 84, 85, 143]:

$$\hat{\boldsymbol{H}} = \hat{\boldsymbol{H}}_0 + \hat{\boldsymbol{H}}_V$$
$$= \hat{\boldsymbol{H}}_0 + V_j \int dz \, \cos\left(2p\hat{\phi}_l(z) - z\delta\right). \tag{5.38}$$

Here, V_j is a constant that depends on the form of $V(z)$, while

$$\delta = 2j\pi/l - 2p\pi n_1 \tag{5.39}$$

is the degree of incommensurability of the potential; both p and j integers, and l is the period of $V(z)$. In particular, $\delta = 0$ corresponds to a commensurate number of bosons per lattice site,

$$n_1 l = \frac{j}{p}. \tag{5.40}$$

For any commensurate filling, the sine-Gordon Hamiltonian can undergo a Mott-U transition [78, 85]; at the transition point, the Luttinger parameter K of the gas (see Section 2.9) takes a critical value K_c that depends only on the commensurability order p,

$$K_c \equiv \frac{2}{p^2}. \tag{5.41}$$

For instance, for a commensurability of order $p = 1$, the critical Luttinger parameter is $K_c = 2$. Physically, this commensurability order corresponds to an integer number of bosons per site: $n_1 l = j$.

For commensurate fillings, even in the presence of a periodic potential, a Luttinger liquid remains superfluid while $K > K_c$. Variations in the interaction strength can push K towards K_c. At the critical point, K jumps discontinuously from K_c in the superfluid phase to zero in the Mott-insulator phase. The excitation energy spectrum, which is non-gapped and increases linearly with the quasimomentum as $E(k) = c_s \hbar |k|$ in the superfluid state [83, 84], develops an excitation gap Δ in the Mott phase, so $E(k) = \sqrt{(c_s \hbar |k|)^2 + \Delta^2}$ [85]. On the other hand, the compressibility tends to a constant at the transition. It then drops discontinuously to zero in the Mott-insulator phase, since no density changes occur upon changing the chemical potential.

5.5.1. Evaluation of the Luttinger Parameter

In this thesis, we calculate K from the low-momenta behavior of the static structure factor $S(k)$. As we saw in Section 5.3.2, $S(k)$ gives valuable information about single and collective excitations in the system. In particular, one can obtain the velocity of propagation of the density collective excitations, i.e., the sound velocity c_s.

The low-momenta behavior of the energy spectrum $E(k)$ of the density collective excitations is related to the static structure factor through the well-known

106

Feynman relation [45, 144, 145]:

$$E(k) \equiv \frac{\hbar^2 k^2}{2mS(k)}. \tag{5.42}$$

This equation gives an upper estimate of the energy of the elementary excitations in terms of the static structure factor. For a Luttinger liquid, the excitation spectrum at long wavelengths is linear with k: $E(k) \sim c_s \hbar |k|$. Substituting the energy spectrum in Eq. (5.42), the sound velocity can be obtained (in the limit when $k \to 0$) as

$$c_s = \frac{\hbar}{2m} \lim_{k \to 0} \left(\frac{S(k)}{k} \right)^{-1}. \tag{5.43}$$

Next, we use relation Eq. (2.121) to relate the sound velocity with the Luttinger parameter, hence $c_s = \hbar k_F / mK$. Substituting this equality in Eq. (5.43), we obtain

$$K = 2k_F \lim_{k \to 0} \frac{S(k)}{k}. \tag{5.44}$$

Consequently, the Luttinger parameter can be obtained from the derivative of the static structure factor at zero wave vector. As long as the system is in the superfluid phase, i.e., $K > K_c$, the value obtained from Eq. (5.44) can be interpreted as the Luttinger parameter of the gas.

5.5.2. Evaluation of the Static Structure Factor

When we introduce the multi-rod lattice, the system acquires a new length scale: the lattice period l. This length fixes some critical parameters that define the quantum behavior of the system, as well as other parameters that control the QMC calculation efficiency. For instance, under the supercell approximation, we use a simulation box that contains several primitive lattice cells, i.e., $L = m_z l$, where m_z is the number of lattice sites. According to the definition of the average linear density: $n_1 \equiv N/L = N/m_z l$, the *filling* becomes

$$n_1 l \equiv \frac{N}{m_z}. \tag{5.45}$$

Its physical interpretation is straightforward: it represents the average number of particles per lattice site. At the same time, the recoil energy $E_R = \hbar^2 \pi^2 / 2ml^2$

becomes a natural energy scale for the multi-rod lattice height, and consequently, to measure the height V_0 of the KP potential barriers. Also, the interaction magnitude can be measured in terms of E_R,

$$\frac{g_{1D}n_1}{E_R} = 2\gamma\left(\frac{n_1 l}{\pi}\right)^2, \tag{5.46}$$

where $\gamma = 2/n_1 a_{1D}$ is the Lieb-Liniger parameter of the gas. In a QMC calculation, we set N and $L = m_z l$, so $n_1 l$ gets fixed too, and the interaction factor Eq. (5.46) that corresponds to a given γ can be determined. Then the QMC results can be compared with data obtained by other means, for instance, from experimental results, as well as from mean-field approximations.

Here we report the results obtained for the static structure factor at commensurate filling of order $p = 1$ using the DMC method adapted for calculation of pure estimators [32]. More specifically, from now on, all analyses will be done with $n_1 l = 1$, i.e., our system will have, on average, one boson per lattice site. Also, we will focus on the study of "square" multi-rod lattices, that is, where the distance a that separates any pair of rods (barriers of the KP potential) is equal to their width b. This condition means that any QMC simulation must be done in a supercell with as many lattice sites as particles according to Eq. (5.45), i.e., $N = m_z$. Also, as we impose periodic boundary conditions on the wave function, the wave vector can only take quantized values according to Eq. (5.34),

$$k_j = \frac{2\pi}{l}\frac{j}{N}, \qquad j = 0, 1, 2, \dots. \tag{5.47}$$

Since $n_1 l = 1$ and $k_F = \pi n_1$, the j-th wave vector can be written conveniently as

$$k_j = 2k_F\frac{j}{N}, \qquad j = 0, 1, 2, \dots. \tag{5.48}$$

As we saw at the start of Section 5.5, a Mott transition can be driven in a Luttinger liquid subject to a periodic potential in two ways: by a Mott-U transition, or by a Mott-δ transition. Here, we study the Mott-U transition by calculating the Luttinger parameter from Eq. (5.44) as a function of the interaction strength γ and the lattice height V_0. We estimate the boundary between both superfluid and Mott-insulator phases defined by the condition $K(\gamma, V_0) = K_c$. Finally, we use the previously obtained pairs (γ, V_0) to construct the zero-temperature phase diagram of the gas.

As our starting point, we report the behavior of the static structure factor for the LL Bose gas Fig. 5.3. We have plotted several curves for different values of the Lieb-Liniger parameter γ: as its value increases, the interactions become stronger. We can observe that for systems with weaker interactions, the static structure factor has a very steep slope, while as the interaction strength increases, the slope diminishes monotonically. As the Luttinger parameter is proportional to the slope of $S(k)$ at zero k, it follows that as the interaction increases, K diminishes. For substantial values of γ, i.e., for very strong interactions, $S(k)$ behaves more and more like the static structure factor of the TG Bose gas:

$$S_{\mathrm{TG}}(k) = \begin{cases} \dfrac{k}{2k_{\mathrm{F}}} & k < 2k_{\mathrm{F}} \\ 1 & k \geq 2k_{\mathrm{F}} \end{cases} . \tag{5.49}$$

From this expression and Eq. (5.43), we can easily verify that the sound velocity of the TG gas is $c_{\mathrm{s}} = v_{\mathrm{F}}$ [23], and the Luttinger parameter is $K = 1$. Hence, QMC calculations are in complete agreement with a result obtained at
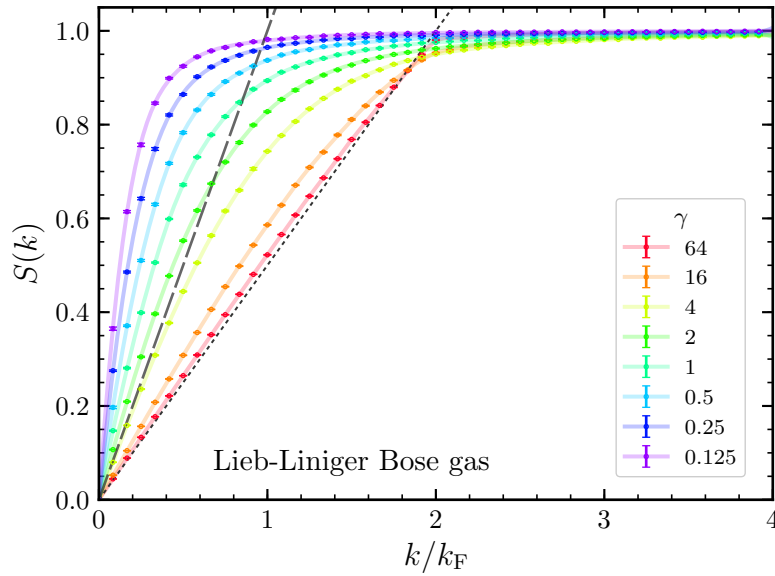
Figure 5.3: Static structure factor as a function of the wave vector for the Lieb-Liniger Bose gas. Each plotted curve corresponds to a different value of the LL parameter γ. The straight dashed line indicates the slope of $S(k)$ at the origin for which the Luttinger parameter K takes the critical value $K_{\mathrm{c}} = 2$. The dotted line indicates the slope of $S(k)$ for the TG Bose gas at $k < 2k_{\mathrm{F}}$.

the end of Section 2.9: the Luttinger parameter of a Lieb-Liniger Bose gas with finite repulsive interactions is always greater than one.

A quick examination of the results reported in Fig. 5.3 indicates that there is a minimum γ_c value where $K = K_c = 2$. One can notice that there is a family of $S(k)$ curves whose slope at the origin is below the dashed line with slope one. Consequently, the Luttinger liquid for these curves is below the critical value K_c. We can estimate the value of γ_c by calculating the slope of $S(k)$ at $k = 0$ from DMC results; then, we can obtain K as a function of γ using Eq. (5.44). The results we obtained from this procedure are shown in Fig. 5.4. As γ increases, we observe that K decreases until it reaches the critical value

Figure 5.4: LL Bose gas Luttinger parameter K as a function of γ^{-1}. K value was obtained from QMC results reported in Fig. 5.3 for $\gamma = 64$, 16, 4, 2, and 1. The horizontal dashed line indicates the critical value $K_c = 2$, while the black circle shows the transition point (γ_c, K_c), where $\gamma_c \sim 3.5$. The darker region indicates those values of γ for which an arbitrarily weak periodic potential can pin the bosons in a Mott insulator state.
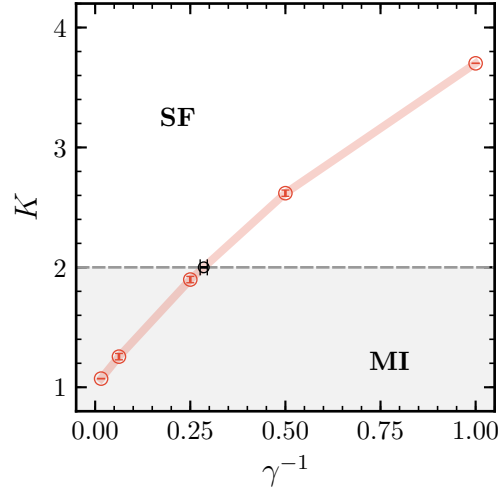
indicated by the dashed horizontal line. From our data, we have estimated that $\gamma_c^{-1} \sim 0.28$, or equivalently: $\gamma_c \sim 3.5$. This result is in complete agreement with theoretical estimations [143].

For interactions stronger than the critical value γ_c a novel phenomenon occurs: the superfluid Luttinger liquid can be driven to a Mott-insulator state by adding an arbitrarily weak periodic potential, pinning the bosons to the lattice sites. This phenomenon is a consequence of the particular type of Mott transition manifested by the low-energy, sine-Gordon Hamiltonian that models the system. For weaker interactions than the critical value γ_c, an arbitrarily weak potential can not trigger a Mott transition. However, for these γ values, the Mott transition can be driven by increasing the height of the periodic multi-rod lattice potential. The transition point depends on the value of the Luttinger parameter: as long as $K > K_c = 2$, the sine-Gordon Hamiltonian is unable to pin the bosons in the lattice sites. Hence, for a particular value $\gamma < \gamma_c$ the Mott

transition is triggered at a critical value of the potential height V_c; if $V_0 < V_c$, the system is a superfluid, whereas if $V_0 \geq V_c$ the system is a Mott-insulator.

Analogously to the LL Bose gas, for nonzero lattice potential, we determine the Luttinger parameter from the low-k behavior of the static structure factor $S(k)$. In Fig. 5.5, we show how the static structure factor of the gas changes in the presence of the multi-rod lattice; the strength of the interactions is $\gamma^{-1} = 1$ in Fig. 5.5a and $\gamma^{-1} = 0.5$ in Fig. 5.5b. According to the previous discussion, for this system, only a sufficiently high lattice can trigger the Mott-U transition. As expected, for the free Bose gas (FBG), the slope of $S(k)$ is above the transition line with slope one in both subfigures. As we increase the lattice height, the slope diminishes; ultimately, for some height V_0, the slope of the curve is clearly below the transition slope.

We have calculated the Luttinger parameter for all the $S(k)$ curves in both Fig. 5.5a and Fig. 5.5b. For $\gamma^{-1} = 1$ results are reported in Fig. 5.6a, while for $\gamma^{-1} = 0.5$ results are shown in Fig. 5.6b. The dependence of K on V_0 shows that for shallow lattices $K > K_c = 2$; this means that the Bose gas is in the superfluid state. As the lattice height increases, K diminishes until it crosses the line $K = K_c$ at some V_c. At this point, the gas becomes a Mott-insulator. We estimated the critical value V_c for both interactions: for γ^{-1}, we get $V_c \sim 4.39 E_R$, while for $\gamma^{-1} = 0.5$, we get $V_c \sim 2.05 E_R$. Similarly, we calculated the static structure factor $S(k)$ for $\gamma^{-1} = 0.75$, $\gamma^{-1} = 1.5$, $\gamma^{-1} = 2$, and $\gamma^{-1} = 5$. For these interactions, we obtained $V_c \sim 2.05 E_R$, $V_c \sim 3.57 E_R$, $V_c \sim 5.46 E_R$, $V_c \sim 6.60 E_R$, and $V_c \sim 9.92 E_R$, respectively.

5.5.3. Superfluid *vs.* Mott-Insulator Phase Diagram

Starting from the estimated values of the critical lattice height V_c as a function of the interaction γ^{-1}, together with the critical interaction γ_c^{-1} for the LL Bose gas, we can establish, at first approximation, the boundary between the superfluid and Mott-insulator phases of the 1D Bose gas in multi-rods. In Table 5.1, we report the calculated pairs (γ^{-1}, V_0). Finally, in Fig. 5.8, we report our DMC numerical results in the zero-temperature phase diagram γ-V_0 of the 1D Bose gas in multi-rods (black circles). In this figure we also report and compare with data from three relevant sources: first, experimental data reported at *Haller et al.* [92] (red squares and orange circles); second, data reported at *Boéris et al.* [146] (green squares and circles); and third, QMC data reported by *Astrakharchik et al.* [147] (blue squares). Before comparing any results, let us discuss a little more about the experimental data in the following lines.

On the one hand, Haller et al. [92] analyzed the Mott-U transition of a 1D Bose gas in an optical lattice $V_{opt}(z) = sE_R \sin^2(2\pi z/\lambda_{OL})$ at commensura-
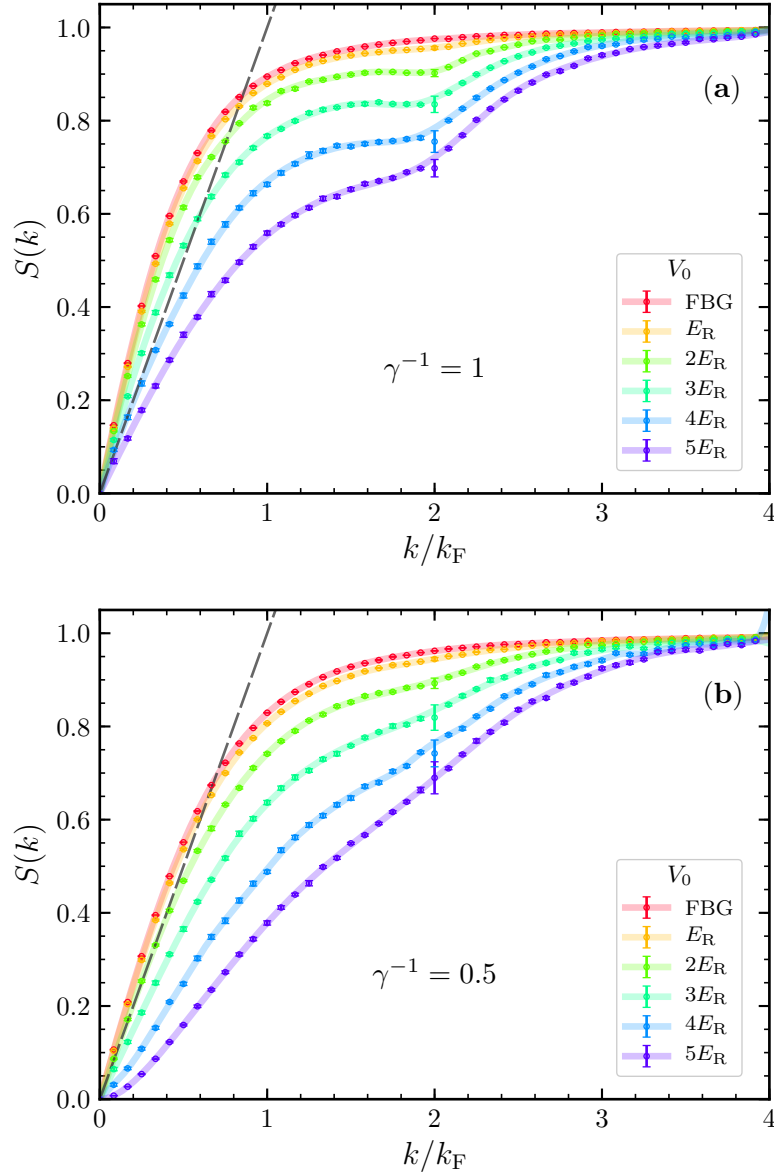
Figure 5.5: Static structure factor as a function of the wave vector. (**a**): $\gamma^{-1} = 1$, (**b**): $\gamma^{-1} = 0.5$. In both figures, the red curve represents the free Bose gas without periodic potential. Subsequent curves represent lattice with height $V_0 = 1, 2, 3, 4$, and 5 times E_{R}, for $\gamma^{-1} = 0.5$. The straight dashed line indicates the slope of $S(k)$ at the origin for which the Luttinger parameter K takes the critical value $K_{\mathrm{c}} = 2$
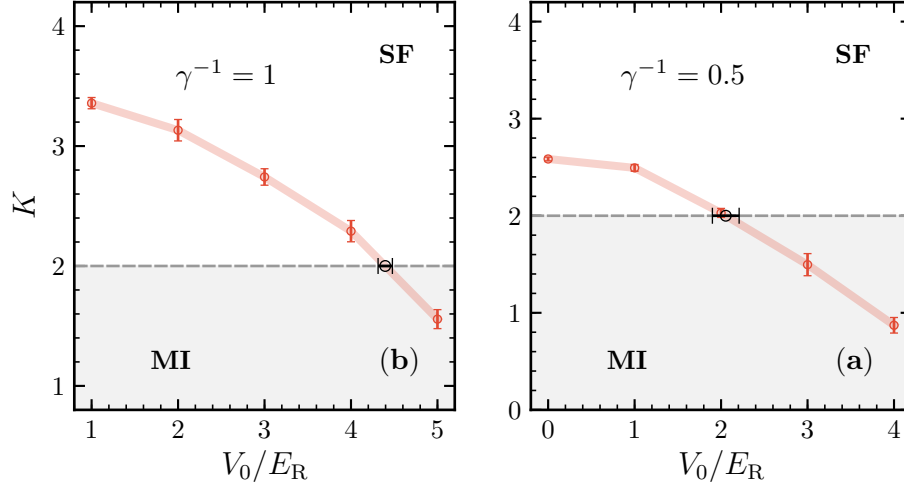
Figure 5.6: Luttinger parameter K as a function of V_0. (**a**): $\gamma^{-1} = 1$; K value was obtained from QMC results reported in Fig. 5.5a for $V_0 = 1$, 2, 3, 4, and 5 times E_R. (**b**): $\gamma^{-1} = 0.5$; K value was obtained from the QMC results reported in Fig. 5.5b for $V_0 = 0$ (FBG), 1, 2, 3, and 4 times E_R. In both figures, the horizontal dashed line indicates the critical value $K_c = 2$, while the black circle shows the transition point (V_c, K_c). Points in the darker region indicate systems which are Mott-insulators.

γ^{-1}	V_0 [E_R units]
0.28(1)	0
0.5	2.05(15)
0.75	3.57(10)
1	4.39(8)
1.5	5.46(7)
2	6.60(10)
5	9.92(24)

Table 5.1: Some critical points (γ^{-1}, V_0) that lie in the boundary that separates the superfluid phase from the Mott-insulator phase obtained from DMC calculations. The number between parenthesis indicates the statistical error in the last digits of the corresponding value.

bility $n_1 \sim 2/\lambda_{\mathrm{OL}}$, where $\lambda_{\mathrm{OL}}/2$ is the period of the optical lattice potential an s is the lattice height. The Mott transition was observed in two ways. The
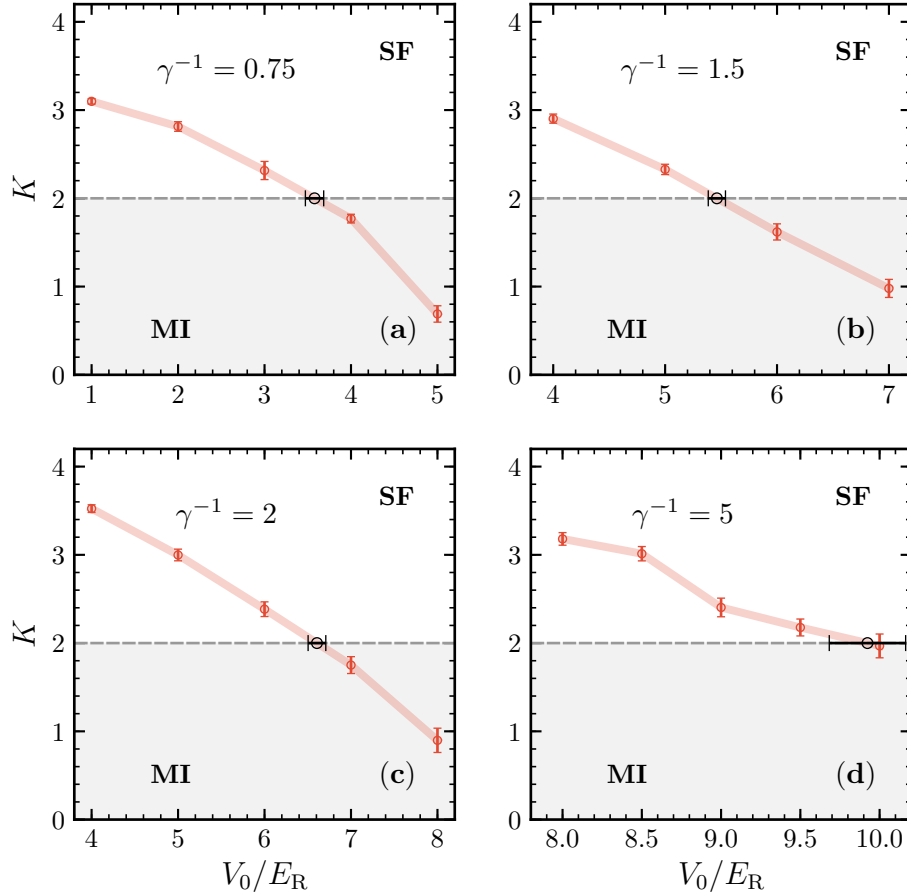
Figure 5.7: Luttinger parameter K as a function of V_0. (**a**): $\gamma^{-1} = 0.75$, (**b**): $\gamma^{-1} = 1.5$, (**c**): $\gamma^{-1} = 2$, and (**d**): $\gamma^{-1} = 5$. We can note that for weaker interactions (larger γ^{-1}), the lattice height must increase in order to trigger a Mott-U transition. The horizontal dashed line indicates the critical value $K_c = 2$, while the black circle shows the transition point (V_c, K_c). Points in the darker region indicate systems which are Mott-insulators.

first one by transport measurements (data marked by red squares in Fig. 5.8) in weakly-interacting gases ($\gamma^{-1} > 2$) and deep lattices (results are compared with predictions of the Bose-Hubbard model [148]). The second one by amplitude modulation spectroscopy (blue circles in Fig. 5.8) on strongly-interacting gases ($\gamma^{-1} < 1$) and shallow lattices (results are compared with predictions of the sine-Gordon model). On the other hand, Boéris et al. [146] also studied the Mott-U transition for a 1D Bose gas in an optical lattice at commensurabil-

ity $\langle n_1 \lambda_{\mathrm{OL}}/2 \rangle = 1$ by measurements of the momentum distribution, for both strongly and weakly-interacting gases, as well as for both shallow and deep optical lattices (green squares in Fig. 5.8). The authors also complemented their experimental results with QMC calculations (green circles in Fig. 5.8).

According to our results reported in Fig. 5.8 (black circles), we observe that for shallow lattices and strongly-interacting gases, our model predicts transition values V_{c} in excellent agreement with experimental results, but somewhat larger than the sine-Gordon model predictions. At γ_{c} and zero potential, both models agree; a similar correspondence occurs with results from [146] and [147] also. As the interaction goes below $\gamma^{-1} = 1$, our results are very close to [92] data and the predictions of the Bose-Hubbard model; however, they are slightly
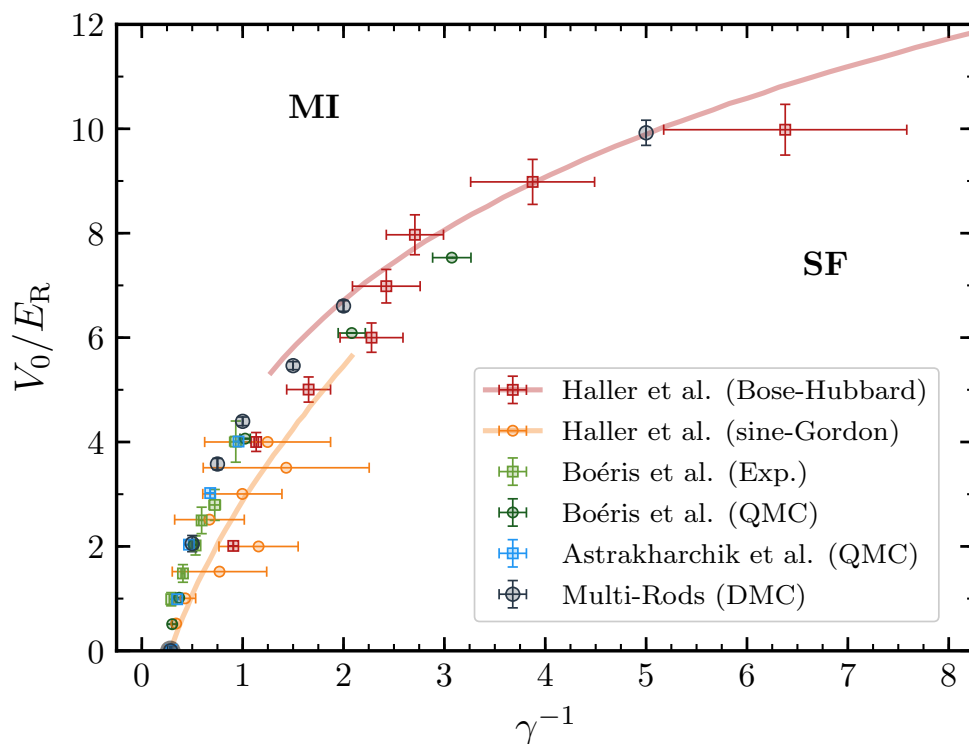
Figure 5.8: Phase diagram of the 1D Bose gas in a square multi-rods potential at zero temperature. The region above the critical points is the Mott-insulator phase, while the region below corresponds to the superfluid phase. We compare our results (black circles) against data from [92] (red squares and orange circles), [146] (green squares and circles), and [147] (blue squares). Our results are in excellent agreement with experimental and QMC data.

larger than QMC results from [146]. For $\gamma^{-1} > 1$, there is no experimental data reported by [146].

It can not go unnoticed that experimental data is obtained from Bose gases loaded into optical lattices, which are different from our multi-rod square lattice. Surprisingly, we found that our results are very close to experimental data, as Fig. 5.8 shows. Hence, results indicate that despite the obvious differences, our square multi-rod lattice effectively captures essential features of an optical lattice with the same period and height V_0.

6

Conclusions and Outlook

In this thesis, we report a detailed study of the ground-state properties of a 1D, interacting Bose gas in a multi-rod lattice at zero temperature. We have studied the system through two complementary approaches. In the first approach, we studied the ground-state properties of the Bose gas in the weakly-interacting regime using mean-field theory. In a second approach, we analyzed the ground-state properties beyond the mean-field regime using Quantum Monte Carlo techniques to obtain the zero-temperature properties, including the superfluid–Mott insulator quantum phase-transition diagram of the gas. In both approaches, we model the lattice structure through a periodic KP potential.

In the mean-field approach, we solved the 1D Gross-Pitaevskii equation subject to the corresponding normalization and boundary conditions. Physically, due to the symmetry and translational invariance of the multi-rod lattice, the condensate wave function can be written in the form of a Bloch wave. By expressing the wave function in polar form, we obtain a pair of differential equations for the density and the phase of the condensate wave function. We found that both density and phase can be determined analytically in terms of the Jacobi elliptic functions and the incomplete elliptic integrals of the first, second, and third kind. Next, we obtained the condensate properties as functions of the lattice height and the interaction strength between particles, namely: the particle number density, the energy band spectrum, the compressibility, and the first sound velocity. The energy band spectrum, in particular, shows an extraordinary feature, that is, the appearance of energy loops, also known as swallow-tails, at the edge of the first Brillouin zone. When the interaction between particles is relatively large compared to the lattice height, the chemical potential and the compressibility show an excellent agreement with their corresponding Thomas-

Fermi approximation closed-form expressions.

Recently, there has been a notorious interest in the experimental realization of optical lattices with a subwavelength structure (SWOL) [36, 37, 113]. From the experimental side, SWOLs have potential applications in the study of p-wave superfluidity in fermionic gases [149, 150]. From the theoretical point of view, these lattices, which are composed of a succession of very narrow, high potential barriers, can be seen as experimental realizations of the 1D Dirac-comb potential. Precisely, the KP potential we use to model the multi-rod lattice becomes the Dirac-comb potential in the limit when the barriers become very high and very thin, but the area below them remains finite. Accordingly, we used our multi-rod lattice to predict the ground-state density and energy band spectrum of a BEC within a SWOL.

Beyond mean-field theory, we resorted to QMC methods to estimate the zero temperature, ground-state properties the 1D Bose gas with contact-like, repulsive interactions of arbitrary magnitude in the presence of a multi-rod lattice. First, we investigated the particular case where the lattice is absent since our system becomes the 1D Lieb-Liniger Bose gas [24]. In this case, we calculated both VMC and DMC ground-state energies for interactions ranging from the high density, weakly interacting regime where the GPE is applicable, up to the low density, strongly interacting TG regime of impenetrable bosons. Our numerical results are in complete agreement with the theoretical predictions of the LL for any value of the interaction.

When the Bose gas is subject to the multi-rod lattice, new types of phenomena may appear due to quantum effects, in particular, the superfluid–Mott insulator phase transition. To study this transition, we employ the Luttinger-liquid Theory [20, 82–84]. This theoretical formalism is a low-energy, effective-description for an extensive collection of 1D quantum many-body systems (Luttinger liquids) that share several common properties; among these systems is the LL Bose gas. Luttinger-liquid formalism predicts that in the presence of a periodic lattice, a Luttinger liquid, being initially a superfluid, can undergo a phase transition to a Mott-insulator state in two ways: by a Mott-U transition, or by a Mott-δ transition. In this thesis, we only investigate the Mott-U transition, which occurs when (for a given lattice height) the interactions between particles are sufficiently strong, and the average density of the gas is commensurate with the lattice periodicity [85]. We use the well-known Feynmann relation to determine whether the Bose gas is a superfluid or a Mott-insulator from the low-momenta behavior of the static structure factor. Next, for a square multi-rod lattice, we calculate the interaction strength and lattice height where the boundary between the superfluid and Mott-insulator phases lies. Finally, we establish the zero-temperature phase diagram of the 1D Bose gas in a multi-rod

lattice. The superfluid–Mott-insulator phase diagram shows that the effect on the Bose gas behavior of a square multi-rod lattice is very similar to the one of an optical lattice with the same periodicity and lattice height. The boundary between superfluid and Mott-insulator phases is indeed very close when comparing experimental and QMC data for optical lattices with DMC obtained for our multi-rod lattice.

Future Work

During the development of this thesis, some prospects of future work that could complement and extend the current results arose.

Elementary Excitations of the Weakly-Interacting Bose Gas

The mean-field theory formalism and the Gross-Pitaevskii equation assume that the vast majority of the particles in a Bose gas occupy the ground-state of the system. Then, the Bogoliubov prescription is enforced, and quantum fluctuations are discarded. Naturally, on real quantum systems, this assumption does not always hold. To investigate the effect of quantum fluctuations on a weakly-interacting condensate, we can resort to the Bogoliubov formalism. In 1D systems, this formalism can be applied within the *phase-density* representation of the quantum field operators [63, 68]. We can exploit the Bogoliubov formalism predictions to determine if, for a given interaction strength between particles, or certain external lattice features, a Bose gas is a true condensate and the GPE is still applicable. Moreover, if the commensurability condition for a Mott-U transition is fulfilled, the superfluid to Mott-insulator phase transition can be observed [64, 65].

Influence of Lattice Defects on the Mott Transition

Our preliminary results obtained by DMC calculations show that the Mott-U transition is strongly affected by the presence of a lattice defect, for instance, by removing a single rod from the simulation supercell. Compared to the perfect multi-rod lattice, the superfluid phase area increases, in detriment of the Mott insulator phase area. Hence, the presence of a defect promotes superfluidity. The influence of lattice imperfections in the quantum behavior of crystals at sufficiently low temperatures is a relevant research topic. Andreev and Lifshitz [151], and later Chester [152], conjectured the existence of a *supersolid* phase where defects like vacancies or interstitials in the lattice of a quantum

solid can move from site to site forming a superfluid. QMC methods provide a way to study this exotic state of matter; see Refs. [153] and [154].

A

Lieb-Liniger Bose Gas

A.1. Estimation of the Ground State Energy

In the Lieb-Liniger theory introduction in Section 2.8, we saw that the energy of the ground state Eq. (2.98) depends on Eq. (2.101) that fixes the density of pseudo-momenta, and on the normalization condition Eq. (2.102). Equation (2.101) is a particular case of a Fredholm Integral Equation of the second kind [155, 156],

$$g(x) = f(x) + \lambda \int_a^b K(x, x')g(x') \, dx', \tag{A.1}$$

where the function $g(x)$ is the unknown function we want to obtain. $K(x, x')$ is called *the kernel*, $f(x)$ is a known function, and λ is a regular value of the kernel. For Eq. (2.101), we have

$$g(x; \gamma) = \frac{1}{2\pi} + \lambda(\gamma) \int_{-1}^{+1} K(x, x'; \gamma)g(x'; \gamma) \, dx', \tag{A.2}$$

where $\gamma = 2/n_1 a_{1D}$, $f(x) = 1/2\pi$, $\lambda(\gamma)$ is the regular value, and

$$K(x, x'; \gamma) = \frac{1/\pi}{\lambda^2(\gamma) + (x - x')^2}, \tag{A.3}$$

is the kernel. Equation (A.2) can not be solved for all values of γ analytically. However, we can resort to numerical integration methods to obtain an approximation of $g(x; \gamma)$ and $\lambda(\gamma)$.

In general, numerical integration techniques approximate an integral as a weighted sum,

$$\int_a^b f(x) \, dx \approx \sum_{j=1}^M w_j f(x_j). \tag{A.4}$$

The weighted sum is done over a set of M abscissas x_i in the integrand domain and its corresponding w_i weights. The accuracy and error of the approximation will depend on the integration technique –quadrature rule– used and on how many abscissas and weights are used. A rule may include the integration limits in the weighed sum; in this case, it is called a *closed method*. If the rule only uses points in the open interval (a, b), it is called an *open formula*.

If we approximate the integrand in the r.h.s of Eq. (A.2) by a quadrature rule Eq. (A.4), then Eq. (A.2) is reduced to

$$g(x; \gamma) - \lambda(\gamma) \sum_{j=1}^{M} w_j K(x, x_j; \gamma) g(x_j; \gamma) = \frac{1}{2\pi}. \tag{A.5}$$

A solution $g(x; \gamma)$ must satisfy this equation for all $a \leq x \leq b$, in particular for the i-nth abscissa x_i. In this way, we arrive at the equality

$$g(x_i; \gamma) - \lambda(\gamma) \sum_{j=1}^{M} w_j K(x_i, x_j; \gamma) g(x_j; \gamma) = \frac{1}{2\pi}. \tag{A.6}$$

Considering the whole set of abscissas x_i, we have a system of M linear equations that we can write in matrix notation as

$$(\mathbf{I} - \lambda(\gamma) \mathbf{K} \mathbf{D_w}) \, \tilde{\mathbf{g}} = \frac{1}{2\pi} \mathbf{1}. \tag{A.7}$$

Here, $\tilde{\mathbf{g}}$ is the column vector with components $g(x_j; \gamma)$, $\mathbf{1}$ is the unit vector, $\mathbf{I}$ is the identity matrix, $\mathbf{K}$ is the matrix whose $(\mathbf{K})_{ij}$ element is $K(x_i, x_j; \gamma)$ and $\mathbf{D_w}$ is the diagonal matrix whose diagonal element $(\mathbf{D_w})_{ii}$ is the weight w_i.

To obtain an approximation for $g(x; \gamma)$, we have to set value for $\lambda(\gamma)$, where we assume that γ has an unknown value at this point, and then we can solve Eq. (A.7). The resulting set of values $\{g(x_i; \gamma) \mid i = 1, 2, \dots, M\}$, together with the quadrature abscissas x_i and weights w_i, are used to calculate the corresponding value of γ and $e(\gamma)$. To calculate γ, we approximate Eq. (2.102) by the quadrature

$$\gamma \approx \lambda(\gamma) \left(\sum_{j=1}^{M} w_j \, g(x_j; \gamma) \right)^{-1} \tag{A.8}$$

with the same abscissas and weights used to approximate Eq. (A.5). Finally, to obtain the ground state energy Eq. (2.98), we approximate Eq. (2.100) by the quadrature

$$e(\gamma) \approx \left(\frac{\gamma}{\lambda(\gamma)} \right)^3 \sum_{j=1}^{M} w_j \, g(x_j; \gamma) x_j^2, \tag{A.9}$$

where the quotient $\gamma/\lambda(\gamma)$ is obtained from Eq. (A.8). This way, we obtain the ground-state energy as a function of $\lambda(\gamma)$, and therefore, as a function of γ.

B

QMC Technical Aspects

In the following sections, we illustrate some important technical aspects on VMC and QMC calculations.

B.1. Variational Monte Carlo

In Fig. B.1, we show $e(\gamma)$ calculated using VMC for a LL Bose gas as a function of the variational parameter r_m for $n_1 a_{1D} = 1$, which is a relatively strongly-interacting system that lies in the intermediate regime shown in Fig. 5.2. The ground-state energy is proportional to $e(\gamma)$, according to Eq. (5.35). We highlight the following features:

- Finite-size effects can be observed by increasing the number of particles in the simulation: $N = 24$, 48, and 72 particles: there is a slight increase in the energy for larger N.

- The energy shows a minimum that moves towards smaller r_m/L values as the number of particles N increases. At the same time, the dependence of E/N for $r_m/L \to 0.5$ reduces.

Similar behavior can be observed for $n_1 a_{1D} = 0.01$ and 10 in Figs. B.2a, b, respectively. For the strongly-interacting gas with $n_1 a_{1D} = 0.01$, despite the statistical noise, the energy is practically independent of r_m, although it increases due to finite-size effects. On the other hand, for $n_1 a_{1D} = 10$, there is a clear dependence of the energy on r_m, and finite-size effects are more important as the significant increase in the energy from $N = 24$ to $N = 48$ shows.

Although VMC gives valuable information about the properties of the system, we used the DMC method to obtain the main results of this thesis. The

Figure B.1: Ground-state energy per boson (VMC) as a function of the variational parameter r_m, for $n_1a_{1D} = 1$ (intermediate regime of interactions). An energy rise from finite-size effects can be observed from three sets of energies for $N = 24$, 48, and 72 particles. The value of r_m where the energy reaches a minimum is observed.
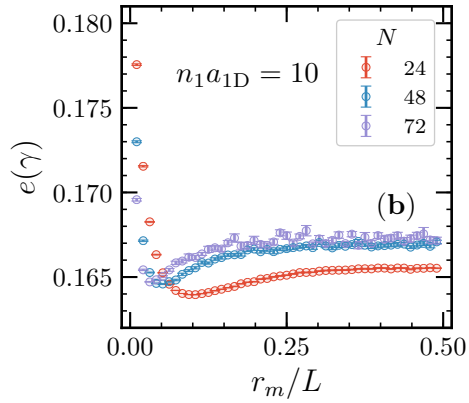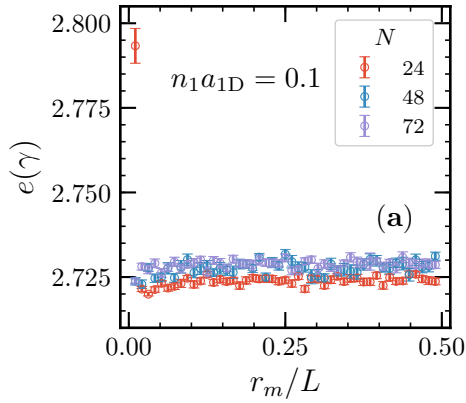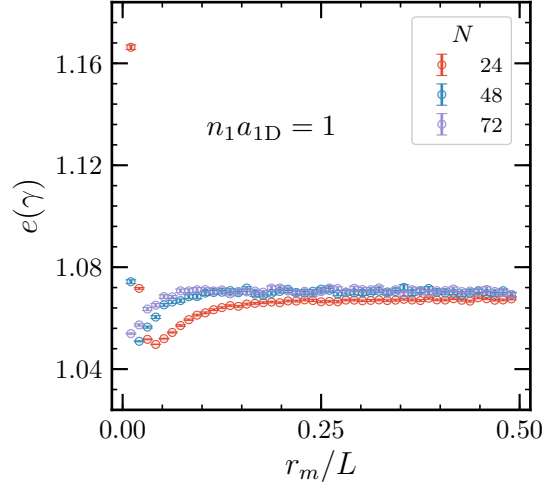

Figure B.2: Ground-state energy per boson (VMC) as a function of the variational parameter r_m. **(a)**: $n_1a_{1D} = 0.1$ represents a strongly interacting system, while **(b)**: $n_1a_{1D} = 10$ corresponds to a weakly-interacting gas. Three sets of energies for $N = 24$, 48, and 72 particles have been plotted.

variational approach is used mainly for the optimization of the trial-wave function used in DMC for importance sampling, in order to reduce the length of the calculations.

B.2. Diffusion Monte Carlo

DMC results have a *bias* that depends on the imaginary time step magnitude $\delta\tau$, as the method yields exact results only in the limit when $\delta\tau \to 0$. In princi-

ple, the magnitude of the time step should be small enough that the short-time approximation of the Green's function Eq. (4.54) is valid. However, if a very small $\delta\tau$ is used, more steps are required to reach convergence within a given statistical error. Also, we saw in Section 4.5.6 that for sufficiently small $\delta\tau$, DMC ground-state energy should scale linearly with $\delta\tau$,

$$E_0(\delta\tau) = E_0 + \kappa\delta\tau. \tag{B.1}$$

One should calculate E_0 for different time steps in the linear regime, and then extrapolate to zero $\delta\tau$ to find the best approximation to the exact ground-state energy.

Besides the time step dependence, DMC results depend on the system size. The supercell approximation Section 4.8 we use for studying extended systems reduces the analysis to a finite volume subject to periodic boundary conditions. This procedure introduces finite-size effects that we can account for by increasing the size L of the simulation cell progressively; then, we realize an extrapolation to $L \to \infty$. Let be the system density

$$n_1 \equiv \frac{N}{L}, \tag{B.2}$$

which we keep constant during a QMC simulation. Then, the size of the system increases by adding more particles to the simulation, since $L = n_1^{-1}N$.

In Fig. B.3, we show the behavior of the Lieb-Liniger Bose gas function $e(\gamma) = (\tilde{E}_0/N)/(n_1 a_{1D})^2$ calculated from DMC ground-state energy per particle, according to Eq. (5.35). We realized several DMC calculations of E_0/N for different $\delta\tau$ values, repeating these calculations in four systems with an increasing number of particles $N = 24, 48, 72$, and 96, whose results we show in Figs. B.3a, b, c, d, respectively. Results clearly show that the energy scales linearly with time step $\delta\tau$. We performed a linear fit on $e(\gamma)$ for all the analyzed systems, obtaining the best approximation at $\delta\tau = 0$, which we indicate by a red circle. We can see that $e(\gamma)$ increases with the number of particles; remarkably, differences appear at the third digit after the decimal point, a clear indicator of DMC degree of accuracy for calculating ground-state energies. As a reference, the exact energy obtained from the LL function Eq. (2.100) is ~ 0.63915.

In Figs. B.4a, b, we show the dependence of Lieb-Liniger $e(\gamma)$ as a function of the inverse of the number of particles N^{-1}, for $\gamma = 1$ ($n_1 a_{1D} = 2$) and $\gamma = 20$ ($n_1 a_{1D} = 0.1$), respectively. We can observe that $e(\gamma)$ increases as we add more particles, i.e., as we increase the system size, but eventually, it reaches a plateau. We calculate the value of the ground-state energy extrapolated for very large N according to the relation [135]

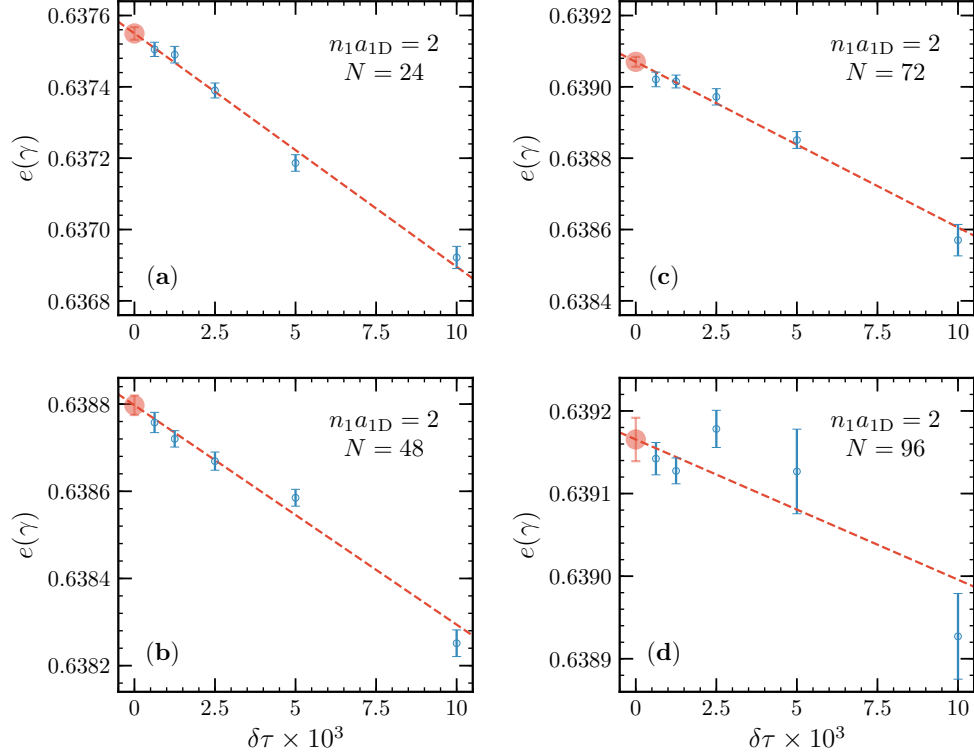$$\epsilon(N) = \epsilon(N \to \infty) + f(N), \tag{B.3}$$

Figure B.3: Dependence of DMC–calculated LL $e(\gamma)$ as a function of the time step $\delta\tau$. The ground-state energy was calculated for $\gamma = 1$ ($n_1 a_{1D} = 2$). Results obtained from DMC (blue circles) show a linear dependence for small time steps. The red circle indicates the value of $e(\gamma)$ extrapolated to $\delta\tau = 0$. We can observe how $e(\gamma)$ at zero $\delta\tau$ increases with the number of particles.

where $\epsilon(N) \equiv E_0(N)/N$, and $f(N)$ is a function that vanishes for $N \to \infty$. For sufficiently large N, $f(N)$ is dominated by a contribution proportional to $1/N$. Hence, at large enough N, we have

$$\epsilon(N) = \epsilon(N \to \infty) + \kappa' N^{-1}. \tag{B.4}$$

For the LL Bose gas with a fixed interaction strength $n_1 a_{1D}$, we obtain

$$e(\gamma)_N = e(\gamma)_{N\to\infty} + \kappa'' N^{-1}. \tag{B.5}$$

The black circles in Figs. B.4a, b show the extrapolated value $e(\gamma)_{N\to\infty}$ obtained from DMC data. These results are in excellent agreement with the value of $e(\gamma)$ calculated from the LL function Eq. (2.100). A red circle shows this last value.
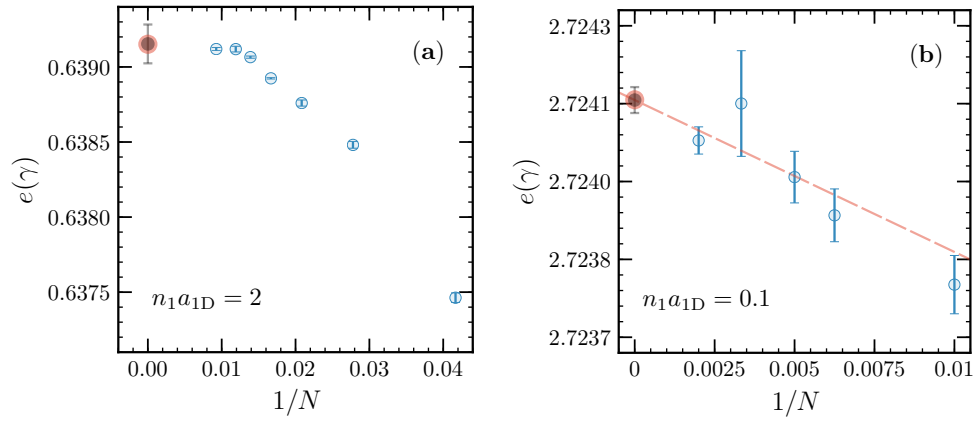
Figure B.4: Dependence of DMC–calculated LL $e(\gamma)$ as a function of N^{-1}. The ground-state energy was calculated for **(a)**: $\gamma = 1$ ($n_1 a_{1D} = 2$) and **(b)**: $\gamma = 20$ ($n_1 a_{1D} = 0.1$). Blue circles show results calculated through DMC. The red circle indicates the exact value of $e(\gamma)$ obtained from Eq. (2.100). The black circle is the extrapolation of $e(\gamma)$ for $N \to \infty$, according to Eq. (B.5).

Bibliography

[1]   M. H. Anderson, J. R. Ensher, M. R. Matthews, C. E. Wieman, and E. A. Cornell, "Observation of Bose-Einstein Condensation in a Dilute Atomic Vapor", Science **269**, 198 (1995).

[2]   K. B. Davis, M. O. Mewes, M. R. Andrews, N. J. Van Druten, D. S. Durfee, D. M. Kurn, and W. Ketterle, "Bose-Einstein condensation in a gas of sodium atoms", Phys. Rev. Lett. **75**, 3969 (1995).

[3]   A. Einstein, *Quantentheorie des einatomigen idealen Gases* (Preussische Akademie der Wissenschaften, 1924).

[4]   D. Jaksch, C. Bruder, J. I. Cirac, C. W. Gardiner, and P. Zoller, "Cold bosonic atoms in optical lattices", Phys. Rev. Lett. **81**, 3108 (1998).

[5]   J. Reichel, W. Hänsel, and T. W. Hänsch, "Atomic Micromanipulation with Magnetic Surface Traps", Phys. Rev. Lett. **83**, 3398 (1999).

[6]   N. H. Dekker, C. S. Lee, V. Lorent, J. H. Thywissen, S. P. Smith, M. Drndić, R. M. Westervelt, and M. Prentiss, "Guiding Neutral Atoms on a Chip", Phys. Rev. Lett. **84**, 1124 (2000).

[7]   Folman, Ron and Krüger, Peter and Cassettari, Donatella and Hessmo, Björn and Maier, Thomas and Schmiedmayer, Jörg, "Controlling Cold Atoms using Nanofabricated Surfaces: Atom Chips", Phys. Rev. Lett. **84**, 4749 (2000).

[8]   W. Hänsel, P. Hommelhoff, T. W. Hänsch, and J. Reichel, "Bose–Einstein condensation on a microelectronic chip", Nature **413**, 498 (2001).

[9]   I. Bloch, "Quantum gases in optical lattices", Phys. World **17**, 25 (2004).

[10] I. Bloch, "Ultracold quantum gases in optical lattices", Nat. Phys. **1**, 23 (2005).

[11] I. Bloch, J. Dalibard, and S. Nascimbène, "Quantum simulations with ultracold quantum gases", Nat. Phys. **8**, 267 (2012).

[12] C. Gross and I. Bloch, "Quantum simulations with ultracold atoms in optical lattices", Science **357**, 995 (2017).

[13] A. Görlitz, J. M. Vogels, A. E. Leanhardt, C. Raman, T. L. Gustavson, J. R. Abo-Shaeer, A. P. Chikkatur, S. Gupta, S. Inouye, T. Rosenband, et al., "Realization of Bose-Einstein Condensates in Lower Dimensions", Phys. Rev. Lett. **87**, 130402 (2001).

[14] J. Esteve, J.-B. Trebbia, T. Schumm, A. Aspect, C. I. Westbrook, and I. Bouchoule, "Observations of Density Fluctuations in an Elongated Bose Gas: Ideal Gas and Quasicondensate Regimes", Phys. Rev. Lett. **96**, 130403 (2006).

[15] T. Jacqmin, J. Armijo, T. Berrada, K. V. Kheruntsyan, and I. Bouchoule, "Sub-Poissonian Fluctuations in a 1D Bose Gas: From the Quantum Quasicondensate to the Strongly Interacting Regime", Phys. Rev. Lett. **106**, 230405 (2011).

[16] B. Yuen, I. J. M. Barr, J. P. Cotter, E. Butler, and E. A. Hinds, "Enhanced oscillation lifetime of a Bose–Einstein condensate in the 3D/1D crossover", New J. Phys. **17**, 093041 (2015).

[17] B. Rauer, P. Grišins, I. E. Mazets, T. Schweigler, W. Rohringer, R. Geiger, T. Langen, and J. Schmiedmayer, "Cooling of a One-Dimensional Bose Gas", Phys. Rev. Lett. **116**, 030402 (2016).

[18] S. Hofferberth, I. Lesanovsky, B. Fischer, T. Schumm, and J. Schmiedmayer, "Non-equilibrium coherence dynamics in one-dimensional Bose gases", Nature **449**, 324 (2007).

[19] L. Tonks, "The Complete Equation of State of One, Two and Three-Dimensional Gases of Hard Elastic Spheres", Phys. Rev. **50**, 955 (1936).

[20] J. M. Luttinger, "An exactly soluble model of a many-fermion system", J. Math. Phys. **4**, 1154 (1963).

[21] B. Paredes, A. Widera, V. Murg, O. Mandel, S. Folling, I. Cirac, G. V. Shlyapnikov, T. W. Hansch, and I. Bloch, "Tonks-Girardeau gas of ultra-cold atoms in an optical lattice", Nature **429**, 277 (2004).

[22] T. Kinoshita, "Observation of a One-Dimensional Tonks-Girardeau Gas", Science **305**, 1125 (2004).

[23] M. Girardeau, "Relationship between Systems of Impenetrable Bosons and Fermions in One Dimension", J. Math. Phys. **1**, 516 (1960).

[24] E. H. Lieb and W. Liniger, "Exact Analysis of an Interacting Bose Gas. I. The General Solution and the Ground State", Phys. Rev. **130**, 1605 (1963).

[25] F. Calogero, "Solution of a three-body problem in one dimension", J. Math. Phys. **10**, 2191 (1969).

[26] E. P. Gross, "Structure of a quantized vortex in boson systems", Nuovo Cim. **20**, 454 (1961).

[27] L. P. Pitaevskii, "Vortex Lines in an imperfect Bose gas", Sov. Phys. JETP **13**, 451 (1961).

[28] F. Dalfovo, S. Giorgini, L. P. Pitaevskii, and S. Stringari, "Theory of Bose-Einstein condensation in trapped gases", Rev. Mod. Phys. **71**, 463 (1999).

[29] L. M. Steele, C. J. Yeager, and D. Finotello, "Precision specific-heat studies of thin superfluid films", Phys. Rev. Lett. **71**, 3673 (1993).

[30] K. Shirahama, K. Yamamoto, and Y. Shibayama, "Localized Bose–Einstein Condensation of 4 He Confined in Nanoporous Media", J. Phys. Soc. Japan **77**, 111011 (2008).

[31] D. M. Ceperley, "An Overview of Quantum Monte Carlo Methods", Rev. Mineral. Geochemistry **71**, 129 (2010).

[32] J. Boronat and J. Casulleras, "Monte Carlo analysis of an interatomic potential for He", Phys. Rev. B **49**, 8920 (1994).

[33] J. Casulleras and J. Boronat, "Unbiased estimators in quantum Monte Carlo methods: Application to liquid ^{4}He", Phys. Rev. B **52**, 3654 (1995).

[34] G. E. Astrakharchik and S. Giorgini, "Correlation functions and momentum distribution of one-dimensional Bose systems", Phys. Rev. A **68**, 031602 (2003).

[35] G. E. Astrakharchik, J. Boronat, J. Casulleras, and S. Giorgini, "Beyond the Tonks-Girardeau Gas: Strongly Correlated Regime in Quasi-One-Dimensional Bose Gases", Phys. Rev. Lett. **95**, 190407 (2005).

[36] M. Łącki, M. A. Baranov, H. Pichler, and P. Zoller, "Nanoscale "Dark State" Optical Potentials for Cold Atoms", Phys. Rev. Lett. **117**, 233001 (2016).

[37] Y. Wang, S. Subhankar, P. Bienias, M. Łącki, T.-C. Tsui, M. A. Baranov, A. V. Gorshkov, P. Zoller, J. V. Porto, and S. L. Rolston, "Dark State Optical Lattice with a Subwavelength Spatial Structure", Phys. Rev. Lett. **120**, 083601 (2018).

[38] N. Metropolis, A. W. Rosenbluth, M. N. Rosenbluth, A. H. Teller, and E. Teller, "Equation of State Calculations by Fast Computing Machines", J. Chem. Phys. **21**, 1087 (1953).

[39] E. K. U. Gross, E. Runge, and O. Heinonen, *Many-Particle Theory* (Adam Hilger, Bristol, 1991).

[40] R. K. Pathria and P. D. Beale, *Statistical Mechanics* (Academic Press, Boston, MA, 2011), 3rd ed.

[41] C. N. Yang, "Concept of Off-Diagonal Long-Range Order and the Quantum Phases of Liquid He and of Superconductors", Rev. Mod. Phys. **34**, 694 (1962).

[42] O. Penrose and L. Onsager, "Bose-Einstein Condensation and Liquid Helium", Phys. Rev. **104**, 576 (1956).

[43] N. N. Bogolyubov, "On the theory of superfluidity", J. Phys.(USSR) **11**, 23 (1947).

[44] C. J. Pethick and H. Smith, *Bose-Einstein Condensation in Dilute Gases* (Cambridge University Press, New York, 2008), 2nd ed.

[45] L. Pitaevskii and S. Stringari, *Bose-Einstein Condensation and Superfluidity* (Oxford University Press, New York, 2016), 2nd ed.

[46] T. Tsuzuki, "Nonlinear waves in the Pitaevskii-Gross equation", J. Low Temp. Phys. **4**, 441 (1971).

[47] B. T. Seaman, L. D. Carr, and M. J. Holland, "Effect of a potential step or impurity on the Bose-Einstein condensate mean field", Phys. Rev. A **71**, 033609 (2005).

[48] W.-T. WANG, Y.-Y. LI, and S.-J. YANG, "EXACT SOLUTIONS TO THE THREE-DIMENSIONAL GROSS–PITAEVSKII EQUATION WITH MODULATED RADIAL NONLINEARITY", Mod. Phys. Lett. B **27**, 1350105 (2013).

[49] K. Berg-Sørensen and K. Mølmer, "Bose-Einstein condensates in spatially periodic potentials", Phys. Rev. A **58**, 1480 (1998).

[50] M. Krämer, C. Menotti, L. Pitaevskii, and S. Stringari, "Bose-Einstein condensates in 1D optical lattices: Compressibility, Bloch bands and elementary excitations", Eur. Phys. J. D pp. 247–261 (2003).

[51] W. Li and A. Smerzi, "Nonlinear Kronig-Penney model", Phys. Rev. E **70**, 016605 (2004).

[52] P. Muruganandam and S. K. Adhikari, "Bose–Einstein condensation dynamics in three dimensions by the pseudospectral and finite-difference methods", J. Phys. B At. Mol. Opt. Phys. **36**, 2501 (2003).

[53] W. Bao and J. Shen, "A Fourth-Order Time-Splitting Laguerre–Hermite Pseudospectral Method for Bose–Einstein Condensates", SIAM J. Sci. Comput. **26**, 2010 (2005).

[54] X. Antoine, W. Bao, and C. Besse, "Computational methods for the dynamics of the nonlinear Schrödinger/Gross–Pitaevskii equations", Comput. Phys. Commun. **184**, 2621 (2013).

[55] X. Antoine and R. Duboscq, "GPELab, a Matlab toolbox to solve Gross–Pitaevskii equations II: Dynamics and stochastic simulations", Comput. Phys. Commun. **193**, 95 (2015).

[56] H. Wang, X. Ma, J. Lu, and W. Gao, "An efficient time-splitting compact finite difference method for Gross–Pitaevskii equation", Appl. Math. Comput. **297**, 131 (2017).

[57] M. O. Mewes, M. R. Andrews, N. J. Van Druten, D. M. Kurn, D. S. Durfee, and W. Ketterle, "Bose-einstein condensation in a tightly confining dc magnetic trap", Phys. Rev. Lett. **77**, 416 (1996).

[58] E. H. Lieb, R. Seiringer, and J. Yngvason, "A Rigorous Derivation of the Gross-Pitaevskii Energy Functional for a Two-Dimensional Bose Gas", Commun. Math. Phys. **224**, 17 (2001).

[59] Y. Cai, M. Rosenkranz, Z. Lei, and W. Bao, "Mean-field regime of trapped dipolar Bose-Einstein condensates in one and two dimensions", Phys. Rev. A **82**, 043623 (2010).

[60] N. D. Mermin and H. Wagner, "Absence of Ferromagnetism or Antiferromagnetism in One- or Two-Dimensional Isotropic Heisenberg Models", Phys. Rev. Lett. **17**, 1133 (1966).

[61] P. C. Hohenberg, "Existence of Long-Range Order in One and Two Dimensions", Phys. Rev. **158**, 383 (1967).

[62] D. S. Petrov, D. M. Gangardt, and G. V. Shlyapnikov, "Low-dimensional trapped gases", J. Phys. IV **116**, 5 (2004).

[63] C. Mora and Y. Castin, "Extension of Bogoliubov theory to quasicondensates", Phys. Rev. A **67**, 053615 (2003).

[64] L. Fontanesi, *Quantum Phase Transition in a Low-Dimensional Weakly Interacting Bose Gas* (EPFL, Lausanne, 2011).

[65] J. Saliba, P. Lugan, and V. Savona, "Superfluid-insulator transition in weakly interacting disordered Bose gases: A kernel polynomial approach", New J. Phys. **15**, 045006 (2013).

[66] Y. Kagan, B. Svistunov, and G. V. Shlyapnikov, "Influence on dimensional inelastic processes of the phase transition in a weakly collisional two-Bose gas", Sov. Phys. JETP **66**, 314 (1987).

[67] S. Dettmer, D. Hellweg, P. Ryytty, J. J. Arlt, W. Ertmer, K. Sengstock, D. S. Petrov, G. V. Shlyapnikov, H. Kreutzmann, L. Santos, et al., "Observation of Phase Fluctuations in Elongated Bose-Einstein Condensates", Phys. Rev. Lett. **87**, 160406 (2001).

[68] Y. Castin, "Simple theoretical tools for low dimension Bose gases", J. Phys. IV **116**, 89 (2004).

136

[69] W. Ketterle and N. J. van Druten, "Bose-Einstein condensation of a finite number of particles trapped in one or three dimensions", Phys. Rev. A **54**, 656 (1996).

[70] T. L. Ho and M. Ma, "Quasi 1 and 2d Dilute Bose Gas in Magnetic Traps: Existence of Off-Diagonal Order and Anomalous Quantum Fluctuations", J. Low Temp. Phys. **115**, 61 (1999).

[71] C. Gils, L. Pollet, A. Vernier, F. Hebert, G. G. Batrouni, and M. Troyer, "Quantum Monte Carlo study of a one-dimensional phase-fluctuating condensate in a harmonic trap", Phys. Rev. A **75**, 063631 (2007).

[72] D. S. Petrov, G. V. Shlyapnikov, and J. T. M. Walraven, "Regimes of Quantum Degeneracy in Trapped 1D Gases", Phys. Rev. Lett. **85**, 3745 (2000).

[73] M. Olshanii, "Atomic Scattering in the Presence of an External Confinement and a Gas of Impenetrable Bosons", Phys. Rev. Lett. **81**, 938 (1998).

[74] T. Bergeman, M. G. Moore, and M. Olshanii, "Atom-atom scattering under cylindrical harmonic confinement: Numerical and analytic studies of the confinement induced resonance", Phys. Rev. Lett. **91**, 1 (2003).

[75] V. Dunjko, V. Lorent, and M. Olshanii, "Bosons in Cigar-Shaped Traps: Thomas-Fermi Regime, Tonks-Girardeau Regime, and In Between", Phys. Rev. Lett. **86**, 5413 (2001).

[76] E. Haller, M. Gustavsson, M. J. Mark, J. G. Danzl, R. Hart, G. Pupillo, and H. C. Nägerl, "Realization of an excited, strongly correlated quantum gas Phase", Science **325**, 1224 (2009).

[77] H. Bethe, "Zur Theorie der Metalle", Zeitschrift für Physik **71**, 205 (1931).

[78] M. A. Cazalilla, R. Citro, T. Giamarchi, E. Orignac, and M. Rigol, "One dimensional bosons: From condensed matter systems to ultracold gases", Rev. Mod. Phys. **83**, 1405 (2011).

[79] L. D. Landau, "The Theory of a Fermi Liquid", Soviet Physics JETP **3**, 920 (1957).

[80] P. Nozières and J. M. Luttinger, "Derivation of the Landau Theory of Fermi Liquids. I. Formal Preliminaries", Phys. Rev. **127**, 1423 (1962).

[81] J. M. Luttinger and P. Nozières, "Derivation of the Landau Theory of Fermi Liquids. II. Equilibrium Properties and Transport Equation", Phys. Rev. **127**, 1431 (1962).

[82] F. D. M. Haldane, "General Relation of Correlation Exponents and Spectral Properties of One-Dimensional Fermi Systems: Application to the Anisotropic $S = \frac{1}{2}$ Heisenberg Chain", Phys. Rev. Lett. **45**, 1358 (1980).

[83] F. D. Haldane, "'Luttinger liquid theory' of one-dimensional quantum fluids. I. Properties of the Luttinger model and their extension to the general 1D interacting spinless fermi gas", J. Phys. C Solid State Phys. **14**, 2585 (1981).

[84] F. D. M. Haldane, "Effective Harmonic-Fluid Approach to Low-Energy Properties of One-Dimensional Quantum Fluids", Phys. Rev. Lett. **47**, 1840 (1981).

[85] T. Giamarchi, *Quantum Physics in One Dimension*, The International Series of Monographs on Physics (Oxford Clarendon Press, 2003), 1st ed.

[86] M. A. Cazalilla, "Bosonizing one-dimensional cold atomic gases", J. Phys. B At. Mol. Opt. Phys. **37** (2004).

[87] T. Giamarchi and B. S. Shastry, "Persistent currents in a one-dimensional ring for a disordered Hubbard model", Phys. Rev. B **51**, 10915 (1995).

[88] C. Chin, R. Grimm, P. Julienne, and E. Tiesinga, "Feshbach resonances in ultracold gases", Rev. Mod. Phys. **82**, 1225 (2010).

[89] L. Santos, M. A. Baranov, J. I. Cirac, H.-U. Everts, H. Fehrmann, and M. Lewenstein, "Atomic Quantum Gases in Kagomé Lattices", Phys. Rev. Lett. **93**, 030601 (2004).

[90] G.-B. Jo, J. Guzman, C. K. Thomas, P. Hosur, A. Vishwanath, and D. M. Stamper-Kurn, "Ultracold Atoms in a Tunable Optical Kagome Lattice", Phys. Rev. Lett. **108**, 045305 (2012).

[91] M. Greiner, O. Mandel, T. Esslinger, T. W. Hänsch, and I. Bloch, "Quantum phase transition from a superfluid to a Mott insulator in a gas of ultracold atoms", Nature **415**, 39 (2002).

[92]   Haller, Elmar and Hart, Russell and Mark, Manfred J and Danzl, Johann G and Reichsöllner, Lukas and Gustavsson, Mattias and Dalmonte, Marcello and Pupillo, Guido and Nägerl, Hanns-Christoph, "Pinning quantum phase transition for a Luttinger liquid of strongly interacting bosons", Nature **466**, 597 (2010).

[93]   J. G. Bednorz and K. A. Müller, "Possible high-Tc superconductivity in the $Ba-La-Cu-O$ system", Zeitschrift für Phys. B Condens. Matter **64**, 189 (1986).

[94]   L. Gao, Y. Y. Xue, F. Chen, Q. Xiong, R. L. Meng, D. Ramirez, C. W. Chu, J. H. Eggert, and H. K. Mao, "Superconductivity up to 164 K in $HgBa_2Ca_{m-1}Cu_mO_{2m+2+\delta}$ ($m =$1, 2, and 3) under quasihydrostatic pressures", Phys. Rev. B **50**, 4260 (1994).

[95]   M. R. Norman and C. Pépin, "The electronic nature of high temperature cuprate superconductors", Reports Prog. Phys. **66**, 1547 (2003).

[96]   H. Ott, J. Fortagh, G. Schlotterbeck, A. Grossmann, and C. Zimmermann, "Bose-Einstein Condensation in a Surface Microtrap", Phys. Rev. Lett. **87**, 230401 (2001).

[97]   J. Fortágh and C. Zimmermann, "Magnetic microtraps for ultracold atoms", Rev. Mod. Phys. **79**, 235 (2007).

[98]   M. Keil, O. Amit, S. Zhou, D. Groswasser, Y. Japha, and R. Folman, "Fifteen years of cold matter on the atom chip: promise, realizations, and prospects", J. Mod. Opt. **63**, 1840 (2016).

[99]   R. de L. Kronig and W. G. Penney, "Quantum Mechanics of Electrons in Crystal Lattices", Proc. R. Soc. A Math. Phys. Eng. Sci. **130**, 499 (1931).

[100] V. E. Zakharov and A. B. Shabat, "Exact theory of two-dimensional self-focussing and one-dimensional self-modulating waves in nonlinear media", Sov. Phys. JETP **34**, 62 (1972).

[101] M. Abramowitz, I. A. Stegun, and D. Miller, *Handbook of Mathematical Functions With Formulas, Graphs and Mathematical Tables (National Bureau of Standards Applied Mathematics Series No. 55)*, vol. 32 (ASME, 1965).

[102] R. L. Burden and J. D. Faires, in *Numerical Analysis* (Cengage Learning, Boston, 2010), pp. 671–712, 9th ed.

[103] M. Machholm, C. J. Pethick, and H. Smith, "Band structure, elementary excitations, and stability of a Bose-Einstein condensate in a periodic potential", Phys. Rev. A **67**, 15 (2003).

[104] B. T. Seaman, L. D. Carr, and M. J. Holland, "Nonlinear band structure in Bose-Einstein condensates: Nonlinear Schrödinger equation with a Kronig-Penney potential", Phys. Rev. A **71**, 033622 (2005).

[105] X. Dong and B. Wu, "Instabilities and sound speed of a Bose-Einstein condensate in the Kronig-Penney potential", Laser Phys. **17**, 190 (2007).

[106] E. J. Mueller, "Superfluidity and mean-field energy loops: Hysteretic behavior in Bose-Einstein condensates", Phys. Rev. A **66**, 063603 (2002).

[107] D.-I. Choi and Q. Niu, "Bose-Einstein Condensates in an Optical Lattice", Phys. Rev. Lett. **82**, 2022 (1999).

[108] O. Morsch, J. H. Müller, M. Cristiani, D. Ciampini, and E. Arimondo, "Bloch Oscillations and Mean-Field Effects of Bose-Einstein Condensates in 1D Optical Lattices", Phys. Rev. Lett. **87**, 140402 (2001).

[109] L. Chen, Z. Chen, W. Li, Z. Zhang, and Z. Liang, "Unusual behavior of sound velocity of a Bose gas in an optical superlattice at quasi-one-dimension", Eur. Phys. J. D **68**, 375 (2014).

[110] P. Salas, F. J. Sevilla, M. Fortes, M. de Llano, A. Camacho, and M. A. Solís, "Dimensional crossover of a boson gas in multilayers", Phys. Rev. A **82**, 033632 (2010).

[111] P. Salas, M. Fortes, M. de Llano, F. J. Sevilla, and M. A. Solís, "Bose-Einstein Condensation in Multilayers", J. Low Temp. Phys. **159**, 540 (2010).

[112] S. Theodorakis and E. Leontidis, "Bound states in a nonlinear Kronig - Penney model", J. Phys. A. Math. Gen. **30**, 4835 (1997).

[113] S. Subhankar, P. Bienias, P. Titum, T.-C. Tsui, Y. Wang, A. V. Gorshkov, S. L. Rolston, and J. V. Porto, "Floquet engineering of optical lattices with spatial features and periodicity below the diffraction limit", arXiv **1906.07646** (2019).

[114] P. Krüger, S. Hofferberth, I. E. Mazets, I. Lesanovsky, and J. Schmiedmayer, "Weakly Interacting Bose Gas in the One-Dimensional Limit", Phys. Rev. Lett. **105**, 265302 (2010).

[115] R. O. Jones, "Density functional theory: Its origins, rise to prominence, and future", Rev. Mod. Phys. **87**, 897 (2015).

[116] H. Wang and Y. Zhang, "Density-functional theory for the spin-1 bosons in a one-dimensional harmonic trap", Phys. Rev. A **88**, 023626 (2013).

[117] F. Malet, A. Mirtschink, C. B. Mendl, J. Bjerlin, E. O. Karabulut, S. M. Reimann, and P. Gori-Giorgi, "Density-Functional Theory for Strongly Correlated Bosonic and Fermionic Ultracold Dipolar and Ionic Gases", Phys. Rev. Lett. **115**, 033006 (2015).

[118] M. Kalos and P. Whitlock, *Monte Carlo Methods* (Wiley-VCH, 2008), 2nd ed.

[119] W. Janke, in *Quantum Simulations of Complex Many-Body Systems: From Theory to Algorithms*, edited by J. Grotendorst, D. Marx, and A. Muramatsu (2002), vol. 10 of *NIC Series*, pp. 423–445.

[120] J. Toulouse, R. Assaraf, and C. J. Umrigar, in *Electron Correlation in Molecules – ab initio Beyond Gaussian Quantum Chemistry*, edited by P. E. Hoggan and T. Ozdogan (Academic Press, 2016), vol. 73 of *Advances in Quantum Chemistry*, pp. 285 – 314.

[121] R. Guardiola, *Monte Carlo methods in quantum many-body theories* (Springer Berlin Heidelberg, Berlin, Heidelberg, 1998), pp. 269–336.

[122] W. K. HASTINGS, "Monte Carlo sampling methods using Markov chains and their applications", Biometrika **57**, 97 (1970).

[123] C. J. Umrigar, "Observations on variational and projector Monte Carlo methods", J. Chem. Phys. **143**, 164105 (2015).

[124] H. F. Trotter, "On the product of semi-groups of operators", Proc. Am. Math. Soc. **10**, 545 (1959).

[125] C. Lin, F. H. Zong, and D. M. Ceperley, "Twist-averaged boundary conditions in continuum quantum Monte Carlo algorithms", Phys. Rev. E **64**, 12 (2001).

[126] P. J. Reynolds, D. M. Ceperley, B. J. Alder, and W. A. J. Lester, "Fixed-node quantum Monte Carlo for molecules", J. Chem. Phys. **77**, 5593 (1982).

[127] C. J. C. Umrigar, M. P. Nightingale, and K. J. Runge, "A diffusion Monte Carlo algorithm with very small time-step errors", J. Chem. Phys. **99**, 2865 (1993).

[128] K. S. Liu, M. H. Kalos, and G. V. Chester, "Quantum hard spheres in a channel", Phys. Rev. A **10**, 303 (1974).

[129] R. N. Barnett, P. J. Reynolds, and W. A. Lester, "Monte Carlo algorithms for expectation values of coordinate operators", J. Comput. Phys. **96**, 258 (1991).

[130] A. Bijl, "The lowest wave function of the symmetrical many particles system", Physica **7**, 869 (1940).

[131] R. Jastrow, "Many-Body Problem with Strong Forces", Phys. Rev. **98**, 1479 (1955).

[132] C. J. Umrigar, K. G. Wilson, and J. W. Wilkins, "Optimized trial wave functions for quantum Monte Carlo calculations", Phys. Rev. Lett. **60**, 1719 (1988).

[133] J. Toulouse and C. J. Umrigar, "Optimization of quantum Monte Carlo wave functions by energy minimization", J. Chem. Phys. **126**, 084102 (2007).

[134] G. Rajagopal, R. J. Needs, S. Kenny, W. M. C. Foulkes, and A. James, "Quantum Monte Carlo Calculations for Solids Using Special k Points Methods", Phys. Rev. Lett. **73**, 1959 (1994).

[135] J. Kolorenč and L. Mitas, "Applications of quantum Monte Carlo methods in condensed systems", Reports Prog. Phys. **74** (2011).

[136] G. Ortiz, D. M. Ceperley, and R. M. Martin, "New stochastic method for systems with broken time-reversal symmetry: 2D fermions in a magnetic field", Phys. Rev. Lett. **71**, 2777 (1993).

[137] L. Reatto and G. V. Chester, "Phonons and the Properties of a Bose System", Phys. Rev. **155**, 88 (1967).

[138] V. I. Yukalov, "Structure factor of bose-condensed systems", J. Phys. Stud. **11**, 55 (2007).

[139] J. Stenger, S. Inouye, A. P. Chikkatur, D. M. Stamper-Kurn, D. E. Pritchard, and W. Ketterle, "Bragg Spectroscopy of a Bose-Einstein Condensate", Phys. Rev. Lett. **82**, 4569 (1999).

[140] V. N. Popov, *Functional Integrals in Quantum Field Theory and Statistical Physics*, vol. 8 of *Mathematical Physics and Applied Mathematics* (Springer Netherlands, 1983), 1st ed.

[141] M. P. A. Fisher, P. B. Weichman, G. Grinstein, and D. S. Fisher, "Boson localization and the superfluid-insulator transition", Phys. Rev. B **40**, 546 (1989).

[142] T. D. Kühner and H. Monien, "Phases of the one-dimensional Bose-Hubbard model", Phys. Rev. B **58**, R14741 (1998).

[143] H. P. Büchler, G. Blatter, and W. Zwerger, "Commensurate-Incommensurate Transition of Cold Atoms in an Optical Lattice", Phys. Rev. Lett. **90**, 130401 (2003).

[144] R. P. Feynman, "Atomic theory of the two-fluid model of liquid helium", Phys. Rev. **94**, 262 (1954).

[145] J. Steinhauer, R. Ozeri, N. Katz, and N. Davidson, "Excitation Spectrum of a Bose-Einstein Condensate", Phys. Rev. Lett. **88**, 120407 (2002).

[146] G. Boéris, L. Gori, M. D. Hoogerland, A. Kumar, E. Lucioni, L. Tanzi, M. Inguscio, T. Giamarchi, C. D'Errico, G. Carleo, et al., "Mott transition for strongly interacting one-dimensional bosons in a shallow periodic potential", Phys. Rev. A **93**, 011601 (2016).

[147] G. E. Astrakharchik, K. V. Krutitsky, M. Lewenstein, and F. Mazzanti, "One-dimensional Bose gas in optical lattices of arbitrary strength", Phys. Rev. A **93**, 021605 (2016).

[148] S. Rapsch, U. Schollwöck, and W. Zwerger, "Density matrix renormalization group for disordered bosons in one dimension", Europhys. Lett. **46**, 559 (1999).

[149] A. K. Fedorov, V. I. Yudson, and G. V. Shlyapnikov, "P-wave superfluidity of atomic lattice fermions", Phys. Rev. A **95**, 043615 (2017).

[150] A. Negretti, R. Gerritsma, Z. Idziaszek, F. Schmidt-Kaler, and T. Calarco, "Generalized Kronig-Penney model for ultracold atomic quantum systems", Phys. Rev. B **90**, 155426 (2014).

[151] A. F. Andreev and I. M. Lifshitz, "Quantum Theory of Defects in Crystals", Sov. Phys. JETP **29**, 1107 (1969).

[152] G. V. Chester, "Speculations on Bose-Einstein Condensation and Quantum Crystals", Phys. Rev. A **2**, 256 (1970).

[153] F. Cinti, T. Macrì, W. Lechner, G. Pupillo, and T. Pohl, "Defect-induced supersolidity with soft-core bosons", Nat. Commun. **5**, 3235 (2014).

[154] G. E. Astrakharchik, K. V. Krutitsky, M. Lewenstein, F. Mazzanti, and J. Boronat, "Optical lattices as a tool to study defect-induced superfluidity", Phys. Rev. A **96**, 033606 (2017).

[155] S. M. Zemyan, in *The Classical Theory of Integral Equations: A Concise Treatment* (Birkhäuser Boston, Boston, MA, 2012), pp. 31–84.

[156] G. B. Arfken, H. J. Weber, and F. E. Harris, in *Mathematical Methods for Physicists: A Comprehensive Guide* (Academic Press, Boston, 2013), pp. 1047–1079, 7th ed.

Agradecimientos

No podría concluir esta tesis sin agradecer a todos aquellos que de alguna manera me han apoyado durante mi doctorado.

Quiero agradecer a mi tutor, el Dr. Miguel Ángel Solís Atala, por ofrecerme la oportunidad de trabajar con él, y por el continuo apoyo que me otorgó, especialmente en momentos difíciles, para superarme académicamente y conocer un poco más el inmenso mundo de la investigación científica. También quiero agradecer al Dr. Mauricio Fortes, al Dr. Francisco Javier Sevilla, y al Dr. Manuel de Llano, por haber formado parte de mi comité tutor y por el respaldo que me otorgaron para continuar con mi preparación académica.

Agradezco a mis sinodales: Dr. Jordi Boronat, Dr. Ricardo Méndez, Dr. Miztli Yépez, y Dr. Elías Castellanos, por ayudarme a mejorar este trabajo con sus comentarios, correcciones, y preguntas.

Quiero dar gracias al Dr. Jordi Boronat por invitarme a la Universitat Politècnica de Catalunya para realizar un par de estancias de investigación, y por su invaluable apoyo durante el tiempo que estuve en Barcelona. Ha sido una grata y placentera experiencia de la cual aprendí muchísimo, y que amplió mi visión a nuevos y fascinantes campos de investigación.

Al Instituto de Física de la UNAM y al Posgrado en Ciencias Físicas, agradezco por todo el conocimiento que me han otorgado, y por apoyarme en un sinfín de formas para desempeñar mi labor de investigación. Agradezco al CONACyT y al pueblo de México por haberme apoyado con una beca de doctorado, así como a los proyectos PAPIIT-DGAPA-UNAM IN-107616, IN-110319 y CONACyT-221030, por los múltiples apoyos que me otorgaron para participar en congresos. A la UNAM, mi *alma mater*, agradezco por el privilegio de haber aprendido en sus aulas, de la mano de grandes profesores e investigadores. A pesar de las dificultades, el proceso que hoy culmina ha sido maravilloso.

Sin el continuo apoyo y amor de mi madre y de mi padre no estaría donde me encuentro ahora. Les debo todo. Mi mayor agradecimiento es a ellos. Igualmente doy gracias a mis hermanos por estar cerca de mi por tantos años.

Y también quiero agradecer a esas personas tan especiales que han estado conmigo a lo largo de estos años en el posgrado. Agradezco a mis compañeros del Grupo de Física de Muchos Cuerpos: Patricia Salas, Guillermo Martínez, y Juan García Nila, por esas reuniones de trabajo donde siempre aprendía algo nuevo y había deliciosos bocadillos. Agradezco a mis amigos Erick, Pedro,